Generation of Particle Spectra and Azimuthal Anisotropy in Relativistic Heavy Ion Collisions at LHC

Bengt Henrik Brusheim Johansson

2015

Abstract

The observed particle distribution in Pb+Pb collisions at LHC are hypothesized to be calculable. Monte Carlo simulations provide insights in hadron genesis and *in materia* scattering, observing the azimuthal anisotropy and transverse momentum spectra.

The simulations are done using a model with parametrized soft processes and generation of hard physics. The analysis work done in this paper provides the means of investigating the modes of hadronization. The coalescence model is used in the investigation of hadronization along with higher order compound flow and analogies to multi particle correlators are made. The correlators are directly related to factorization of higher order flow. Factorization is then dependent on the level of coherence of the observed particle distribution. The modes of hadronization are then investigated under this hypothesis.

The elliptic and triangular flow are simulated with a high degree of precision for ($p_T < 3.5$) GeV and centralities $0-50\%$, along with the associated transverse momentum spectra, which displays an equally high degree of precision. This precision manifests in the integrated flow, which also displays a very high level of precision. The identified elliptic flow displays a dependence on decays for the coalescence regime. This phenomena is most visible for mesons, thus providing the conditions for constituent quark number scaling. Higher order flow is examined in the model and factorization, i.e. level of coherence, is in particular investigated, where the simulations display a p_T dependence. Coalescence and associated decays seem to provide the coherence levels needed for factorization. In present model, the fragmentation regime ($p_T < 3.5$ GeV), is producing non-factorizable flow, which posess different coherence levels.

Establishing the theorethical elliptic and triangular flow provides a solid base for further investigation of hadron genesis. The ability to simulate elliptic flow for identified particles provides us with the means of investigating coherence levels, and suggesting possible observables of hadronization. This investigation points out some possibilities of investigating the various modes of hadronization through multiparticle correlators. This reasoning can be elaborated upon, thus investigating multiparticle and multiplane (non linear) correlators in experimental data.

Acknowledgement

This thesis has been made during the last two years on part time basis, where the work has been done on my spare time and on leave from work. Besides a student conference held in Bergen, where some of the findings made by the research group were presented, the work has been done in Oslo at the Department of Physics at Oslo University. Here, the daily work has been done on the thesis and on the published and to be published papers. This is also where my thesis advisors reside, which I owe great gratitude to: Prof. Larissa V. Bravina and also Dr. Evgeny E. Zabrodin, which provided invaluable support and showed great patience having me as a student.

I would also like to thank the members of the associated research group: Gyulnara Eyyubova, Vladimir L. Korotkikh, Igor P. Lokhtin, Ludmila V. Malinina, Sergei V. Petrushanko and Alexander M. Snigirev for allowing me to learn from their work and vast amount of experience. I am equally thankful to I. Arsene, K. Tywoniuk, R. Lednicky, T. A. Pocheptsov, Iu. Karpenko, Yu. M. Sinyukov and A. Kaidalov for sharing their knowledge and work, and for giving me the opportunity to learn and derive from their and their predecessors work.

It has been a pleasure working on the available and nicely performing Oslo cluster and I would like to thank the staff at the formerly known as Titan and now referred to as the Abel cluster, which provides the infrastructure for computational work on an international level. I also would like to thank the IT-support at the Department of Physics at the University of Oslo for providing local support.

Furthermore, I would like to thank my colleagues at the Departement of Computer Science at HiOA for their support and also Thea Dæhli at "Folkeuniversitetet". I would also like to thank my colleagues and fellow students at the Faculty of Educational Sciences for having me and providing the sanctuary needed for my work. Also, I would like to thank the Department of Physics at the University of Bergen for the hospitality during my brief stay.

Finally, I would like to thank my parents Bengt and Elisabeth for their patience and support.

Contents

List of Figures

List of Tables

Chapter 1

Introduction

Abyssus abyssum invocat
The Holy Bible, *Versio Vulgata, 42:8*

In the early evolutionary stages of the universe, the primordial matter went under a series of phase transitions. In the Planck era, i.e. the first 10^{-43} s, the physics was of indeterminable origin [1, 2]. Cooling of the matter led to a phase transition, were gravitation freezes out and matter transits into the grand unified (GUT) epoch. In this stage strong and electroweak forces are unified and the temperature is of the order $\sim 10^{27}K$ when matter transforms into the quark regime.

For the evolutionary time $\tau = 10^{-11}$ s and a temperature of $T \sim 100$ GeV, electroweak phase transitions took place thus giving the elementary particles their mass. This regime is now accessible through observations at the Large Hadron Collider at CERN [3]. At $\tau \sim 10^{-5}$ s $T \sim 200$ MeV, strong phase transitions took place thus confining the quarks and gluons into hadrons and chiral symmetry was spontaneously broken. This regime is examined at all the modern colliders, including the Relativistic Heavy Ion Collider at Brookhaven National Laboratory [4, 5, 6] and also at SPS and CERN [7, 8, 9]. Later on, the Lepton epoch sets in at $\sim 10^{-4}$s. In this epoch, only lighter particles are in equilibrium and the neutrinos decouple at $\sim 10^{-3}$ s.

Deuterium and Helium starts to form at ~ 100 s when photon ionization is no longer possible which means the end of the radiation era. This nuclear regime is referred to as the nuclear epoch. The evolution goes on through further macroscopic stages; The Atomic, Galactic and Stellar stages of evolution, thus arriving at the "present day" conditions of $t = 10$ MY.

In order to study the processes involved during the early stages of the universe, the mentioned conditions during the cosmological evolution has to be recreated or simulated in the laboratory. Some of these conditions can be and are reproduced in the modern day particle colliders. In the colliders, hot

and dense conditions, which are necessary in order to observe an evolution of mass, can be achieved through smashing particles head on after accelerating them to speeds approaching the speed of light.

In particular, colliding two heavier particles will produce a brief and extremely small volume ~ 10 fm of "primordial" matter, which then can be studied through the observed particle distributions. This matter will also show a characteristic evolution, which will involve several phase transitions in metamorphing from the primordial state of matter into the observed hadron state in the detector $\sim 10^{15}$ times the interaction distance away.

The spatial and energy scale of the laboratory system, (~ 10) fm and $\sqrt{s} = 2.76$ TeV, i.e. the produced matter in the ion-ion collision, calls for a microscopic modern description due to the high yield multiplicity of the produced distribution, where e.g. ~ 20000 pions are produced in a central Pb+Pb collision. This makes the heavy ion collisions a particle laboratory, where interacting matter evolves and is detected as e.g. hadrons. These investigations of hadronization coupled to the macro scale genesis might be carried out in high energy colliders such as the Relativistic Heavy Ion Collider (RHIC) and the Large Hadron Collider (LHC).

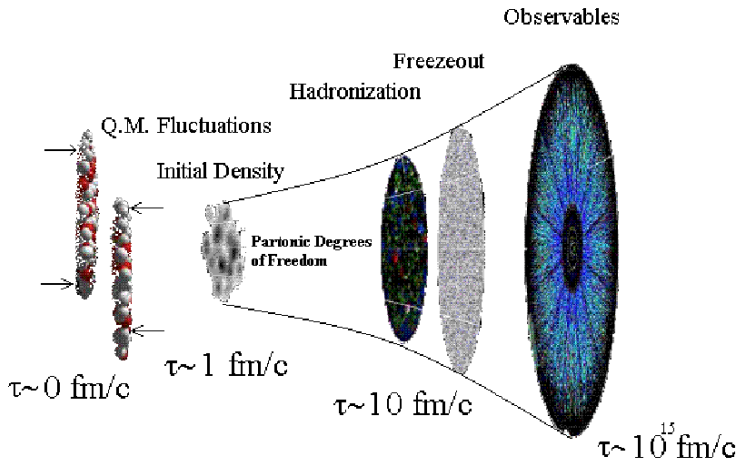

Figure 1.1: Stages in a Relativistic Heavy Ion Collision. Initial Lorentz contracted nuclei colliding, forming an initial state and evolving with subsequent expansion and cooling. The matter reaches temperature and density for hadronization and finally freezes out chemically and thermally. Particles are detected $\sim 10^{14}$ times the interaction distance away.

The early universe may here serve as a picture of the evolution of pre hadron matter including phase transitions and further hadronization processes and finally freeze-out to observable particles. However, the investigation of matter is the view of present author, thus focussed on the subject

as opposed to contextual meaning as of above. In order to be able to study the processes and conditions described above, the system under study has to be small with a controlled level of complexity. The size of the systems under investigation are certainly microscopic, but system mass *is* of interest on a microscopic level. Also, in order to simulate hadronization, the matter has to "melt" and subsequently break chiral symmetry in order to observe true phase transitions. This requires extreme energies and temperatures ($T \sim 200$) MeV. These conditions are achieved in the modern high energy particle colliders referred to above. Given these conditions, a line of phase transitions and evolution of matter through heating, expansion, cooling and finally hadronization is within reach of the investigator through the detected particles (Fig. 1). The observables available are usually momentum and energy. With an addition of statistical/computational work, the identification of particle species has become feasible. Connected is the spatial fixation of the observables, which makes observables related to geometry possible.

Modern day physics may be seen upon as the investigation of matter. As such, matter, or the constituents of matter has to be investigated in theoretical models and also in the laboratory. Investigating matter in the lab is a complex and not completely determinable process. Models for particle collisions have to be derived before any work on the actual colliders can be done. The models provide data for the preparations of the specifications when building accelerators and detectors. Further, the colliders are placed in service and data is obtained from experiments, which in turn are used in modelling and tuning the existing models of relativistic particle collisions. Modelling and analysis work related to the collisions are thus of highest interest.

The particle distributions observed from the relativistic heavy ion collisions are observed and combined with accelerator dependent information, and different processes are studied through the distributions. The main observables in the study of relativistic heavy ion collisions and also the main topic of present paper, is the anisotropic flow v_n and transverse momentum spectra. These observables are projections of the particle distribution [10, 11, 12]

$$E\frac{d^3N}{d^3p} = \frac{1}{2\pi}\frac{d^2N}{p_T dp_T dy}\left(1 + \sum_{n=1}^{\infty} 2v_n(p_T, y)\cos[n(\phi - \phi_n)]\right). \tag{1.1}$$

The invariant transverse momentum spectra is denoted $\frac{dN}{p_T dp_T}$, where the transverse momentum is denoted p_T and the particle rapidity is denoted "y". The particle azimuth is denoted ϕ and the flow reaction plane ϕ_n. We usually identify a symmetry plane, the event plane, which can be view as the "x-z" plane with the z-axis lying in the direction of the beam. The "reaction plane" is thus viewed as the "true event plane", which is approximated as

the event plane. The impact parameter "b" which defines the "overlap" of the nuclei when colliding is thus defined to be oriented along the "x"-axis. Further, we define the participant axis which is oriented along the main axis of the elliptic shaped participant distribution thus defining the fluctuations around the reaction plane.

The azimuthal anisotropy observable (flow) is then denoted $v_n(p_T, y)$ [11, 12]. The azimuthal anisotropy is then the projection

$$v_n(p_T, y) = \langle \cos(\phi - \Psi_n) \rangle. \tag{1.2}$$

The first term in the expansion is called "directed flow", the second term is called "elliptic flow", the third "triangular flow" and the fourth is called "hexadecapole flow". The fifth term is referred to as pentagonal flow and the sixth term is thus the hexagonal flow. In Fig.1, we see the "participants" as coloured circles. The participants form a body at each collision with a symmetry axis, referred to as participant axis in the figure.

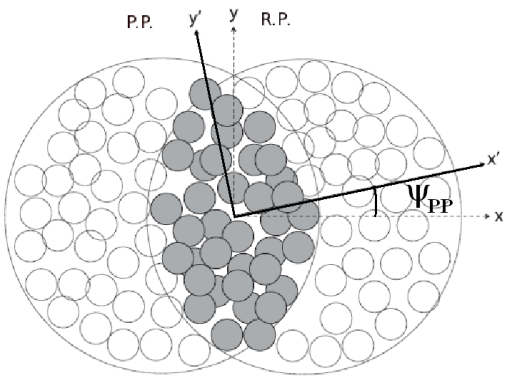

Figure 1.2: Reaction plane(RP) and participant plane(PP). Participant nucleons are in colour.

This axis will fluctuate from event-to-event. It will in general deviate from the reaction plane. This will reflect on the observed flow. The flow in the participant plane will then be larger than in the reaction plane. The shape around the principal axis is said to be at first elliptic at first approximation. There are deformations to this elliptic shape, due to the non uniform distribution. These deformations are represented as the cosine projections of (1.1). In the calculations these deformations provides distinct features of the distributions which will prove essential in understanding the flow in particular and heavy ion collisions in general. The flow is commonly

examined as a function of the initial conditions, i.e. the isotropic distribution of matter, characterized by the eccentricity. The eccentricity ϵ for the n:th mode is defined by the matter distribution

$$\epsilon_n e^{in\Psi_n} = -\frac{\langle r^n e^{in\phi}\rangle}{\langle r^n\rangle}, \tag{1.3}$$

where the event pane angle is denoted by Ψ and the azimuth ϕ. The eccentricity of second order is written

$$\epsilon = \frac{\langle y^2 - x^2\rangle}{\langle x^2 + y^2\rangle}. \tag{1.4}$$

The eccentricity is roughly proportional to the elliptic flow [13]. The eccentricity, or spatial anisotropy definition above is certainly not the only existent, but maybe the easiest to interpret. This anisotropy is then evolved into phase space and further on observed in the particle detectors.

Assuming a spherical distribution, will make the eccentricity (1.3) evaluate to zero. The event-by-event fluctuations will introduce an odd part in the matter distribution, which will yield odd eccentricities not consistent with zero. These fluctuations will then evolve into odd flows, i.e. the odd number terms in (1.2). The odd flows are thus not dependent on ellipticity or centrality in the same way as even flows. The density of the matter distribution *will* influence the momentum transfer, thus displaying weak and maybe non-monotonous behaviour. Anisotropic flow develops out of the in-collision produced initial conditions. The matter is distributed in a, at first approximation, almond like shape. Since this participant distribution displays pressure gradients, which are largest in the (negative) direction of the impact vector, or the minor axis of the participant ellipsoid, the flow, or momentum will build up with continuity reasoning according to

$$\partial_\nu J^\nu = 0 \Leftrightarrow \nabla\rho \cdot \mathbf{v} = \frac{\partial\phi}{\partial t} - \rho\nabla \cdot \mathbf{v}. \tag{1.5}$$

Thus, the flow builds up fastest parallel to the pressure gradient [10]. This anisotropy will evolve in momentum space while subsiding in spatial space thus giving us the momentum anisotropy with respect to the symmetry plane of the particle distribution.

For the lower end of the momentum spectra, we will have a predominantly hydrodynamic evolution due to thresholds associated with hard processes, i.e. in the range $p_T \lesssim 1$ GeV. For higher momentum, the dominant particle production mode is fragmentation. The flow in that regime is decreasing due to the path length dependent energy loss effect having its origin in hard rescattering in the media [14], which is not dependent on pressure gradients in first order. Along with these production modes are the decays, which scatters the distribution thus affecting the observed distribution. The

decays are to a degree coupled with the coalescence processes in the hydro dynamical regime, thus contributing to the scaling behaviour between mesons and baryons. The matter distribution will eventually "freeze out", due to the expansion which makes the matter more dilute and cooler (Fig. 1.3).

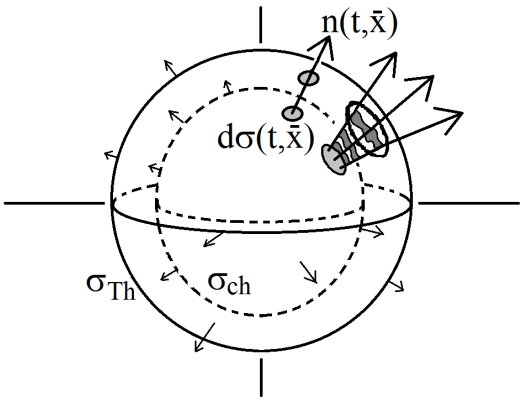

Figure 1.3: Sketch of fireball freeze out surfaces. The inner surface is the chemical freeze out surface and the outer surface is the thermal freeze-out surface.

When the matter reaches the specific chemical freeze-out temperature, T_{ch}, the matter gets fixed in its chemical composition. Cooling further, the thermal freeze-out temperature, T_{th}, is reached and the particles seize to exchange energy and thus the distribution gets frozen out thermally. The particle distribution (1.1) is then completely determined and a particle yield with a predominately soft spectra i.e. low transverse momentum dominated ($p_T < 1$ GeV), is observed at the detector some 10^{14} times the interaction distance away. The angles of emission is strongly correlated and thus observed as described above (1.2).

The initial conditions for the matter produced are possible to study in observing the particle distributions and anisotropy. The fluctuations in the initial conditions depend on initial partonic microscopic interactions which determine the matter distribution, which will evolve through several phase transitions into observed particles. Fluctuating initial conditions produces odd flows, which depends weakly on centrality. Even flows, on the other hand depends strongly on centralities, or ellipticity. Some additional features of the particle detectors can also be used, e.g. calorimeter data from outside the main detector, which aides in determining the collision centrality.

The evolution of the produced matter is also possible to study along with the equation of state for the matter. The in media interactions are of interest. An aspect of the interactions is radiative losses in the media when particles traverse the matter and other hard processes. These in media

losses are a fairly direct observable. A direct hard observable is jets, which at the moment are separable for $p_T > 10$ GeV. Also particle decays and recombination takes place during the matter evolution, where most of the recombination occurs during the early stages of the matter evolution $\tau <$ 5 fm. Decays and recombination are observed through modelling of the processes and the experimental distribution.

As mentioned, phase transitions are likely to take place during the evolution of the strongly interacting matter. Chiral symmetry restoration and deconfinement are then related phenomena, given the quantum fluid paradigm with disassociated partons. These processes are visible in observables such as the anisotropic flow and connected multiparticle correlators. Also, the rôle of hard processes such as jets can be investigated through the transverse momentum spectra and the azimuthal anisotropy, i.e. flow. The hadronization process is taking place before the chemical freeze out, where the chemical composition is fixed. After the chemical freeze out, the distribution scatters thermally, and subsequently seizes to interact and freezes out thermally, thus free streaming for 10^{15} times the interaction length of the fireball. The relativistic heavy ion collisions thus provide us with a laboratory where strong interactions and various phenomena involving these interactions are studied.

In studying the matter evolution, the modern methodology is to implement a hydro dynamical evolution thus treating the produced matter as a hydro dynamically governed fluid. This fluid might be hypothesized to possess a viscosity not consistent to zero. The viscosity is thus modelled within the hydro dynamical evolution, and the observed spectra and anisotropy are compared to experimental data in order to evaluate the present model. The viscosity can then be interpreted as a manifestation of micro dynamics in the interacting media, i.e. collisional and radiative processes. The viscosity is usually put in terms of relaxation times for the interacting matter, thus quantifying the minimal interaction distance.

Relevant research for the specific field has been ongoing since 1956 [15]. This is by present author recognized as the first attempt of an abstraction of the micro dynamics of the collisional process. The language of relativistic hydrodynamics, is a way of abstracting the micro interactions of partonic matter in terms of the collective variables of hydrodynamics, e.g. [16, 17, 18, 19, 20, 21]. The hydrodynamics is still "fine" enough to describe the microscopic $R \sim 10$ fm. matter in a physically sound way.

The hydrodynamic paradigm has been developed continuously since the first attempts. Analytical solutions has been found [22], even for viscous hydrodynamics [23, 24]. The use of computers has made the hydro dynamical models more elaborate including viscosity and realistic in media interactions. The common use of computer clusters has further boosted the computational power available and thus the possibilities for implementing micro interactions and fine structure. In connection with the ability to evolve a distinct state, the initial conditions are simulated.

The initial conditions are simulated in two main physical models. The Glauber model is a geometric model [25, 26, 27, 28], involving a lower degree of sophistication, however in common use and performing fairly well. The Colour Glass Condensate approach is a model based on chromo dynamic concepts and is commonly preferred when simulating realistic initial conditions [29, 30, 31, 32]. The present CGC models are of today not delivering magnitudes of initial conditions in accordance with the present acknowledged evolution models. Given the evolution models, the CGC models yields initial conditions (eccentricities), which are elevated relative e.g. Glauber model generated initial conditions [29, 32]. The ability to generate the initial conditions provides the necessary fluctuations of the initial conditions to reproduce the anisotropic flow and spectra [33, 34, 35, 32].

Aspects of termalization and phase transition and evolution of initial conditions are also investigated through the implementation of realistic initial conditions [36, 37, 38]. The evolved matter is then hadronizing and freezes out and scatters in the late stages. The late scattering stages has been found, through present model and others to be more problematic to simulate, likely as a consequence of late stage scattering [39, 40, 41]. Flow of the first six orders have been observed both at RHIC [42, 43, 44, 45] and LHC [46, 47, 48, 49]. The relevant experimental programs started at Brookhaven (AGS, $\sqrt{s} = 4.75$ GeV)[50, 51, 52] during the 1990's and at CERN with the Super Synchrotron (SPS, $\sqrt{s} = 17.2$ GeV) [53, 54]. The program continues at the Brookhaven Relativistic Heavy-Ion Collider (RHIC, $\sqrt{s} = 200$) GeV. The highest available energy for ion-ion collisions is at present time at the LHC ($\sqrt{s} = 2.76$) TeV.

This progress led to the "perfect fluid" hypothesis in 2005 [33, 55, 56, 57] and the paradigm shift toward the plasma picture of quark gluon plasma (QGP) [58, 59] which describes a phase of deconfined quarks and gluons. This phase is assumed to survive out to ~ 10 fm (Fig.1).

The observed transverse momentum spectra are experimentally extracted commonly and also reproduced with high accuracy for identified particles, e.g. $\pi^{\pm}, \mathrm{p}, \bar{\mathrm{p}}, \mathrm{K}^{\pm}$, and inclusive spectra [49, 60, 61, 62]. The predictions are almost as accurate for the fluctuating, non-extensive regime as for the thermal transverse regime [63, 64, 65]. The azimuthal anisotropy is also connected to the particle spectra. The projection of flow has been systemized in the early 1990s and is presented as a stable observable since then [46, 66]. The higher harmonics has been extracted only in the last few years [47, 49, 48, 67]. Associated with them are the plane- and particle correlators [68].

The energy scale reached in the relativistic heavy ion collisions of today ($\sqrt{2.76}$ TeV), provides an unprecedented level of resolution, which provides for deeper investigations of matter, e.g. investigation of coalescence and mass generation processes. This makes the work concerning the investigation of hadronization and mass generation relevant in order to push the

development of observables related to hadron formation forward.

This thesis treats the generation of particle spectra and anisotropy in relativistic heavy ion collisions. The investigation of the matter produced in the relativistic heavy ion collisions, is a mean of studying strongly interacting matter and matter evolution along with hadrogenesis. Through the observation of the particle distributions, aspects of matter evolution and detection are studied. Factorization and separation is the main topic of this thesis. The different production modes are analyzed and observables are derived in order to probe the hadronization deeper.

The azimuthal anisotropy and the transverse momentum spectra are dependent on particle production modes i.e. the distribution has different characteristics coming from a jet as opposed to being produced in a purely hydro dynamical way. It also has specific characteristics coming from directly produced particles versus decayed particles. The difference is mainly in particle coherence, which manifests itself in the specific distributions. The distributions display different fundamental behaviour, dependent on the governing particle production mode. The thermal exponential distribution is commonly seen as the soft mode. The higher transverse momentum regime displays a power law behaviour, which characterizes harder, non-equilibrium, fluctuating fragmentation processes.

This coherence might be observed in terms of particle correlators. The observation of correlating angles or particles also gives an indication of the mentioned initial conditions and also on the evolutionary specifics. The correlator can often be viewed upon as level of factorization of higher order flows. These correlators depend on the level of particle coherence, thus being associated to different production processes. The higher order flows, i.e. pentagonal and hexagonal flow, simulated in lower order planes, are related to particle correlators and level of factorization in this thesis. These correlators are then viewed as observables related to hadronization.

In investigating the matter evolution and the different modes of hadronization, the particle distribution can be examined within the constitutive quark number scaling model. This model makes the assumption of constitutive quarks carrying momentum, which is scaled with the number of constituents and no attention is given to the multitude of non linear effects is made. The model also makes an attempt to display the flow in terms of transverse kinetic energy, thus centering the flow. The flow may then be investigated in terms of mesons and baryons and compared, thus providing means of making conclusions regarding particle production, usually as a violation of the constituent quark number scaling.

The event planes of different order “n”, from (1.1) display different characteristics. I.e. the flow of second order is dependent on number of participant particles and the level of ellipticity, i.e. centrality while the third order flow is dependent on event-by-event fluctuations in the initial conditions. Thus, the fluctuating dependent flow is less dependent on centrality.

However, observed flow *do* depend on the ability of the matter to transfer the fluctuations to freeze out and observed flow and spectra. The ability of evolving fluctuation is determined by the viscosity (Fig. 1.4), which abstracts the matter relaxation times, thus making the fluctuating triangular flow an observable, which is dependent on viscosity.

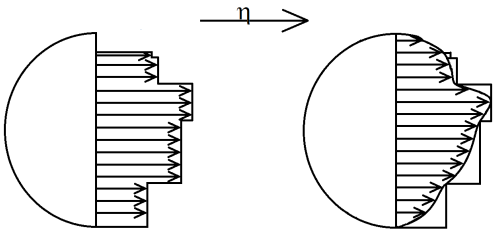

Figure 1.4: Viscous flow. Non viscous flow on the left and viscous flow on the right side.

This interesting dependence will however *not* be discussed in present paper, mostly due to the implementation of realistic initial conditions. Despite the lack of initial conditions, the triangular flow is simulated with great precision in present paper due to an implemented triangular scalar event plane.

The simulation of higher order flow in lower order planes, calls for the implementation of the elliptic and triangular event plane and possibly the pentagonal event plane also. The elliptic and triangular flow holds most of the physics in relativistic heavy ion collisions. Most of the evolutionary mechanics and large parts of the initial conditions are necessary to implement in order to reproduce the flows and the transverse momentum spectra. The elliptic and triangular flows are also the largest in magnitude, thus carrying the most (at least conceptual) weight. This is the reason of the focus on these two flows along with the pentagonal flow. Thus provide the possibility of simulating non-linear flows. The flows will then be reproduced for the centralities $(0 - 50\%)$, which are relevant for present model.

Also treated in connection with the azimuthal anisotropy are the transverse spectra of identified particles. The spectra are a direct observable which gives the number of observed particles dependent on transverse momentum, which has different characteristics dependent on production modes.

In simulating flow and spectra for identified particles, the possibility of projecting different production modes opens up. Of interest is the influence of particle decays on flow and the effect of the different particle production modes on the constituent quark number scaling, which is a way of normalizing the flow for different particles, thus make higher order conclusions.

The effect of in medium scattering and recombination is of interest and can also be studied in higher order flows, where analogies to particle correlators are made. The correlators measure the level of particle coherence in

general, thus indicating the origin of the particles for different regimes. It is argued that the higher order harmonics can be used as an observable for particle decays and confinement. In general the coherence of the generated particles is studied and the work is intended to lay the foundation for a more intricate flow analysis. In line with recent publications, attempts are made to simulate correlators utilizing several event planes, and also study the associated compound flow, which represents the relevant factorization of the higher order flows.

In order to study higher harmonics, the flow has to be calculated with respect to different symmetry planes, which has to be determined and/or approximated. The various aspects of determination of symmetry planes and the statistical work needed will also be treated.

To make this high energy relativistic collision digress somewhat more complete, the cross sections for identified particles are calculated and tuned. In using the calculating software, various features of the origins of matter in general and relativistic heavy ion collisions in particular are discovered. Again, the highly complex software in use (HYDJET++) [69] proves to be not just a quantitative predictional tool, but also an invaluable test bench or learning tool in the daily work. A high degree of accuracy is achieved in comparison with the available experimental data. The general aim of present research group is the investigation of flow in all its manifestations. Therefore the calculation and the tuning of the code are done in a heavy ion, high energy, setting (Pb+Pb). This might be a setback from an *ab initio* tuning approach. On the other hand accuracy is achieved more readily and the tune includes vital collective effects i.e. shadowing, relevant energy loss effects etc.

The main part of this thesis is the calculation of anisotropic flow using a simulation package , which implements parameterized hydrodynamics combined with a hard process generator, including *in materia* energy loss and jet production. This combined with an implementation of particle decays provide the simulation tool used for the MC-calculations done in this thesis.

An important remark is that the fluctuations provide us with information about *earlier* stages. In this thesis, with the use of present model, the particles are fluctuating in a more artificial way and the implementation of more realistic initial conditions is in the future. Higher harmonics are highly fluctuative in their origin, and are thus expected to display discrepancies, in particular when simulated in second order as of the case in present paper.

Chapter 2

Theory

2.1 Introduction

The heavy ion collisions produce a distribution of hot and dense matter. This matter is considered to be primordial, i.e. due to evolve into observable matter or hadrons. The matter distribution is thus observed and the evolution of the matter and possible observables connected to it has to be hypothesized in order to investigate the evolution.

The initial matter is usually assumed to evolve hydro dynamically [70, 15]. This evolution is driven by pressure gradients, which are formed in the initial stages. In this thesis, a brief introduction to relativistic hydrodynamics is given along with some qualitative consequences.

When matter is thermalized post collision, the matter evolves due to hydrodynamics. The matter displays a disassociated behaviour in the first $\sim$ 5 fm/c after the collision. Here, large parts of the hadronization takes place to a large part, mostly in recombination processes, and we get to study the theory of strong interactions, which is briefly reviewed in this thesis.

The matter evolves further under the hypothesized hydro dynamical evolution. The in media partons scatter of the matter, thus deflecting spatially and transfer momentum, this *in materia* modulation is of highest importance and governs the resulting flow in a qualitative way. The matter modulations due to parton scattering are treated in this thesis, thus examining the strong interactions of matter.

The in media radiated gluons are further scattered and also hadronizing which produces visible effects of the secondary scattering in the observed distribution. Jets are produced in the media for transverse momentum above $\sim$ 1 GeV. These jets may traverse the media, thus scattering in the way mentioned, losing energy and possibly getting thermalized in the matter. The jets may also lose some of its energy through radiation into the matter and subsequently "escape" from the participant matter and get observed as hadronized matter in the detector.

The matter gets chemically frozen out and thus fixes its relative chemical composition, while scattering thermally, thus transferring momentum and finally freezes out to its thermal distribution and free streams to the distant detector. Here, the observed particle yield has to be analyzed in a systematic way in order to serve as standardized observables. The systematization of the observables is also treated in this thesis in order to understand the concept of flow and the methodology of observing distributions in the particle detectors.

2.2 Analysis

The flow analysis of heavy ion collisions starts with definitions and systematization of variables.

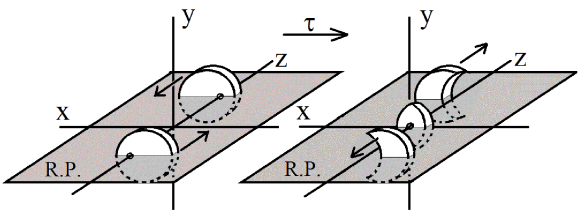

Figure 2.1: Reaction plane. Heavy ions approach each other, interact and pass through each other (left). An almond shaped body of participants is formed. This matter distribution left in the middle, is the subject of interest.

A coordinate system has to be defined. Cartesian coordinates are used where the beam direction points along the z-axis and the positive x-axis is parallel to the impact vector i.e. the short axis of the matter distribution. The y-axis is then given to point in the long-axis of the theoretical-symmetric participant matter distribution. The reaction plane displayed in Fig. 2.1 is thus determined for each collision event.

The (realistic) asymmetry in the initial particle distribution around the reaction plane makes the center of mass plane fluctuate around the reaction plane. This fluctuating plane in Fig. 2.2 is referred to as the participant plane.

The produced matter transfers through the plasma phases and later freezes out (hadronizes) and is observed as particle distributions. The azimuths of the observed particles are then defined as the azimuth relative the beam. In order to derive some distinct interpretable observables, one has to standardize the flow analysis. In general, the analysis is based on the Fourier decomposition of the particle distribution (2.1) [11, 12]. The particle azimuthal angle is denoted ϕ, the order of harmonic n and the true

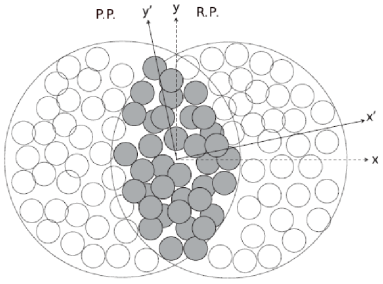

Figure 2.2: Participant (P.P.) and reaction plane (R.P.). The participants, marked with dark colour forms a volume which moment plane fluctuates around the reaction plane event-by-event.

reaction plane angle Ψ_r

$$E\frac{d^3N}{dp^3} = \frac{d^3N}{p_T dp_T dy d\phi} = \frac{1}{2\pi}\frac{d^2N}{p_t dp_t dy}(1+\sum_{n=1}^{\infty} 2v_n(p_T,y)\cos[n(\phi-\Psi_r)]). \quad (2.1)$$

Here, the transverse momentum is denoted p_T and the longitudinal rapidity y. The distribution (2.1) is transformed to rapidity dependence with [71]

$$y = \tanh^{-1}(\frac{p_z}{E}) \Leftrightarrow \frac{1}{\cosh^2(y)}\frac{dy}{dp_z} = \frac{1}{E} \Leftrightarrow \frac{dy}{dp_z} \simeq \frac{1}{E} \quad (2.2)$$

$$E\frac{d^3N}{dp^3} = E\frac{d^3N}{dp_x dp_y dp_z} = \frac{d^3N}{dp_x dp_y dy} = \frac{d^3N}{p_t dy dp_t d\phi}. \quad (2.3)$$

The distributions (2.1) and (2.3) are compared and the angular distribution is thus

$$\frac{dN}{d\phi} = \frac{1}{2\pi}\left(1+\sum_{n=1}^{\infty} 2v_n\cos[n(\phi-\Psi_n)]\right). \quad (2.4)$$

The $\langle\cos[k(\phi - \Psi_k)]\rangle$ is calculated with the distribution (2.4).

$$\begin{aligned}\langle\cos[k(\phi - \Psi_k)]\rangle &= \int_0^{2\pi} d\phi \frac{1}{2\pi}\left(1 + \sum_{n=1}^{\infty} 2v_n \cos[n(\phi - \Psi_n)]\right) \\ &\times \cos[k(\phi - \Psi_k)] \\ &= \int d\phi \frac{1}{2\pi}\left(1 + \sum_{n=1}^{\infty} 2v_n \cos[n(\phi - \Psi_n)]\right) \\ &\times \cos[k(\phi - \Psi_k)] \\ &\int d\phi (\frac{1}{2\pi}(\sum_{n=1}^{\infty} v_n \cos[(n-k)\phi + (n\Psi_n - k\Psi_k)] \\ &\times \cos[(n+k)\phi - (n\Psi_n + k\Psi_k)]) \\ &= v_k.\end{aligned} \tag{2.5}$$

The coefficients are viewed as a means of observing the azimuthal anisotropy of the particle distribution. These coefficients are then referred to as "flow" or "azimuthal anisotropy". Given the Fourier series above (2.1), the reaction plane for each coefficient has to be determined, or at least estimated. This estimated reaction plane is referred to as the event plane. The periodicity is implemented as a simple division of the unit circle. Experimentally, a finite number of particles are used as a statistical base for the determination of the event planes [12]. To calculate the event plane, a weighted sample (ρ_i) of particles (i) is used in the estimation. It can be done separately for each harmonic. With a base of a finite number of particles, the event flow *vector* $\mathbf{v_n}$, is defined in the transverse plane by [11, 12]

$$\begin{aligned}|\mathbf{v}_n| \cos(n\Psi_n) &= \sum_i \rho_i \cos(n\phi_i) \\ |\mathbf{v}_n| \sin(n\Psi_n) &= \sum_i \rho_i \sin(n\phi_i),\end{aligned} \tag{2.6}$$

where the azimuth of the k:th particle is denoted by ϕ_k. This will provide us with a statistical estimation of the reaction planes, i.e. the event planes. In determining the weights in (2.6), depending on the hemisphere where the particle is observed, the sign of the weight is altered due to an assumed π-rotational symmetry. Reflection symmetry implies that the particle distribution is equal for the forward and backward hemisphere i.e. invariant to a rotation of π. The signs of the weights ρ for the backward hemisphere is thus reversed. In order to optimize the resolution of the reaction plane, different weights are used. The weights might be mass, transverse momentum or even flow. One might also use the kinetic energy of the particles as statistical weight or the rapidity [12]. Acceptable choices of weight could be unity [72] and maybe the pseudo rapidity η as weights for the odd harmonics for $|\eta| > 1$ [56]. The weights for even and odd planes are also different.

The optimal weights are proportional to v_2, but a common choice would be $\rho = p_T$ for $p_T < 2$ GeV and flat for higher momentum [56, 72].
In order to calculate the resolution of the event plane, the starting point is the central limit theorem i.e. the deviation is assumed to resemble a gaussian with deviation σ is $\sigma^2 = \frac{1}{2N}\frac{\langle w^2\rangle}{\langle w\rangle^2}$. The distribution (2.7) is then assumed to be centered around the mean flow parameter $\bar{\mathbf{v}}$ [11, 12]

$$\frac{d^2P}{v_n dv_n d\Psi} = \frac{1}{2\pi\sigma^2}\exp\left(-\frac{(\mathbf{v}_n - \bar{\mathbf{v}}_n)^2}{2\sigma^2}\right) = \frac{1}{2\pi\sigma^2}\exp\left(-\frac{v_n^2 + \bar{v}_n^2 - 2v_n\bar{v}_n\cos(\Psi)}{2\sigma^2}\right). \tag{2.7}$$

The variables are the x-axis flow vector which is denoted $\bar{\mathbf{v}}_n$ and the fluctuating particle flow vector is denoted by $\mathbf{v}_n$. The v_n is the magnitude of corresponding flow vector $\mathbf{v}_n$. The angle between x-axis and reaction plane is denoted $\Psi = n\left(\Psi_n - \Psi_R\right)$. The resolution of the $m = kn$ event plane, i.e. the resolution in plane m using plane n, is defined as

$$\mathrm{Res}\left(m\Psi_n\right) = \langle\cos\left(kn\left[\Psi_n - \Psi_R\right]\right)\rangle. \tag{2.8}$$

The resolution is then calculated using the distribution (2.7). This yields the expression for the resolution

$$\begin{aligned}\langle\cos\left(kn\big[\Psi_n - \Psi_R\big]\right)\rangle =& \frac{1}{2\pi\sigma^2}\int d\left(n\left(\Psi_n - \Psi_R\right)\right) dv_n v_n \cos\left(kn\left[\Psi_n - \Psi_R\right]\right) \\ &\times \exp\left(-\frac{v_n^2 + \bar{v}_n^2 - 2v_n\bar{v}_n\cos\left(n\left[\Psi_n - \Psi_R\right]\right)}{2\sigma^2}\right).\end{aligned} \tag{2.9}$$

The integral (2.9) is solved as [12]

$$\langle\cos\left[kn\left(\Psi_n - \Psi_r\right)\right]\rangle = \frac{\sqrt{\pi}}{2\sqrt{2}}\chi_n\exp(-\chi_n^2/4)\times[I_{(k-1)/2}(\chi_n^2/4) + I_{(k+1)/2}(\chi_n^2/4)], \tag{2.10}$$

with the modified Bessel function $I_k\left(x\right)$ of first kind and order k. The flow to deviation ratio is denoted $v_n/\sigma = \chi_n$. The anisotropic flow with respect to the real reaction plane is then

$$v_n = \frac{v_n^{obs}}{\langle\cos\left[km\left(\Psi_m - \Psi_r\right)\right]\rangle}. \tag{2.11}$$

This means that the coefficients always increase when they are modified when accounting for the resolution. Trivially, using the event plane for the particular coefficient will maximize it. Using a harmonic "n" significantly different from the "reaction harmonic", will of course deteriorate the resolution. Here, the resolution parameter $\chi_m = v_m\sqrt{N_m}$ is defined such as the resolution parameter for the full event is $\chi = \chi_m\sqrt{N/N_m}$. Given the hypothesis of a causal evolution of the produced matter in heavy ion collisions,

the initial conditions must be established in order to predict the final flow. Given the initial conditions, the hydro dynamical evolution equations [73] for the produced matter in the heavy ion collisions can be solved, or iterated. The evolved matter will further lead to realization of the observed matter through non-trivial final processes described in section 2.4 and section 2.3, where it is observed as distributions. In observing the yields, hypothesises regarding initial conditions, temporal and spatial evolution, freeze-out processes and observation, can be made. Comparing the eccentricities and initial conditions with the evolved state of the matter would provide a vast amount of information. This situation demands factorization and alternate hypothesizing in order to move the understanding forward. Large parts of present day research is focussed on the initial conditions [74, 34, 75, 76, 77]. The initial matter is spatial-temporally complex. It consists of frozen gluon states and nucleons and the produced GLASMA [36, 37, 32] matter also determines properties as termalization and transition to gluon plasma. The geometric initial condition when simulating anisotropic flow is defined in terms of eccentricity. The eccentricity is characterized as the deviation from a spherical distribution and has its origin in two processes. First, the geometric distribution of the participants due to the overlap of the ionic wave functions.The second origin of eccentricity is the microscopic interactions between matter constituents. The eccentricity may be defined in terms of the geometric modes of the observed distribution. The eccentricities ϵ_n are defined in terms of moments as [78]

$$\epsilon_n e^{in\Psi_n} = -\frac{\langle r^n e^{in\phi} \rangle}{\langle r^n \rangle}. \tag{2.12}$$

Here, the participant plane angle is denoted by Ψ_n, the ϕ denotes the azimuth and the radius is denoted by r. It is seen that the odd eccentricities evaluates to zero for a spherical symmetric distributions centered in the origin. The observation of odd harmonics is thus interpreted as an indication of a non-spherical distribution of the initial matter distribution [78, 47]. In order to calculate the expectation value ($\langle\rangle$), the energy density distribution calculated in the mean on the transverse plane as

$$\epsilon_n e^{in\Psi_n} = -\frac{\int r^n e^{in\phi} \rho\left(\mathbf{r}\right) dA}{\int r^n \rho\left(\mathbf{r}\right) dA}. \tag{2.13}$$

The eccentricity may also be factorized as $\epsilon_n e^{in\Psi_n} = \epsilon_x + i\epsilon_y$. The x-component is thus the reaction plane component. Relevant eccentricities

are written down for reference

$$\epsilon_2 = -\frac{\langle r^2 \cos(2[\phi-\Psi_2])\rangle}{\langle r^2\rangle} \tag{2.14}$$

$$\epsilon_3 = -\frac{\langle r^3 \cos(3[\phi-\Psi_3])\rangle}{\langle r^3\rangle} \tag{2.15}$$

$$\epsilon_4 = -\frac{\langle r^4 \cos(4[\phi-\Psi_4])\rangle}{\langle r^4\rangle} \tag{2.16}$$

$$\epsilon_5 = -\frac{\langle r^5 \cos(5[\phi-\Psi_5])\rangle}{\langle r^5\rangle} \tag{2.17}$$

$$\epsilon_6 = -\frac{\langle r^6 \cos(6[\phi-\Psi_6])\rangle}{\langle r^6\rangle}. \tag{2.18}$$

The higher order (cumulant) terms can be made irreducible by subtracting the lower order combinations of moments. This will yield a cumulant form of eccentricities. At the very least the subtraction reveals the eccentricity substructure. The lower order combinations are subtracted with their combinatoric weights as [79]

$$\mathcal{E}_2 = \epsilon_2 e^{i2\phi_2} = -\frac{\langle X^2\rangle - \langle X\rangle\langle X\rangle}{r^2} \tag{2.19}$$

$$\mathcal{E}_3 = \epsilon_3 e^{i3\phi_3} = -\frac{\langle X^3\rangle - 3\langle X^2\rangle\langle X\rangle - \langle X\rangle\langle X\rangle\langle X\rangle}{r^3} \tag{2.20}$$

$$\mathcal{E}_4 = \epsilon_4 e^{i4\phi_4} = -\frac{\langle X^4\rangle - 3\langle X^2\rangle^2 - 4\langle X^3\rangle\langle X\rangle - \langle X\rangle\langle X\rangle\langle X\rangle\langle X\rangle}{r^4} \tag{2.21}$$

$$\mathcal{E}_5 = \epsilon_5 e^{i5\phi_5} = -\frac{\langle X^5\rangle - 10\langle X^2\rangle\langle X^3\rangle - 5\langle X^4\rangle\langle X\rangle - 15\langle X^2\rangle\langle X^2\rangle\langle X\rangle}{r^5} \tag{2.22}$$

$$\frac{-\langle X^2\rangle\langle X\rangle\langle X\rangle\langle X\rangle - \langle X\rangle\langle X\rangle\langle X\rangle\langle X\rangle\langle X\rangle}{r^5} \tag{2.23}$$

$$\mathcal{E}_6 = \epsilon_6 e^{i6\phi_6} = -\frac{\langle X^6\rangle - 15\langle X^4\rangle\langle X^2\rangle - 10\langle X^3\rangle^2 - 30\langle X^2\rangle^3 - 6\langle X^5\rangle\langle X\rangle}{r^6} \tag{2.24}$$

$$-\frac{60\langle X^3\rangle\langle X^2\rangle\langle X\rangle - 90\langle X^2\rangle^2\langle X\rangle\langle X\rangle - 30\langle X^2\rangle\langle X\rangle\langle X\rangle\langle X\rangle\langle X\rangle}{r^6}. \tag{2.25}$$

Where $X = re^{i\phi}$ and the ϕ_n denotes the participant planes.

2.2.1 Flow Expansion

As stated above, the eccentricity evolves under hydrodynamics and subsequently freezes out to the observed distributions. Given this we assume a link w_n between the eccentricity ϵ_n and the corresponding flow. The complex flow

$$V_n = v_n e^{in\Psi_n}, \tag{2.26}$$

can be expanded in terms of cumulants [80]

$$V_n = \mathcal{E}_n \frac{w_n}{\epsilon_n} + \sum \mathcal{E}_\alpha \mathcal{E}_\beta \frac{w_n^{\alpha\beta}}{\epsilon_\alpha \epsilon_\beta} + \sum \mathcal{E}_\alpha \mathcal{E}_\beta \mathcal{E}_\gamma \frac{w_n^{\alpha\beta\gamma}}{\epsilon_\alpha \epsilon_\beta \epsilon_\gamma} + \dots. \tag{2.27}$$

The first order term is usually characterizing. However, in present paper, an attempt to investigate non linear terms is made in line with [80].

2.2.2 Compound flow

In investigating the higher order response, the starting point is the initial conditions of the matter evolution. The energy distribution is characterized by the cumulants, or eccentricities in (2.14). In order to investigate the higher order terms describing the initial conditions, and later, the flow, the flows are examined in terms of eccentricities and the matter answer to the initial conditions. To a first approximation, the anisotropic flow is linear in its composition. Higher order terms can however be examined including higher order terms in the eccentricity-flow expansion [80]. The definitions (2.26) and (2.27) [79] is used in order to investigate the impact of lower order planes on higher order flow. For, e.g. the pentagonal flow, the cumulant expansion is

$$\begin{aligned} V_5 = v_5 e^{i5\Psi_5} &= \epsilon_5 e^{i5\phi_5}\frac{w_5}{\epsilon_5} + \epsilon_3\epsilon_2 e_3^{i3\phi_3} e^{i2\phi_2}\frac{w_5^{23}}{\epsilon_3\epsilon_2} + \epsilon_4\epsilon_1 e_3^{i4\phi_4} e_1^{i\phi_1}\frac{w_5^{14}}{\epsilon_4\epsilon_1} \\ &+ e^{i(2\phi_2+2\phi_2+\phi_1)} w_5^{221} + e^{i(3\phi_3+\phi_1+\phi_1)} w_5^{311} + \dots \\ &\Leftrightarrow v_5 = e^{i5(\phi_5-5\Psi_5)} w_5 + e^{i(3\phi_3+2\phi_2-5\Psi_5)} w_5^{23} + e^{i(4\phi_4+\phi_1-5\Psi_5)} w_5^{14} + \dots \end{aligned} \tag{2.28}$$

The pentagonal flow is thus composed to second order of the answer to eccentricity in the fifth event plane and two second order factors which originates in the first, second, third and fourth event plane. The phase correlations for the flows are factorized in front of the flow answer. The magnitude of the correlation is thus determining the influence of the different terms. E.g. the influence of the non-linear v_2v_3 term in (2.28), is determined by the correlator $\langle\cos(5\Psi_5 - 3\Psi_3 - 2\Psi_2)\rangle$. As a part of the thesis hypothesis, the nonlinear answer $w_5^{23} \rightarrow v_2v_3 \propto \langle\cos(5\phi - 2\Psi_2 - 3\Psi_3)\rangle$ can and will be tested in present paper. The compound flow is also investigated as a "multiparticle", multiplane correlator. The v_2v_3 flow is calculated as

$$\begin{aligned} v_2v_3 &= \int d\alpha d\beta \cos(2\alpha)\cos(3\beta) f(\alpha) f(\beta) \\ &= \int d\alpha d\beta \frac{1}{2}\cos([2\alpha - 3\beta])) + \frac{1}{2}\cos([2\alpha + 3\beta]) \\ &= \langle\cos(2\phi_2 + 3\phi_3 - 2\Psi_2 - 3\Psi_3)\rangle. \end{aligned} \tag{2.29}$$

This expression will be tested as a multiparticle flow correlator for centralities, thus compared with other configurations.

For reference, due to the further investigation of compound flow the

hexagonal flow is also written down using cumulant expansion (2.27)

$$\begin{aligned} V_6 = v_6 e^{i6\Psi_6} &= e^{i6\phi_6} w_6 + e^{i(2\phi_2+4\phi_4)} w_6^{24} + e^{i(\phi_1+5\phi_5)} w_6^{15} + e^{i(3\phi_3+3\phi_3)} w_6^{33} \\ &+ e^{i(2\phi_2+2\phi_2+2\phi_2)} w_6^{222} + e^{i(3\phi_3+2\phi_2+\phi_1)} w_6^{321} + \dots \\ &\Leftrightarrow v_6 = e^{i6(\phi_6-\Psi_6)} w_6 + e^{i(2\phi_2+4\phi_4-6\Psi_6)} w_6^{24} + e^{i(6\phi_3-6\Psi_6)} w_6^{33} \\ &+ e^{i(6\phi_2-6\Psi_6)} w_6^{222} + \dots \end{aligned} \tag{2.30}$$

The hexagonal flow is here truncated to a hexagonal part from its own plane and contributions from second, third and fourth harmonics. The answers $w_6^{33} \to v_3 v_3 \propto \langle \cos(6\phi - 6\Psi_3) \rangle$ is investigated in present paper. Further, the cubic answer of $w_6^{222} \to v_2^3 \propto \langle \cos(6\phi - 6\Psi_2) \rangle$, is also investigated. Also seen here is the corresponding correlators $\langle \cos 6(\phi_3 - \Psi_6) \rangle$ and $\langle \cos 6(\phi_2 - \Psi_6) \rangle$, which of course determines the contribution from the different combination of planes. The cubic elliptic flow is calculated as

$$\begin{aligned} v_2 v_2 v_2 &= \int d\alpha d\beta d\gamma \cos(2\alpha) \cos(2\beta) \cos(2\gamma) f(\alpha) f(\beta) f(\gamma) \\ &= \int d\alpha d\beta d\gamma \frac{\cos(2\alpha)}{2} \left[\cos(2\left[\beta - \gamma\right])) + \cos(2\left[\beta + \gamma\right]) \right] \\ &= \int d\alpha d\beta d\gamma \frac{1}{2} \cos(2\left[\alpha - \beta + \gamma\right])) + \frac{1}{4} \cos(2\left[\alpha - \beta - \gamma\right])) \\ &+ \frac{1}{4} \cos(2\left[\alpha + \beta + \gamma\right])) \\ &= \langle \cos(2\left[\phi_1 + \phi_2 + \phi_3 - 3\Psi_2\right]) \rangle. \end{aligned} \tag{2.31}$$

This provides an interpretation of the cubic elliptic flow. The cube can be view upon as a "three particles" correlating with the Ψ_2 plane. Given an infinitely sharp distribution, the expression (2.31), turns into

$$v_2 v_2 v_2 = \langle \cos(6\left[\phi - \Psi_2\right]) \rangle. \tag{2.32}$$

The expression (2.32), is only reached for a high degree of coherence. That will make the sixth harmonic in the Ψ_2 grow to the magnitude of the cubic elliptic flow. For the case of flow from all processes, the expected value of the hexagonal flow in the Ψ_2 plane may be lower due to lower degree of particle correlation. The hexagonal flow in the Ψ_2 plane, for $p_T < 2$ GeV is hypothesized to be composed of a hydro flow with jets, quenching the flow to a minor degree. In this regime, the particles display approximately the same type of particle production, thus producing the same level of coherence for the region in question. For higher transverse momentum, particles are produced with a higher degree of fragmentation, i.e. jets producing a higher degree of correlation with the hexagonal plane, due to the higher wave number, which couples with scattering from decays and jets, thus producing the

theoretical asymptote (2.32).
The quadratic triangular flow is investigated in the same way

$$\begin{aligned} v_3 v_3 &= \int d\alpha d\beta \cos(3\alpha)\cos(3\beta) f(\alpha) f(\beta) \\ &= \int d\alpha d\beta \frac{1}{2}\cos(3\left[\alpha-\beta\right])) + \frac{1}{2}\cos(3\left[\alpha+\beta\right]) \\ &= \langle \cos(3\left[\phi_1+\phi_2-2\Psi_3\right])\rangle. \end{aligned} \tag{2.33}$$

In this case, the analogue of (2.32), is

$$v_3 v_3 = \langle \cos(6\left[\phi-\Psi_3\right])\rangle, \tag{2.34}$$

for the higher transverse momentum regime. The correlating (2.33), is interpreted as a two particle correlator relative Ψ_3. Hydrodynamics, which produces the same relative flow due to the invariance of level of correlation for all transverse momentum and wave numbers, is likely to produce a scaling for the flow ratios. This may fulfil (2.29), (2.33) and (2.34) and up to a constant.

2.2.3 Eccentricity Fluctuations

Quantifying the fluctuations of the geometric initial conditions is of interest since the fluctuations are a sensitive observable related to the viscosity of the produced matter. The viscosity is in hydrodynamics the anisotrotropy susceptibility for the energy momentum tensor, thus damping fluctuations through the matter evolution (Fig. 2.3). The observed fluctuations in e.g. flow are compared to the hypothesized fluctuations of the initial conditions. In general, the fluctuations will lower the anisotropic flow relative to the case of non-fluctuating initial conditions. In the hydrodynamic picture, the

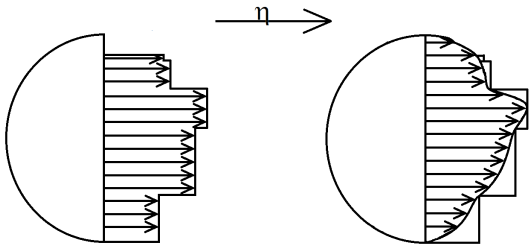

Figure 2.3: Zero viscosity flow (left) vs. viscous flow (right). Arrows denotes velocity field. Flow with shear viscosity, η, smoothens (dampens) velocity gradients.

case of zero viscosity gives the largest flow signal, given the initial conditions. This is due to a minimal mean free path and a minimal termalization

time. Viscosity corresponds to finite cross sections and mean free paths not zero. The odd-flows are then of main interest due to their strong fluctuation dependence. The relationship between eccentricities of different order and different planes are also possible to investigate through the fluctuations of the individual eccentricities. The average of a variable X over *one* event is denoted $\{X\}$ and the mean is denoted $\langle X\rangle$. The eccentricity cumulants (2.13), can then be written in terms of the displacement $\delta_X = \{X\} - \langle X\rangle$ [35]

$$\epsilon_2 e^{i2\phi_2} = -\frac{(X-\delta_X)^2}{r^2} = -\frac{\delta_{X^2} - \delta_X^2 - 2\delta_X\langle X\rangle + \langle X^2\rangle}{r^2} \quad (2.35)$$

$$\epsilon_3 e^{i3\phi_3} = -\frac{(X-\delta_X)^3}{r^3} = -\frac{\langle X^3\rangle + \delta_{X^3} - 3\delta_{X^2}\delta_X - 3\langle X^2\rangle\delta_X + 2\delta_X^3 + 3\delta_X^2\langle X\rangle}{r^3}. \quad (2.36)$$

Here, the displacements are written in terms of their plane of origin. The odd "mean" terms can be set to be zero for a spherical distribution. The cumulants thus show the trivial $\langle X^2\rangle$ dependence, in addition to a fluctuating term in the second order event plane and a second order fluctuation in the first order event plane. The second order cumulant also contains a product of fluctuation times an odd harmonic which can be set to zero. The third order cumulant is here seen to consist of *only* fluctuating terms of first, second and third order in the first three planes. I.e., the third order cumulant and eccentricity are zero without fluctuations.

2.3 QCD

2.3.1 Introduction

Hadronic matter is believed to be made up by quarks. The concept of quarks arose from the need of the group SU(3) seen in the low-mass spectrum for baryons and mesons [81, 82, 83]. The observed baryons are made up of three valence quarks i.e. "observed, constituent" quarks and a postulated fluctuating quark vacuum.

The mesons are correspondingly made up of two constituent quarks. The quarks are fermions and their individual spins combine to the spin of the baryon or meson. The baryon being in a symmetrical state with respect to spin, position and flavour SU(3), thus requires an imposed asymmetric part of the wave function. In order to introduce this asymmetry, an additional quantum number is introduced.

Colour is the new degree of freedom. The colour index can have three different values, i.e. (R)ed, (G)reen and (B)lue as stated. The colour wave function is totally anti symmetric. In addition, the new constraint of the exclusive existence of *observed* colourless singlet states has to be imposed. If the quarks transform according to SU(3) and the antiquarks with a corre-

sponding representation, the colour singlet states are the colourless baryonic and the mesonic states, which are observed.

When examined in relativistic collisions, QCD often appears to be a theory of free quarks and gluons. At wavelengths of the order of an nucleon, bound particles are observed. These particles are quarks bound (confined), with string like potentials, mediated by the strong gauge boson: the gluon. The QCD physics proves nonetheless itself to be very difficult, if not impossible to solve as of present state. However, QCD is believed to be an ultimatively non-reducible theory, thus being described by the QCD Lagrangian. This presentation of chromo dynamics is brief and only meant to serve as an orientation.

2.3.2 The QCD Lagrangian

The group of chromo dynamics is SU(3). This special unitary group has as elements complex 3×3 matrices. The matrices has determinant $\det(A) = -1$. There are nine different 3×3 matrices and thus eight different coordinates in colour space, which makes the gluons octets. The matrices i.e. the charge operators operates on themselves (gluon - gluon) and on the colour triplet states (quarks).

The standard variational approach starts with the Lagrangian of the theory. The calculation of matrix elements is carried out using the Lagrangian density [84]

$$\mathcal{L} = \mathcal{L}_{Classical} + \mathcal{L}_{Gauge-fix} + \mathcal{L}_{Ghost}, \tag{2.37}$$

with the classical Lagrangian density as

$$\mathcal{L}_{Classical} = \sum_f \left[\bar{q}_a \left(i\not{D} - m\right)_{ab} q_b\right]_f - \frac{1}{4} F^{\alpha}_{\mu\nu} F^{\mu\nu}_{\alpha}, \tag{2.38}$$

where the α run over the colour octet indexes, and a run over colour triplet indexes. The quarks are represented as (fundamental representation)

$$q = \begin{pmatrix} q_R \\ q_G \\ q_B \end{pmatrix}. \tag{2.39}$$

Starting with the gluon field $\mathcal{A}^a_\mu$, the field tensors can be derived as

$$F^{\alpha}_{\mu\nu} = \left[\partial_\mu \mathcal{A}^{\alpha}_{\nu} - \partial_\nu \mathcal{A}^{\alpha}_{\mu} - g_s f^{\alpha\beta\gamma} \mathcal{A}^{\beta} \mathcal{A}^{\gamma}\right], \tag{2.40}$$

where g_s is the strong coupling term, defined as

$$g_s^2 = 4\pi\alpha_s. \tag{2.41}$$

The Gauge fix term is then

$$-\frac{1}{2}(\partial_\mu A^{\mu}_i)^2, \tag{2.42}$$

and the ghost term is

$$\partial_\mu \eta_i \partial^\mu \tilde{\eta}_i. \tag{2.43}$$

The ghost fields η represents fermion with spin-0. The particles are not observable, but considered as virtual particles, however interacting with the gauge fields. The fields are introduce in order to obtain the generating fnuctional more convenient. The gauge fix terms also works in favour of obtaining the generating functional.

The running coupling α_s, is defined (derived below) as

$$\alpha_s(Q^2) = \frac{\alpha_s(\mu^2)}{1 + \alpha_s(\mu^2)(11 - \frac{2}{3}n_f)\ln(\frac{Q^2}{\mu^2})}. \tag{2.44}$$

The covariant derivative, which act on the triplet and the octet field is

$$(D_\mu)_{\alpha\beta} = \partial_\mu \delta_{\alpha\beta} + ig\left(t^\gamma \mathcal{A}^\gamma_\mu\right)_{\alpha\beta}. \tag{2.45}$$

The generators t^α can be written in terms of the 3×3 Gell-Mann matrices $t^\alpha = \frac{1}{2}\lambda^\alpha$. The colour flows during interaction thus producing the final colour singlet states with zero colour charge. Thus, the colour charge is not observed in the final state. This means that the colour is averaged over in the incoming states instead of projected into different colour states (confinement). The interaction always involve a contraction of the Gell-Mann matrices and the quark states. The contractions are referred to as colour factors associated to each QCD process.

2.3.3 Deep Inelastic Scattering

Deep inelastic scattering reveals the deeper structure of e.g. protons. In the parton picture the scattering has a natural interpretation. Some kinematical definitions are made:

$$\begin{aligned} Q^2 &= -q^2 \\ M^2 &= p^2 \\ \nu &= p \cdot q = M\left(E' - E\right) \\ x &= \frac{Q^2}{2\nu}. \end{aligned} \tag{2.46}$$

The structure of the "target" e.g. the proton is examined through the structure functions F_i. The structure functions describes the resolved proton. This digress assumes a lepton-proton interaction.

In the infinite momentum frame, the relevant cross section can be written [85]

$$\frac{d^2\sigma}{dxdQ^2} = \frac{4\pi\alpha^2}{Q^4}\left((1+(1-y)^2)F_1 + \frac{1-y}{x}(F_2 - 2xF_1)\right). \tag{2.47}$$

This model assumes an point like constituents (partons). The structure functions of the complex proton are obtained from the quark structure functions

$$F_2(x) = 2xF_1(x) = \sum_f e_f^2 xq\,(x)\,. \tag{2.48}$$

Assuming e.g. three flavours; up, down strange, we get the structure function

$$F_2 = x\left(\frac{4}{9}(u+\bar{u}) + \frac{1}{9}(d+\bar{d}+s+\bar{s})\right) \tag{2.49}$$

In general, the structure function $F_2(x, Q^2)$, is obtained starting with a bare quark distribution (in a proton)

$$q(x,\mu^2) = q_0 + \frac{\alpha_s}{2\pi}\int_x^1 \frac{d\chi}{\chi} q_0(\chi)\left\{P\left(\frac{x}{\chi}\right)\ln\frac{Q^2}{\kappa^2} + C\left(\frac{x}{\chi}\right)\right\}. \tag{2.50}$$

The function $P\left(\frac{x}{\xi}\right)$ is the splitting function and denotes the probability for the e.g. quark to have a parton, e.g. gluon in a vicinity of it. This probability is evaluated at a logarithmic resolution $t = \ln\left(\frac{Q^2}{\mu^2}\right)$.

The splitting function is calculated in the e.g. DGLAP-framework [86]. Examples of the splitting function could be, e.g. the probability for a gluon to be revealed as a part of a quarks inner structure is

$$P_{gq} = \frac{4}{3z}\left[1+(1-z)^2\right], \tag{2.51}$$

where the gluon has the momentum fraction $z = \frac{x}{y}$ of the "parent" quark. A DGLAP equation can thus be derived using this framework. The additional logarithmic correction can be seen upon as the differential parton distribution, such that [82]

$$\Delta f = -\frac{\alpha_s}{2\pi}\ln\left(\frac{Q_2^2}{Q_1^2}\right)\int_x^1 \frac{dy}{y} f(y) P_{gq}(\frac{x}{y}). \tag{2.52}$$

This leads to

$$\frac{df}{dt} = \frac{\alpha_s}{2\pi}\int_x^1 \frac{dy}{y} f(y,t) P_{gq}. \tag{2.53}$$

As stated this equation is referred to as the Dokshitzer-Gribov-Lipatov-Altarelli-Parisi equation (DGLAP). This type of approximation is only valid

with a sufficiently high Q^2 and x. A large α_s would also degenerate the precision of the DGLAP equation. These digression also serves as a picture of subatomic interactions.

2.4 Hydrodynamics

2.4.1 Introduction

In investigating relativistic heavy ion collisions, the evolving matter distribution, produced by the interacting constituents of the ion collisions need to be described. Making a micro evolution model of the matter distribution might prove unwieldy, including all micro interactions on an individual level is likely adding too much calculation weight to the evolution equations and in the computer code.

The use of relativistic hydrodynamics provides a certain level of abstraction of the micro dynamics, thus using a calculated average in the hydro dynamical calculations. Still, the use of hydrodynamics is justifiable due to its universality, using conservation laws and equation of state only. Additional relations might be added due to dissipative effects.

Evolving the matter evolution with a hydro dynamical, ideal, paradigm was first suggested by Landau using Euler's work [70, 15]. Theoretical refinements has and are carried out to this day [89, 90, 91, 92, 93]. The virtue of the hydrodynamics approach is the way of describing the dynamics by a set of conservation laws and an equation of state. Which is can be used as a first order investigation, thus abstracting the micro interactions.

2.4.2 Initial Conditions

The initial state is formed out of the collisional participants, which interacts and form a frozen GLASMA state. The GLASMA evolves into the a non-equilibrated partonic plasma distribution, where the matter distribution thermalizes in a time frame τ, as a function of the saturation scale Q_S

$$\tau_0 \sim \frac{1}{Q_S}, \quad Q_S^2 = Q_0^2 \frac{T_A}{T_0} (\frac{x_0}{x})^\lambda, \tag{2.54}$$

with the parameters set to; $Q_0^2 = 2$ GeV^2, $T_0 = 1.53$, $x_0 = 0.01$ and $\lambda = 0.28$ [34]. The termalization time will then evaluate as $\tau_0 \approx 0.7$ fm/c.

The point of termalization is then used as initial conditions for the hydro dynamical evolution equations. The initial conditions can be modelled in e.g. Glauber theory [25, 26, 94, 28], as in present thesis, where the initial distribution is derived from geometrical concepts.

In defining the initial condition, an Woods-Saxon distribution is used. The nucleon density is then described by [28]

$$\rho\left(r\right) = \frac{\rho_0 + w(r/R)^2}{1 + e^{(r-R)/d}}. \tag{2.55}$$

In order to get some numerical results, an ALICE parameters are used. Distribution parameters from [95] are used; nuclear cut off radius $R = 6.62$ fm, the nuclear skin depth $d = 0.546$ fm and the parameter $w = 0$. The distribution is normalized according to

$$\int_0^R \rho\left(r\right) dV = A. \tag{2.56}$$

The distribution is integrated with a c++ implementation of the Romberg algorithm. This gives us the $\rho_0 = 0.199$ for lead ions in an ALICE environment. Due to Lorentz contraction, a thickness function is defined. The function is the transverse nucleon density distribution, and is calculated as

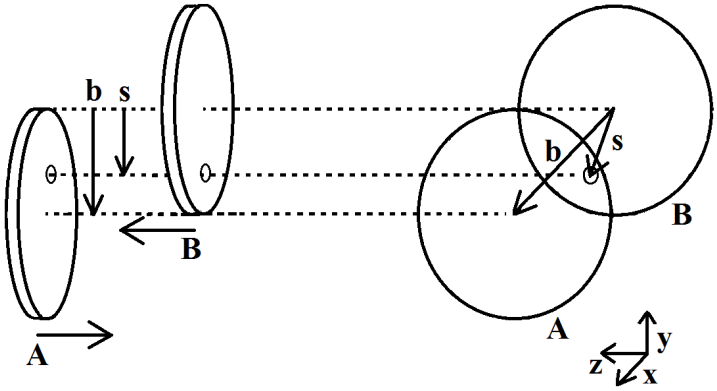

Figure 2.4: Impact vector and mass/density element. Situation for integration. Ion A and ion B approaching each other with impact vector **b** and position vector **s**.

$$T(x, y) = \int_{-\infty}^{\infty} \rho(x, y, z) dz. \tag{2.57}$$

In order to make calculations involving the produced matter and its evolution, the participants in the collision process needs to be quantified (Fig. 2.4). This can be achieved through different methods used on different regimes. The produced particle number can be estimated as being proportional to the number of wounded nucleons in the process. Number density for wounded nucleons are defined as the sum of all nucleons participated in *at least* one reaction [73]

$$
\begin{aligned}
n_{WN} = T_A(x+\frac{b}{2},y)\left[1-\left(1-\frac{\sigma_0 T(x-\frac{b}{2},y)}{B}\right)^B\right] \\
+ T_B(x-\frac{b}{2},y)\left[1-\left(1-\frac{\sigma_0 T(x+\frac{b}{2},y)}{A}\right)^A\right].
\end{aligned}
\tag{2.58}
$$

I.e., the number of participants is

$$
N_{Participants} = \int dx^2 n_{WN}(x,y). \tag{2.59}
$$

The densities are calculated with $b = 5$ for separation and clarity (Fig. 2.5). A Newton-Cotes algorithm is used on a transverse grid in order to calculate the densities. The algorithm is then implemented in c++ and array-run for safety on the Abel Cluster [1]. Run time for each grid is ~ 100 min. In order to calculate eccentricities and to plot the distributions, Root [115] macros are written and run on local LINUX workstations at the Physics Department at the University of Oslo.

The binary collision density is also calculated. This type of density is relevant in a high energy collision. The nucleon (parton) propagates after an initial collision and scatters off other scattering centres in its path through the interaction area. The density is then defined as

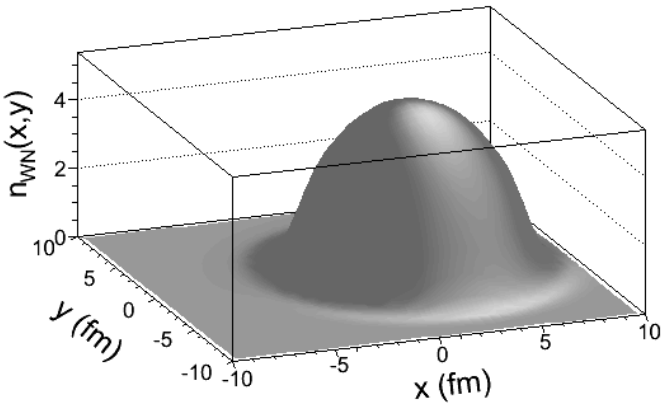

Figure 2.5: Density function for wounded nucleon model. Pb+Pb ion collision with b=5 fm. Collision center at $x = 2.5$ fm.

[1] The Abel Cluster is owned by the University of Oslo and the Norwegian metacenter for High Performance Computing (NOTUR), and operated by the Department for Research Computing at USIT, the University of Oslo IT-department. http://www.hpc.uio.no/

$$n_{BC} = \sigma_0 T_A(x + \frac{b}{2}, y) T_B(x - \frac{b}{2}, y) \tag{2.60}$$

The initial post-collisional transverse energy distribution may be parameterized as a combination of the wounded nucleon density (WN) and the binary collision density (BC)

$$W(x, y, b) = (1 - \alpha) n_{WN}(x, y, b) + \alpha n_{BC}(x, y, b). \tag{2.61}$$

The α parameter denotes the fraction of binary collisions in the process and is fitted to the observed distribution [47]. The resulting eccentricities

$$\epsilon_2 = \frac{\langle y^2 - x^2 \rangle}{\langle y^2 + x^2 \rangle}, \tag{2.62}$$

is then a measure of the second order deformation of the initial participant distribution. Comparing the eccentricities (2.62) and initial conditions with the evolved state of the matter would provide a vast amount of information. Or, hypothesizing the matter evolution and observing the final state matter provides the initial condition. This type of situation demands factorization and alternating hypothesizing in order to move the understanding forward.

2.4.3 Hydrodynamics

Given the initial distribution which has equilibrated after the collisional pseudo evolution, the hydro dynamical equations can be applied on the thermalized initial conditions. The conservation laws for causal hydrodynamics in the given setting are given by [96]

$$\partial_\mu T^{\mu\nu} = 0, \quad \partial_\mu J^\mu_B = 0. \tag{2.63}$$

Here, the $T^{\mu\nu}$-tensor is the divergence free energy momentum tensor and J^μ_B is the conserved baryonic current. The energy momentum tensor and the baryonic current is defined in terms of the time like flow vector u_μ

$$\begin{aligned} T^{\mu\nu}_{Ideal} &= (\epsilon + \mathcal{P}) u^\mu u^\nu - \mathcal{P} g^{\mu\nu} \\ J^\mu_{Ideal} &= \rho_B u^\mu, \end{aligned} \tag{2.64}$$

where the energy density is ϵ and the pressure $\mathcal{P}$ is governed by an equilibrium equation depending on energy and baryon density ρ_B. Using The equations (2.64), we get for the zeroth component

$$\begin{aligned}
\partial_\mu T^{\mu\nu} &= \partial_\mu \Big[(\epsilon + \mathcal{P})\, u^\mu u^\nu - \mathcal{P} g^{\mu\nu} \Big] \\
&= u^\mu u^\nu \partial_\mu \mathcal{P} + u^\mu u^\nu \partial_\mu \epsilon + (\epsilon + \mathcal{P})\, \partial_\mu u^\mu u^\nu + (\epsilon + \mathcal{P}) u^\mu \partial_\mu u^\nu - g^{\mu\nu} \partial_\mu \mathcal{P} \\
&= u^\mu \partial_\mu \mathcal{P} - \frac{d\mathcal{P}}{d\tau} + u^\mu \partial_\mu \epsilon + (\epsilon + \mathcal{P})\, u^\mu \partial_\mu u^0 = 0 \\
&\Leftrightarrow \frac{d\epsilon}{d\tau} = -\frac{\epsilon + \mathcal{P}}{\tau},
\end{aligned} \tag{2.65}$$

with the assumption of an uniform matter distribution [22, 97, 73]. The differential equation (2.65) is trivial and solves with the EOS $\mathcal{P} = v_s^2 \epsilon$ as

$$\begin{aligned}
\frac{d\epsilon}{d\tau} &= -\frac{\epsilon + \mathcal{P}}{\tau} \\
\int \frac{d\epsilon}{\epsilon + \mathcal{P}} &= -\int \frac{d\tau}{\tau} \\
\int \frac{d\epsilon}{\epsilon + v_s^2 \epsilon} &= -\int \frac{d\tau}{\tau} \\
\int \frac{d\epsilon}{\epsilon + v_s^2 \epsilon} &= -\int \frac{d\tau}{\tau} \\
\frac{\ln(\epsilon)}{1 + v_s^2} &= -\ln \tau + \ln C \\
\epsilon &= \epsilon_0 \left(\frac{\tau_0}{\tau} \right)^{1 + v_s^2}.
\end{aligned} \tag{2.66}$$

The temperature dependence can thus be transformed, through the appropriate EOS into other thermo dynamical properties e.g. temperature, which the evolves according to (2.66).

The matter distribution is evolved under the governing hydro dynamical equations along with equation of state (Fig. 2.6). The initial condition for the equations is the thermalized matter distribution achieved shortly after the time of impact. When thermalized, the matter evolves in a hydro dynamically.

The driving force of the matter dynamics is pressure. Current conservation (2.63) suggests, with Navier-Stokes evolution

$$\begin{aligned}
u^\mu \partial_\mu \rho + \rho \partial_\mu u^\mu &= 0 \\
\frac{\partial (u^0 \rho)}{\partial t} &= v \cdot \nabla \rho + \rho \nabla \cdot v.
\end{aligned} \tag{2.67}$$

Assuming a rectilinear matter velocity, the density in the transverse plane diminishes fastest for a velocity parallel with the density gradient (2.67). I.e. the gradient of the pressure is greatest parallel to the transverse reaction

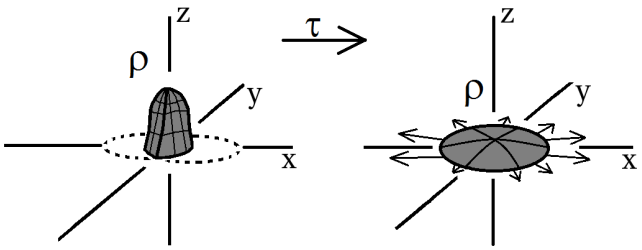

Figure 2.6: Initial conditions. The initial conditions are schematically displayed. The evolved matter prior to freeze-out on the left side. The matter distribution equalizes in spatial space due to larger pressure gradient in "x-direction" thus building up in momentum anisotropy.

plane axis, due to initial geometry, this will make the pressure equalize fastest. i.e. building up the most flow in transverse momentum space, parallel to the pressure gradient.

The fluid may be assumed ideal, i.e. assumed to have zero viscosity. The equations can, and is in practice modified in order to account for the non-zero viscosity [98, 17, 92, 99, 100, 101]. The stress-strain tensor is then put in the form

$$T_{\mu\nu} = T^{ideal}_{\mu\nu} + \Pi_{\mu\nu}. \tag{2.68}$$

The ideal part of the tensor $T_{\mu\nu}$ is the same used in the derivation above. The specifics of the viscous term can be parameterized in different ways [17]. Here, the viscous term in (2.69) can be taken as the first order Navier-Stokes term in local rest frame

$$\Pi^{\alpha\beta} = \eta \left(\partial^\alpha u^\beta + \partial^\beta u^\alpha - \frac{2}{3} g^{\alpha\beta} \partial_\mu u^\mu \right). \tag{2.69}$$

The dissipative term (2.69), has two main terms. The first term is dependent on the velocity gradient, i.e. "classical shear". This term is dependent on the radiative loss of the matter.

The second term is a source term, which is bounded by the microscopic relaxation time for the fluid [102], where zero relaxation time corresponds to zero viscosity. The relaxation time might be taken as

$$\tau_\pi = \frac{\eta}{Ts}, \tag{2.70}$$

where the temperature is denoted T and the entropy density s.

The matter evolves and equilibrates differentially depending on the viscosity. Due to friction, the spatially differentiated *flow* equilibrates in opposition to the force of *matter*. Although anisotropic flow producing, the flow is suppressed due to viscosity.

The viscosity debated is usually in the context of anisotropic flow, shear viscosity. Also, there is bulk viscosity, not affecting anisotropy in the same quantitative way. Thus, the shear viscosity diminishes not only the initial ellipticity, but also the more local fluctuations which will affect the higher harmonics to a larger extent due to their fluctuative characteristics, e.g. triangular flow.

2.5 The HYDJET++ Model

2.5.1 Introduction

The HYDJET++ package includes two main parts. First, the soft part, which is a parameterized model, thus generating soft states on the chemical and thermal freeze-out surfaces [69]. The generation of soft particles includes *materia* effects, such as flow modulations and decays. This part is derived from the FAST MC model [110, 111].

2.5.2 Parton Picture

All physical interactions depends on the energy transferred in the process. The energy transferred sets the scale of the scattering. If more momentum is transferred in the process, then the scattering resolution increases. The resolution of the incoming boson is $\sqrt{Q^2}$, i.e. the boson resolves only partons [81, 96, 83] with transverse momentum less, or an wave length longer than the incoming boson. The proton viewed in its rest frame is composed of three valence quarks confined in a colour singlet state. The "proton ether" is also fluctuating thus producing parton-antiparton pairs, with an ephemeral nature. These partons has a virtual nature and has the scale of Λ_{QCD}. The nature of the fluctuations are frame dependent since the lifetime of the fluctuations are boost dependent

$$\Delta t = \gamma \Delta t_0. \tag{2.71}$$

Since the lifetime of the fluctuations are much longer than the mean free path of the partons, the partons can be considered as free particles within in the e.g. proton. The partonic cross section can thus be factorized as e.g.

$$d\sigma = \sum_i x_i f_i(x, \mu^2) d\hat{\sigma}_i, \tag{2.72}$$

where $\hat{\sigma}$ is the cross section for the partonic event.

2.5.3 Hard Scattering

The hard part of the code generates multiparton rescattering and parton radiation. These parts are a superposition, intermixing continuously. The code at present might be constrained for symmetric heavy ion collisions ($40 \leq A$), and energies 10 GeV $\leq \sqrt{s}$. The centrality generation might also be seen as constrained to the range $0 - 50\%$ due to model specific parameterization. Forward rapidties are not seen to be completely described in present model.

A model for the jet production in the media is e^+e^- annihilation. The annihilation is followed by a quark-antiquark production originating from the emitted boson. The virtuality is usually high for the quark pair due to the large momentum transfer. The quark pair will thus cascade down under gluon emission. These gluons cascades down further under gluon emission thus losing virtuality while branching, however to a finite extent until the cascading approach mass shell. During cascading, the momentum transfer and virtuality diminishes. This will lead to a larger coupling constant and a virtuality $\sim 1GeV$. The jet is triggered and thus produces a cone of distributed and correlated particles. In a heavy ion collision setting, the jets are produced asymmetrically in the matter distribution. This asymmetry will translate into an particle/energy asymmetry. This asymmetry may lead to a complete or partial loss of one or several members of the annihilation/jet diagram. A consequence of this process is the observed "jet quenching".

The *in materia* energy loss is modelled including the Landau-Pomeranchuk-Migdal effect for QCD, with the use of the modified emission spectra for the expanding medium. The generic expression for the energy loss, ΔE of a parton traversing the media is

$$\delta E = \int_0^L dl \exp(-l/\lambda(l)) \frac{dE}{dl}, \tag{2.73}$$

where the exponential denotes the probability for scattering due to the media. Here, the "L" denotes the dimension of the media traversed. The media properties are included in the mean free path $\lambda = \frac{1}{\rho\sigma}$, and is defined by the matter density ρ, and the scattering cross section σ. The energy loss is then divided in two main parts. The energy loss for a parton with mass m_p and energy E off thermal partons ($m \sim 3T << E$), due to the collisional part is in this model treated in the high momentum limit [125, 126, 127].

$$\frac{dE^{coll}}{dl} = \frac{1}{4T\lambda\sigma} \int_{\mu_D^2}^{t_{max}} dttC \frac{2\pi\alpha^2(t)}{t^2} \frac{E^2}{E^2 - m_p^2}, \tag{2.74}$$

with the α denoting the strong running coupling constant, and the momentum transfer is t, and T denotes the temperature. The Debye mass μ_D, is here taken as the minimum momentum transfer and the constant C is due to the scattering species (gg, gq and qq). This regularization makes the low

momentum scatter being cut off. The momentum is however low, thus not contributing to the energy loss (2.74) to a greater extent. to The scaling parameter is in level with the temperature for the quark hadron transition $\Lambda \sim 200$ MeV.

The other mode of energy loss is the radiative loss. The energy loss is here modelled in the BDMS framework [105, 106, 107, 108, 109]. The energy loss spectrum is thus modelled as

$$\frac{dE^{rad}}{dld\omega} = \frac{2\alpha C_R}{\pi L}[1 - y + \frac{y^2}{2}] \times \ln|\cos\left(\sqrt{i(1 - y + C_R\frac{y^2}{3})\frac{\mu_D^2\lambda_g}{\omega(1-y)}\ln\left(\frac{16\omega(1-y)}{\mu_D^2\lambda_g}\right)}\frac{L}{2\lambda_g}\right)|. \tag{2.75}$$

The spectrum is integrated from the minimum energy $E_{min} = \mu_D^2\lambda$ over all relevant energies. The fractional energy radiated is thus denoted $y = \omega/E$, and the Casimir factors are C_R.

The radiated gluons are modelled in the small angle parameterization

$$\frac{dN^g}{d\Theta} \propto \sin\Theta \exp\left(-\frac{(\Theta - \Theta_0)^2}{2\Theta_0^2}\right), \tag{2.76}$$

with Θ_0 approximated to five degrees. As of choice in the input file, there are a wide angle distribution ($\frac{dN^g}{d\Theta} \propto \frac{1}{\Theta}$), and a collinear choice ($\frac{dN^g}{d\Theta} = \delta(\Theta)$).

The interacting, expanding matter is modelled, or parameterized by the scaling solutions [22]

$$\epsilon\tau^{4/3} = \epsilon_0\tau_0^{4/3} \tag{2.77}$$

$$T\tau^{1/3} = T_0\tau_0^{1/3} \tag{2.78}$$

$$\rho\tau = \rho_0\tau_0. \tag{2.79}$$

Here, the index naught denotes the proper time of quantum gluon plasma, and the thermodynamic state. The scaling then gives the state at arbitrary proper time. The initial energy density is calculated as the scaled central hit energy density. The initial energy is then scaled with the fractional density and the fractional transverse nuclear overlapping area. The density function T_{AA} is then the standard density overlap in standard Glauber theory. The input temperature parameter then interpreted as $T_0 \propto \epsilon_0^{1/4}$.

2.5.4 Freeze Out

The thermal state generated on the freeze out hyper surfaces is thus generated out of the parameter list (Fig. **??**). The hydrodynamic evolution

is abruptly ended at freeze out, with given parameterized conditions and chemical potentials for baryons, strangeness and pions for tuning.

The momentum distribution is thus given by a thermal distribution in the fluid rest frame [110, 111]

$$f_i^{eq}\left(p^0, T^{ch}, \mu_i, \gamma_i\right) = \frac{g_i}{\gamma_s^{-n_i^s} \exp([p^0 - \mu_i]/T^{ch}) \pm 1}, \tag{2.80}$$

where the strangeness suppression factor γ is powered by the number of strange quarks. The "g" denotes the spin degeneracy and the specie potential is μ_i. The chemical freeze out temperature is denoted by T^{ch} and the plus or minus depends on whether the particle is a fermions or boson. The particle density are then calculated as

$$\rho_i(x) = \int \frac{d^3\mathbf{p}}{p^0} p_\mu u^\mu f_i(x,p). \tag{2.81}$$

The effective volume associated with this density is then for constant emission time τ

$$V_{eff} = \int d^3\sigma_\mu(x) u^\mu(x) = \tau \int d_T^x n_\mu u^\mu \int f(\eta) d\eta, \tag{2.82}$$

where $f(\eta)$ is the flow rapidity distribution and thus is the rapidity denoted by η. The probability density for production of N particles are then given by the Poisson distribution

$$P(N_i) = \exp(-\bar{N}_i) \frac{\bar{N}_i^{N_i}}{N_i!} \tag{2.83}$$

The freeze out temperature is then parameterized as [112]

$$T(\mu_B) = a - b\mu_B^2 - c\mu_B^4, \quad \mu_B = \frac{d}{1 + \sqrt{s}}, \tag{2.84}$$

where the chemical potential is weighted by its charge. The particles cannot be considered as free streaming after chemical freeze out. This calls for a thermal freeze out surface cooler than the chemical freeze out surface [104]. In the HYDJET++ model, this thermal freeze out is implemented.

2.5.5 Decays

The resonances are allowed to decay under cooling and expansion. A reasoning of particle fraction conserving is the used in order to establish the final composition. In use for this process is the input parameter of effective pion potential.

The thermal distribution consists of stable particles and resonances from the SHARE data table [113]. The decay widths are used in simulating the decays with a probability density of

$$\Gamma \exp(-\Gamma\tau). \tag{2.85}$$

The decay is then translated as

$$\Delta L = \Delta\tau P/M, \tag{2.86}$$

where the decaying mass and four momentum is given by M and P. The branching of the decays are also part of the model and is from the same tables [113]. The mass distributions is then of Breit-Wigner type.

2.5.6 Confinement

In connection to the decays is confinement of hadronic states. The non observability of colour, or the invariance of colour in physical observables might be viewed as a exact symmetry. That is, the colour SU(3) is an exact symmetry and only colour singlet states are observed [83]. Quark confinement is referring to the potential, which rises with separation initially, and due to string/flux tube fragmentation, or breaking, reaches a constant value (mass screening) [87]. The flux tube formed at intermediate distances and energy levels makes it more energetically favourable for the string to break into smaller strings, thus producing a quark-antiquark pair, which "preserves" confinement [88]. The strength of the gluon field is assumed to be enhanced due to secondary radiation of gluons by gluons, thus enhancing the field to the realistic confining levels.

2.5.7 Jets

Final state partons and hadrons appear in collimated bunches for hard interactions. The collimated bunches are commonly referred to as "jets". In order to observe jets, one uses a jet definition. The definition specifies how to assign hadron to jets. I.e. kinematics ranges for e.g. partons to belong to one jet instead of another or maybe even form a jet of its own. The jet algorithms are designed for the specific type of setting. Usually the algorithms are of iterative nature and thus start with an initial jet particle as reference and iterates over the assumed jet cone thus finding a distribution which will lead to the next seed particle associated with the obtained distribution. The hard scattering is modelled in the sub part PYQUEN from a generated jet event obtained from PYTHIA [114]. The generation of hard scattering in PYQUEN includes the generation of the initial parton spectra and vertex. The rescatterings are also simulated in the media with the described losses. The final hadronization is then modelled using the Lund string model for

harder partons and emitted gluons. In the presence of shadowing, the mean number of jets is modulated as

$$N_{AA}^{jet} \int dp_T^2 dy \frac{d\sigma_{NN}^{hard}}{dp_T^2 dy} \int d^2x_T T_A(x_1) T_A(x_2) S(x_1, x_2, p_T, y), \tag{2.87}$$

where $S < 1$ denotes shadowing, which factorizes for both colliding nuclei. The shadowing effect is due to the degree of coherence between the target and the projectile and will lower the total number cross section by lowering the *in materia* cross sections. Without shadowing (screening effects), the mean number of jets are proportional to the mean number of binary sub collisions. In the model, the choice of shadowing is an input variable in the parameter file.

2.5.8 The Running Coupling Constant

The running coupling constant is here derived for completeness. The parameter "t" is introduced as

$$t = \ln\left(\frac{Q^2}{\mu^2}\right). \tag{2.88}$$

The running coupling is defined as

$$t = \int_{\alpha_s(\mu^2)}^{\alpha_s(Q^2)} \frac{dx}{\beta\left(x\right)}. \tag{2.89}$$

We use this to derive

$$\begin{aligned} \frac{\partial t}{\partial Q^2} &= \frac{\partial t}{\partial x}\frac{\partial x}{\partial \alpha_s}\frac{\partial \alpha_s}{\partial Q^2} \\ \Rightarrow \frac{\mu^2}{Q^2} &= \frac{1}{\beta(\alpha_s)}\frac{\partial \alpha_s}{\partial Q^2} \end{aligned}. \tag{2.90}$$

Letting $\mu^2 = 1$, the chromo dynamic running coupling is determined through solving the renormalization group equation

$$Q^2 \frac{\partial \alpha_s}{\partial Q^2} = \beta\left(\alpha_s\right). \tag{2.91}$$

Using the expansion for the β function

$$\beta\left(\alpha_s\right) = -b\alpha_s^2\left(1 + b'\alpha_s + b''\alpha_s^2 + \mathcal{O}(\alpha^3)\right) \tag{2.92}$$

and truncate after the first term, we get (2.91)

$$\begin{aligned} Q^2\frac{\partial\alpha_s}{\partial Q^2} &= -b\alpha_s^2 \\ \frac{\partial\alpha_s}{\alpha_s^2} &= -b\frac{\partial Q^2}{Q^2} \\ -\frac{1}{\alpha_s} &= -b\ln(Q^2)+C \\ \alpha_s(Q^2) &= \frac{1}{b\ln(Q^2)-C}. \end{aligned} \tag{2.93}$$

With the condition $\alpha_s(\mu^2)$, we get

$$C = b\left(\ln(Q^2)-t\right)-\frac{1}{\alpha_s(\mu^2)}, \tag{2.94}$$

giving

$$\alpha_s(Q^2) = \frac{\alpha_s(\mu^2)}{1+\alpha_s(\mu^2)b\ln(\frac{Q^2}{\mu^2})}, \tag{2.95}$$

with $b = 11-\frac{2}{3}n_f$. Then the running coupling reads in its final form

$$\alpha_s(Q^2) = \frac{\alpha_s(\mu^2)}{1+\alpha_s(\mu^2)(11-\frac{2}{3}n_f)\ln(\frac{Q^2}{\mu^2})}. \tag{2.96}$$

2.6 Summary

A brief review of some of the theory needed in this thesis is given. The flow analysis needed together with a brief review of the simulation model is included.

The observed distribution in momentum space is derived as a factorization of the transverse momentum spectrum, and the Fourier expansion of the angular distribution. The anisotropy of the observed particle distribution is observed in terms of flow. The flow is further interpreted as the coefficients (cosines) of the Fourier expansion above (2.1).

The lower order flows, i.e. elliptic, triangular and pentagonal flow are tuned and simulated for transverse momentum and centralities. These flows are the building blocks for higher order flows, thus being terms in the expansion of higher order flows in combinatoric terms. The higher order harmonic terms are then put in a form, which is intended for the investigation of factorization. Correlators corresponding to the factorization of the higher order harmonics are derived. Also, the eccentricity fluctuations are touched briefly.

The review also contains a display of fundamental strong dynamics. The foundations of Quantum Chromo dynamics are reviewed, with the phenomena of deep inelastic scattering as an interaction model.

Relativistic hydrodynamics is included with the generation of initial conditions. In present paper, the Glauber theory is almost exclusively reviewed, due to the use of Glauber theory in the model.

Finally, the simulation model in use in present thesis is reviewed. The models for generating the particle distribution is referred to, and the *in materia* modulation of the hadron spectra is reviewed. The spectra for radiative and collisional energy loss is reviewed together with the generation model for scattering decays. The freeze out model is also reviewed, thus concluding the theory section.

Chapter 3

Method

3.1 Introduction

The investigation of matter and its constitution and origin is the core of modern physics. The deep structure probed, where fundamental processes is starting to manifest themselves, is getting accessible through the use of modern detector equipment combined with state of the art particle accelerators and also through cosmological observation. The main particle detectors are situated in the United States of America, at Brookhaven National Laboratory on Long Island, and at LHC in Genève. At Brookhaven, there are four experiments: BRAHMS, STAR, PHENIX and PHOBOS. The energy available is lower at the Relativistic Heavy Ion Collider (RHIC). For Gold+Gold collision the RHIC energy is $\sqrt{s} = 200$ GeV and the corresponding energy for the Pb+Pb ions at LHC is $\sqrt{s} = 2.76$ TeV. The main LHC experiments referred to in this thesis are: ATLAS, ALICE and CMS. The higher level of sophistication and also the higher available energy and mass makes for use of data and parameters from the LHC experiments exclusively. The data from RHIC might serve as reference, but the simulations are exclusively aimed at the investigation of LHC phenomena.

3.2 Problem Statement

In designing experiments, theoretical work and simulations have to precede the construction, or implementation of the experiments. Modern science is characterized by deep structure, i.e. small distances and separation. The conditions necessary to probe matter and its evolution are bound to be extreme. Analogies to the early stages of the Universe have been made with respect to the conditions and the matter evolution from the deconfined hot, pre hadronic state, to the observable hadrons of the present. The interest in investigation of the early stages of the cosmological evolution and the specific stages of matter and formation of observable matter is the highest.

In the laboratory, the hypothesized thermodynamic conditions are achieved through e.g. ion-ion collisions at ultra relativistic velocities, which creates a distribution of participant matter at ultra high temperatures and densities. This matter is assumed to go through several phases when interacting, heating up, and cooling to chemical and thermal freeze out. This evolution includes an array of phenomena related to hadronic formation and deep structure, thus of highest importance. The direct observables available at the detector are the spatial position and the particle momentum. Also, the detector has some additional features, which aid in determining the particles, e.g. calorimetry and luminosity. The investigation of the phenomena in the heavy ion collisions builds upon the particle spectra. The particle spectra is usually split into a transverse momentum spectra and an anisotropic angular distribution [11, 12]

$$E\frac{d^3N}{dp^3} = \frac{d^3N}{p_T dp_T dy d\phi} = \frac{1}{2\pi}\frac{d^2N}{p_t dp_t dy}\left(1 + \sum_{n=1}^{\infty} 2v_n(p_T, y)\cos[n(\phi - \Psi_r)]\right). \tag{3.1}$$

In order to understand the phenomena related to heavy ion collisions, the transverse momentum spectra and the azimuthal anisotropy has to be reproduced in simulations. The reproduction of the particles involves evolution of particle initial states. This type of calculations usually implies extremely heavy calculation done on clustered computers. The computational time may be of the order of hours or days per node. Thus the simulations of the particle spectra and the azimuthal distribution have to be done in a rational way. The distributions obtained in simulations also have to reproduce substructure, i.e. the production modes and the features of them is seen as a priority. When establishing the fundamental distributions, including substructure, further investigations can be made. The higher order harmonics are of interest due to the higher wave number and their response to e.g. jets. Analogies are made to different particle correlators, connected to the higher harmonics (Chap. 2). These higher order harmonics are contextualized as terms of flow expansions, thus being higher flow terms simulated in lower event planes.

3.3 Research Objective

In this Thesis, the simulation of azimuthal anisotropy and transverse momentum spectra are treated in connection with the investigation of strong interactions. Through the azimuthal anisotropy, phenomena related to hadrogenesis are studied, such as confinement and decays. The observed particle distribution is simulated and the transverse momentum spectra and azimuthal anisotropy are extracted from the simulated distribution. The simulations are made on a local computing cluster (ABEL), using a statis-

tical simulation methodology.

The simulations of the elliptic and triangular flow are a prime objective of this thesis. The simulation of the two flows includes establishing the corresponding event planes, which are intended to be used in the simulation of higher order compound flows. Given the reproduction of elliptic and triangular flow for inclusive and for identified particles, the model is assumed to deliver the correct projections in terms of particle production modes. The modes of particle production is then used in order to establish an hypothesis regarding the observability of deeper processes connected to hadronization.

The azimuthal anisotropy of fifth and sixth order are then simulated in the established lower order event planes, i.e. the second, third and fifth. These higher order flows are then compared to the assumed factorizations associated with the lower order event planes. The possibility to observe deeper processes are evaluated with the aid of the simulation model.

3.4 Methodological Framework

3.4.1 Major Research Question

In order to investigate the deeper structure of matter, the hadron genesis has to be studied in relativistic heavy ion collisions. The heavy ion collision participants form a prehadronic matter distribution, which evolves and undergoes several hypothesized phase transitions on its path to hadronization. The matter will freeze out chemically and later thermally. After the thermal freeze out, the particles are assumed free streaming travelling the distance from the event vertex to the interacting detector. The major research question is regarding the possibility of the experimentally observed distributions being reproduced with all its characteristics in order to understand the path "travelled" through different phases starting with the produced initial conditions.

The main question of this thesis is whether it is possible to reproduce the anisotropic flow of second and third order for centralities and also the transverse momentum. Also, connected is the objective of simulating the transverse momentum spectra for unidentified particles. Fulfilment of these objectives is hypothesized to provide a foundation of further analysis work made in order to investigate hadronization. Given fulfilment of these objectives, the simulation of higher order planes are assumed to reveal exclusive properties.

3.4.2 Minor Research Question

The secondary question is whether the elliptic flow is possible to simulate for mesons and baryons. This would occur in parallel with the simulation of the transverse particle spectra for identified particles. Succeeding in this, the

mesonic and baryonic flow may be related in order to reveal deeper hadronic structure and modes of formation.

3.4.3 Hypotheses

The anisotropic flow is possible to simulate to some extent. The elliptic, triangular and pentagonal flow is in specific possible to simulate out of the same statistical set of generated particles. Given this hypothesis, the modes for hadron genesis are possible to simulate and extract. The anisotropic flow is then in connection hypothesized reproducible for identified particles along with particle transverse momentum spectra. Given this, the features of anisotropic flow are possible to investigate and predict for centralities and transverse momentum.

Given this, the simulation of different higher order compound flows are possible. The parts of interest are combinatoric terms which are reachable within present model and are contextualized as terms in the flow expansion of the pentagonal and hexagonal flows. Analogies between these higher order terms and multiparticle correlators can be made. The level of factorization of the higher order flows is to some extent characterizing the level of this analogy. Given the inability to reproduce the higher order flows, there are two main possibilities:
The model fails an extrapolation due to computational truncations or due to coarseness of the present model, e.g. initial conditions.
The analysis work is too symbolic and/or lacks finer details.

3.4.4 Dependent variables

The dependent variable is the particle distribution. The particle distribution may be put in a factorized form which has two main parts: An invariant part depending on transverse momentum and rapidity, and an angular part, dependent on the azimuth of the particle. These are the real output variables.

3.4.5 Independent variables

The independent variables are: the thermodynamic state, including the chemical freeze out temperature, which allows for mainly fluctuations when increased and slightly sustained flow due the hotter plasma. The lowering of the chemical freeze out temperature will make the phase space denser, thus lower the flow (lesser degree of disassociated partons).

A lower temperature makes the phase space denser, thus less fluctuating. The thermal freeze out temperature is giving the distribution its slope $-\frac{1}{T}$, thus making the phase space denser and lower the azimuthal anisotropy due to a higher degree of thermal scattering.

Also independent are the effective chemical potentials, which control particle production and thus the azimuthal anisotropy, e.g. a high chemical potential makes the flow focus around the transverse plane, thus elevating the anisotropic flow.

The total mass and its distribution is also of importance for the development of flow and the produced yield. The larger amount of matter leads to a larger participant matter distribution, thus higher levels of energy loss. The flow is highly dependent on pressure gradients in the initial matter distribution, in order to generate the matter constituent velocities.

Further, geometric properties such as the impact vector b, which is another term for centrality, governs the ellipticity and amount of participant matter. The elliptic flow has a rising but limiting behaviour due to the impact vector.

The matter radius is also of importance for the hydro dynamical flow. Increasing the matter radius will make the matter distribution larger thus less fluctuating. This is equivalent to a longer (in transverse momentum) hydro phase, however lower flow due to less eccentricity (pressure gradient).

The energy available per nucleon is also an independent variable. The energy makes for hotter plasma, thus more hydro like flow, hence higher degree of flow for lower centralities and LHC displays lower elliptic flow for higher centralities due to higher jet production which manifests itself in the R_{AA} observable.

3.4.6 Moderating variables

The choice of media cross sections might be seen upon as moderating. The in-media cross sections will have a quantitative influence on the produced distributions. The different flow modes of the distribution are qualitative moderations of the simulations.

3.4.7 Assumptions

In this thesis, in addition to the model assumption, the assumption of the hierarchical flows are made. I.e. a lower order eccentricity is more defining for the evolution of the produced matter than a higher order eccentricity. This makes for the assumption of a second and third order event plane main dependence in all other flows. Of course, in the detector, planes of all orders are present. This assumption might lead to deviations in the simulated distributions.

3.4.8 Limitations

The limitations of this work is in some sense investigated. The tuning of the model main flows is used for the higher order work. This assumption might

be visible in higher order terms. Here, the deviation should then be proportional to the order of factorization of e.g. flow. This is in a sense the core of the simulation programme: A model is used and proved and extrapolated in order to make predictions. The predictions are considered and modifications are made. The model is reconsidered and maybe progress is made. An obvious limitation with present model is the transverse momentum range where the flow is reproduced with enough accuracy to make higher order predictions. This is mainly due to the fact that reliable spectra is lacking due to fluctuations and low multiplicity, which will make the model tuning difficult at best.

The corresponding limitation is also in the generation of (model) eccentricity. In this model, the eccentricity distribution proves hard to simulate, or fit to the precision needed. Higher centrality is wished for, but is not likely to be reproduced with present model due to the steep parameterization, which makes fitting very difficult. The generation of initial conditions are also a limitation, since realistic generation of initial conditions are not implemented. This makes the model event planes hard to simulate in a realistic way. The higher order flows then gets harder to reproduce in their own event planes, due to the fluctuating nature of the flows.

3.5 Research Design

The simulation of heavy ion collisions is in present paper made using the a Monte Carlo based simulation package. Given the process evolutionary characteristic, the need for cluster computing quickly become obvious. The heavy ion simulation package of the associated research group is HYDJET++ [69], which is the simulation tool in use in this thesis. This simulation package uses a combination of parameterized hydrodynamics combined with generated hard processes and decay algorithms and the physics model is described in chapter 2.

In the model, the matter radius is modelled in terms of the azimuth and the mean squared radius $\bar{R}$ as

$$R\left(b,\phi\right)=\bar{R}(b)\frac{\sqrt{1-\epsilon^{2}(b)}}{\sqrt{1+\epsilon(b)\cos\left(2\phi\right)}}, \tag{3.2}$$

where the momentum ($\delta(b)$) and spatial ($\epsilon(b)$) anisotropy parameters are defined as

$$\begin{aligned} \epsilon_0(b) &= \frac{b}{2R_A} \\ \epsilon(b) &= k\epsilon_0 \\ \delta &= \frac{\sqrt{1+4B(\epsilon(b)+B)}-1}{2B} \\ B &= C(1-\epsilon^2(b))\epsilon(b), \end{aligned} \tag{3.3}$$

where R_A is the ion radius. The transverse rapidity profile is then scaled with the fractional radius as

$$\rho = \frac{r}{\bar{R}}\rho^{max}(b=0), \tag{3.4}$$

where the transverse velocities are

$$u_1 = \sqrt{1+\delta(b)}\sinh(\rho)\cos(\phi) \tag{3.5}$$

$$u_2 = \sqrt{1-\delta(b)}\sinh(\rho)\sin(\phi). \tag{3.6}$$

The effective volume, mean square radius and temperature are scaled for centralities in terms of the effective volume and the mean number of particles

$$V_{eff}(b) = V_{eff}(0)\frac{\bar{N}(b)}{\bar{N}(0)} \tag{3.7}$$

$$\bar{R}\,(b) = \bar{R}\,(0)\sqrt{\frac{V_{eff}(\delta(0))}{V_{eff}(\delta(b))}} \times \left(\frac{\bar{N}(b)}{\bar{N}(0)}\right)^{1/3} \tag{3.8}$$

$$\tau(b) = \tau(0)\left(\frac{\bar{N}(b)}{\bar{N}(0)}\right)^{1/3}. \tag{3.9}$$

The rapidity is modulated in terms of the event planes, e.g. the parameterization might look like

```
Double_t rhou3 = 0.0645*TMath::Sqrt((0.5*impactParameter)/0.67);
Double_t rhou4 = 0.0235*((0.5*impactParameter)/0.67);.
```

The rapidity is then simulated as e.g.

```
rhou = rhou*(1+rrcoeff*rhou3TMath::Cos(3*(phiF+psiforv3))
       +rrcoeff*rhou4*TMath::Cos(4*phiF));.
```

The simulation code is prepared with respect to the observables simulated. Some of the code needs to be modified substantially, or put in.

Parameterizations are also in some cases needed to fit against data and establish theoretically. E.g., the parameterization for the model ellipticity is modified in order to soften the more dilute end of the impact parameter spectra. Modifications for the fireball radius are also likely necessary in order to reproduce the azimuthal anisotropy. This seems to be two of the key factors for reproducing flow with a high degree of prediction.

The fits are straightforward uniformly weighted least square fits and are implemented in c++ and run on the local Abel cluster [1]. The fits along with the modifications needed in order to produce the data containers (histogram) are implemented and compiled and test run on local computers. The modifications are mostly done by adding container generating code pieces to existing code and also adding physical parameters for the simulation.

The event simulation is done with the PYTHIA [114], thus calculating the inelastic cross sections, including the hard cross sections. The impact parameter distribution is generated in the framework of the multiple scattering Glauber model [26], thus the inelastic cross section is simulated as

$$\frac{d^2\sigma^{AA}}{d^b} = 1 - \left(1 - \frac{T_{AA}\sigma_{NN}(\sqrt{s})}{A^2}\right)^{A^2}. \tag{3.10}$$

The binary and participant mean yields are then calculated as

$$\bar{N}_{binary} = T_{AA}(b)\sigma_N N(\sqrt{s}) \tag{3.11}$$

$$\bar{N}_{participant} = \int d^2x_T T_A(r_1)(1 - \exp(\sigma_{NN}(\sqrt{s})T_A(r_2))) \tag{3.12}$$

The soft and hard particles are generated independently and superposed in the output file, i.e. RunOutputHisto.root.

The hard state is simulated by random generation of the fraction weighted jet cross section. Hard sub collisions are simulated for proton-proton, or neutron-neutron collisions. The transverse jet vertex density is then calculated as

$$\frac{dN^{jet}}{dx_T}(b) = \frac{T_A(r_1)T_A(r_2)}{T_{AA}(b)}. \tag{3.13}$$

The energy loss for hard partons traversing the matter, the multiple scattering energy loss is iterated according to the theory in chapter 2. The energy and momentum is thus modulated per scattering for radiative and collisional loss. The scattering criteria is then the spatial (thermal), which is fulfilled as long as the temperature is above T_c and the "quenched" criteria,

[1] The Abel Cluster is owned by the University of Oslo and the Norwegian metacenter for High Performance Computing (NOTUR), and operated by the Department for Research Computing at USIT, the University of Oslo IT-department. http://www.hpc.uio.no/

which means that the scattered partons momentum reaches the surroundings, thus dissipating into the media ($p_T \leq 2T$). Shadowing and decays are also implemented according to the theory section (chap. 2).

The soft particles are simulated by initializing the chemical and thermal freeze out parameters. The geometric properties along with the freeze out time and time of emission is also calculated. The multiplicity is then calculated according to theory chapter. The particle properties are simulated according to e.g. (3.5).

The two and three body decays are run, with randomized decay channel [110, 111]. For the two body decay, the momentum and spatial orientation is given by

$$|p| = \frac{1}{2}\frac{\sqrt{(M^2 - m_1^2 - m_2^2)^2 - 4m_1^2 m_2^2}}{M} \tag{3.14}$$

$$\cos(\Theta) \in [-1, 1], \quad \phi \in [0, 2\pi]. \tag{3.15}$$

The three body decays are simulated with a random distribution of the energies

$$\begin{aligned} E_1 &= \xi_1 \Delta M \\ E_2 &= (1 - \xi_2)\Delta M \\ E_3 &= (\xi_2 - \xi_1)\Delta M, \end{aligned} \tag{3.16}$$

where the ξ are random numbers, uniformly distributed. The first decay remnant is randomly oriented. The last two decay remnants are randomized using conservation laws. The remnants are then boosted to the collision rest frame. Coordinates for the decay remnants are the same as for the parent resonance.

The HYDJET++ is implemented in c++ and ROOT [115]. A Fortran part is also included in the generator structure. The main user parts of the package is the particle and decay files with descriptions of particles and the decay branches as in Fig. 3.1. The main input file is RunInputHydjet, in which the user input parameters are written prior to simulation run. The main user part, where particles are distributed into user specified containers, is the RunHadronSource-file. Here, the user receives the particle distribution and may construct the observables required. The containers are usually produced in various ROOT objects, such as e.g. TProfile histogram.

The whole simulation package is then uploaded on the Abel cluster along with the macros needed in order to array run the MC code for statistics. The statistics needed is in the order of $\sim 1,000,000$ simulated collision events. This number varies over several orders of magnitude. The higher order harmonics tend to demand higher statistics to produce a usable result. The run time on the cluster is in the order of $\sim$ 10 h for the type of simulations described, however the runtime may vary dependent on the number

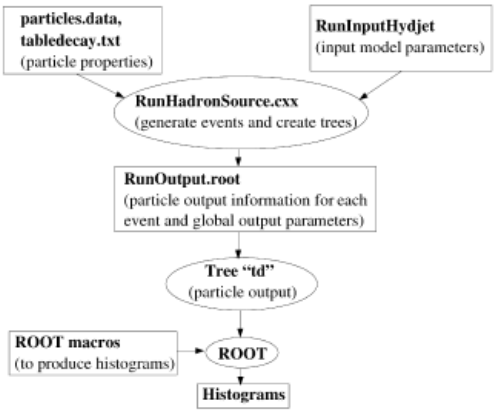

Figure 3.1: Principal sketch for HYDJET++ structure.

of users running code on the cluster. The produced data containers which are produced are added using the ubuntu "hadd" macro in order to add the containers and produce a copy with the statistics corresponding to the number of containers/events added. The resulting containers are displayed using macros written, using the Root package [115]. The macros are run on local LINUX workstations at the Physics Department at the University of Oslo, or even on the Abel cluster. The Root package has also been used on local Windows machines successfully. Finally, the plots are produced in the formats of choice and displayed. In addition, or prior to the data container producing runs, the code needs to be fine tuned in order to produce data which correlates to experimental data and also physical relevance. This type of work is of highest importance, especially when produced data is used in, not only first order, but also in higher order. The tuning work is tedious due to the high multiplicity needed. Maybe additional algorithms or procedures for tuning should be considered in the future.

The elliptic flow is simulated in terms of identified particles. The choice of particles was here limited to pions, antiprotons and lambdas. The pions and antiprotons are compared to data and related to lambdas. The simulated flow is displayed in terms of production modes in order to investigate the influence on the flow of different production modes. The simulated flow is then displayed within the number constituent quark model. Here, the production modes are showing their specific characteristics. The characteristics found in this investigation is further examined in the investigations of

higher order flows.

The unidentified elliptic and triangular flow is simulated for unidentified particles and compared to experimental data. The flows are necessary superposed on the experimental data, since the need for precision is due to further work with correlators and factorization. The precision is also needed for centralities, in order to reproduce as many features as possible of the participant matter. Thus model ellipticity and triangularity and also in addition, a pentagonal plane is established. Given the tune, the particle production modes are projected and investigated. The higher order flows are also simulated in the second, third and fifth event planes and compared to the corresponding factorizations. The higher order compound flows are then contextualized as terms in the expansions of flows. Analogies are then made to particle correlators.

The choice of experimental data is due to the preferred energy and mass, but also due to availability of data regarding retrievability and also variations of projections. The main body of work is done in terms of unidentified particles and transverse momentum dependence. Necessary is also integration of data and maybe correlators. The choice made, was then the ATLAS collaboration. The retrieval of data was solely done over the open web through the archives associated with Durham University. The choice of data source was done due to the availability of open data and the absence of available data and communication from the actual data sources. The integrity of the data might be questionable, however, checks are done against plots in published papers. The situation might not be optimal, but considered acceptable.

3.6 Summary

Simulating relativistic heavy ion collisions is of highest interest. In present paper, the investigation of hadronic genesis is initiated. The workflow of the simulation of relativistic heavy ion collisions is described. The simulation procedure of transverse momentum spectra and the simulation of the azimuthal anisotropy is reported. The hypothesis of simulating lower order flows, together with the investigation of different flow projections is made. The hypothesis of higher order compound flows as flow correlators are also made. Further, the elliptic and triangular flow are used in constructing compound terms of higher order flows. The flow is simulated in the HYDJET++ MC model and array run on the local computer cluster Abel. The lower order flows are compared to experimental data, which is retrieved from public open sources. Further, the higher order flows are investigated and conclusions and further hypothesises are made.

Chapter 4

Results

4.1 Introduction

The anisotropic flow and the associated transverse momentum spectra are means of observing the properties and the evolution of the matter produced in the relativistic heavy ion collisions. Anisotropic flow is characterized by initial conditions which is formed of the combined ion energy distributions and the microscopic matter interactions in the collisional stages. There are two main different models for the initial conditions. The Glauber model [25, 28], which is a geometric model and the colour glass condensate (CGC) model [116, 30], which is a modern model, based on chromo dynamical concepts. In this thesis, the Glauber model is the only model in use [69]. The initial conditions are modelled/parameterized in the Glauber multiple scattering model [26].

The initial shape of the fireball produced in the collision has an elliptic shape dependent on the centrality. This initial state shape evolves into an almost symmetric shape due to pressure gradients in the matter.

The expansion and cooling of the matter is dependent on the sound velocity of the matter. The velocity of the matter is in turn highly dependent on the equation of state, which is paramount in describing matter. Due to the evolution described above, the anisotropy in momentum space starts out at zero to evolve and reach its limit as the spatial anisotropy diminishes.

The softer regime (low p_T), is governed by a hydro dynamical evolution and shows that the flow is to a large extent built up in the earlier partonic stages of the evolution of the produced matter [92]. Later stages are probably not building up the anisotropic flow to any larger extent, however hadronic rescattering has some significance regarding the production of flow and transverse momentum spectra [41].

In the mid p_T range, the baryonic flow is lower than the mesonic flow. This phenomena is believed to originate in the earlier (hydrodynamic) stages of the matter evolution. The comoving quarks coalesce [117, 118, 119] into

hadrons and thus produce the mass scaling [120, 121, 45, 122], which is a consequence of the connection between kinetic energy and pressure gradients in the fireball, in particular the early stages of the matter evolution. This phenomena is referred to as constituent mass scaling and is treated in present paper.

The high p_T regime is characterized by fragmentation of high energy partons from initial hard scattering. The fragmentation process involves a hard scattering which produces partons, propagation through the media and the process of hadronization. The fragmentation for a parton into a hadron can be described within perturbative chromo dynamics and may be factorized as

$$E\frac{d\sigma}{d^3P} = \Sigma_p \int_0^1 dz \frac{D_{p\to h}(z)}{z^2} E_p \frac{d\sigma_p}{d^3P_p}, \tag{4.1}$$

where the fragmentation function $D_{p\to h}(z)$ [123] denotes the probability for the parton, p, to fragment into a hadron h, with the integrated first moment

$$\int_0^1 dx z D_{p\to h}(z) = 1. \tag{4.2}$$

The fragmentation functions have been fitted to experimental data [124]. The fit reveals a pion-to-proton fragmentation function ratio of ~ 10. I.e. the probability of a fragmentation produced pion is an order of magnitude larger than for the case of a proton for all momentum transferred.

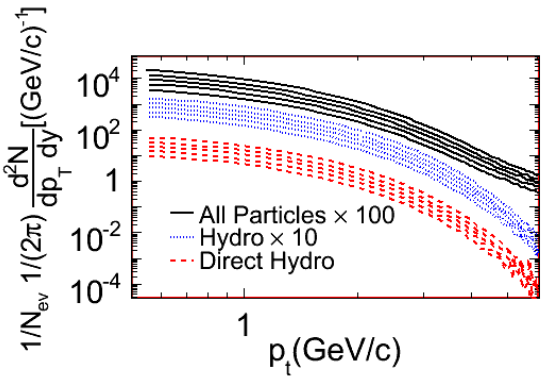

Figure 4.1: Spectra for unidentified particles. Different scaled production modes for all, hydro and direct hydro particles. Calculations for ATLAS setting, i.e. $\sqrt{s} = 2.76$ TeV and centralities (a) $\sigma/\sigma_{geo} = 0-5\%$, (b) $\sigma/\sigma_{geo} = 10-20\%$, (c) $\sigma/\sigma_{geo} = 20-30\%$ and (d) $\sigma/\sigma_{geo} = 30-40\%$ and (e) $\sigma/\sigma_{geo} = 40-50\%$.

The transverse momentum spectra is simulated for all inclusive particles and hydro dynamically produced particles (Fig. 4.1) . The modes are scaled for clarity and the plot is of a log-log type in order to display the difference of a thermal spectra (curved lines) and a power law spectra (straight lines). The inclusive spectra displays a predominantly thermal behaviour for $p_T \leq 3$ GeV and starts to display fragmentation for higher transverse momentum. The hydrodynamic spectra displays an approximate thermal behaviour for the whole region, however, the inclusive hydrodynamics displays a power law behaviour due to broadening for the high p_T regime, and also to some extent, for the soft regime due to decays. The probabilities might be modulated by the environment, e.g. the partons radiation field is modulated by the media traversed. This will be further investigated below.

The parton path through the dense medium is characterized by radiative [105, 106, 107, 108, 109] and collisional loss [125, 126, 127, 128] to the environment. The parton energy loss in the anisotropic system is, by definition, dependent on the energy and mass of the system, thus leading to the produced particle spectra and anisotropy. The energy loss is commonly quantified as the nuclear modification factor R_{AA} [129, 130, 66, 132].

As stated elsewhere, the anisotropic flow is described by the Fourier coefficients of the distribution [12]

$$E\frac{d^3N}{dp^3} = \frac{d^3N}{p_T dp_T dy d\phi} = \frac{1}{2\pi}\frac{d^2N}{p_t dp_t dy}(1+\sum_{n=1}^{\infty} 2v_n(p_T,y)\cos[n(\phi-\Psi_r)]), \quad (4.3)$$

with respect to the collision symmetry plane. A projection which describes the azimuthal anisotropy of the particle yield distribution is the anisotropic flow. The flow is defined as the projection in the n:th direction

$$v_n = \langle \cos\left[n\left(\phi - \Psi_n\right)\right]\rangle. \quad (4.4)$$

Where ϕ is the particle azimuth [10, 11, 12]. The symmetry plane Ψ_n, for the n:th harmonic, as a consequence of the event by event fluctuations of the partonic matter, the participant plane deviates from the reaction plane. This will produce odd harmonics which are non zero only due to fluctuations in, mainly, the initial conditions. Assuming a smooth matter distribution, the reaction plane and the plane of symmetry coincides, $\Psi_n = \Psi_{RP}$. The fluctuating plane is thus referred to as the participant plane(Ψ_{PP}), describing the event angular distribution of the participating particles.

The starting point in investigating the anisotropy of heavy ion collisions is the elliptic flow. The elliptic flow is defined as the second coefficient in (4.3). The p_T dependent flow can be used to investigate the freeze out conditions and the evolution of strongly interacting matter including phase transitions. Connected to the phase transition is the chiral symmetry restoration and deconfinement, i.e. fundamental aspects of modern physics, probing the

very nature of matter. Among the possible phenomena to investigate, is the energy loss of partons when traversing the matter, thus investigating the interactions of the hypothesized matter. The transport coefficients modulated by the energy loss is defining the viscosity for the produced matter, thus affecting the hypothesized hydro dynamical evolution.

4.2 Azimuthal Anisotropy

4.2.1 Elliptic Flow

The elliptic flow is calculated within the HYDJET++ model, described in chapter2. The elliptic flow is displayed for all centralities and is reproduced with great predictive power. The flow is calculated for centralities: $0-5\%$, $10-20\%$, $20-30\%$, $40-50\%$, using the HYDJET++ model [69]. The simulations are made for all unidentified particles and particles produced in hydro dynamical, i.e. soft and non perturbative processes, with and without decays. The simulations are displayed with experimental data.

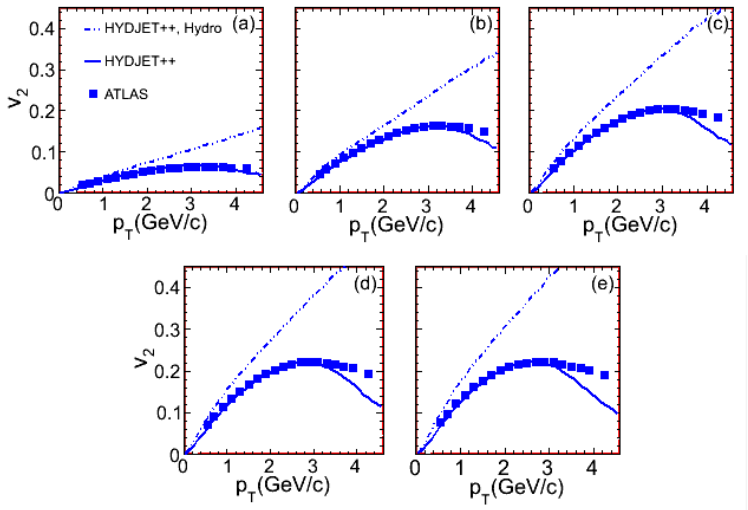

Figure 4.2: Elliptic flow for unidentified particles. Differential flow for unidentified particles and also for hydro dynamically produced particles, with and without particle decays. Calculations for ATLAS setting, i.e. $\sqrt{s} = 2.76$ TeV and centralities (a) $\sigma/\sigma_{geo} = 0-5\%$, (b) $\sigma/\sigma_{geo} = 10-20\%$, (c) $\sigma/\sigma_{geo} = 20-30\%$ and (d) $\sigma/\sigma_{geo} = 30-40\%$ and (e) $\sigma/\sigma_{geo} = 40-50\%$. Experimental data included for comparison [48].

The model ellipticity and triangularity has been parameterized to fit the experimental data. This provides a rarefaction of the participant energy distribution, thus providing a better fit to experimental data. The modulating

part is implemented by a three parameter fit run on the LINUX cluster at UiO (Abel) for convenience. Runtime was $\sim$ 10 h on a single node. The fit was a trivial c++ implementation. The elliptic flow does not increase monotonically as a function of ellipticity, but has a limiting behaviour due to the lower ability to transfer momentum [47] which overtakes the increase in ellipticity. The decrease in density due to centrality and the ionic density makes the speed of sound c_s lower, which is equivalent to lower ability to transfer momentum. This general feature is also seen in present simulation (Fig. 4.2).

The dependence on the fireball radius is seen to be strong for the semi soft ($\sim$ 1 GeV) region. This dependence is accounted for in model modifications in order to correspond to the characteristics of the matter distribution. This dependence is an indication of the dimensioning production mode in the particular p_T regime i.e. hydrodynamics and recombination is dependent on fireball radius in Fig. 4.2. The radius dependence in the factorizable region makes the fragmentation region shift to the more dilute, higher transverse momentum region for large fireball radius i.e. the anisotropic flow is largely defined by hydro dynamical particle genesis in geometrically symmetric systems. As stated above, the slope of the hydrodynamic curve is dependent on the curvature of the initial matter distribution, i.e. an extrapolation of the soft regime. This represents an almost pure thermal distribution, scaling the flow with the transverse momentum. This of course implies larger slope for higher fireball curvature i.e. higher centrality equals larger deviation from hydrodynamics. For the high p_T regime, the all inclusive flow calculations loses the predictive power, due to the lack of multiplicity and available experimental spectra.

The elliptic flow is reproduced to $\sim$ 3.5 GeV. The present model does not account for initial condition in a corresponding way due to the parameterized hydrodynamics used. This means that one might expect deviation from experimental data when fluctuations are dimensioning. Deviations connected to the initial conditions are not clearly visible in the calculations for differential elliptic flow. This type of deviation might be expected in central, initial condition dependent flow. Also, the model displays the expected integrated density dependent hydro dynamical behaviour. The level of fragmentation is seen to increase for centralities due to the increased diluteness and ellipticity of the matter distribution.

The calculations has been done with the fixed temperature of 165 MeV coming from the parameterization [112]

$$T(\mu_B) = a - b\mu_B^2 - c\mu_B^4, \tag{4.5}$$

with the parameters; $a = 0.166 \pm 0.002\text{GeV}, b = 0.139 \pm 0.016\text{GeV}^{-1}, c = 0.053 \pm 0.021\text{GeV}^{-3}$. For this simulation, the baryon potential is set to zero (unidentified particles). The thermal freeze out temperature is set to 105

MeV, with an freeze out time of 14.0 fm/c. The duration of particle emission is set to 3.5 fm/c. The baryonic, mesonic and strange potential are all set to zero for the distributions for unidentified particles [69]. Given the freeze out time for central hits $\tau = 14$ fm, the radius is assumed to be of order $R^2 = 14.0^2 - \tau_{Therm}$. Where the termalization temperature is denoted by τ_{Therm}. The central hit radius is here fitted to $R = 11.0$ fm.

The flow is further integrated in order to investigate the centrality dependence for different production modes. The spectra for corresponding projection thus has to be simulated as in Fig. 4.1.

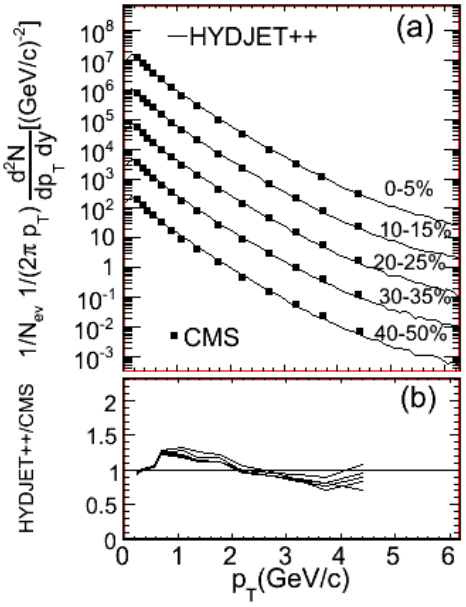

Figure 4.3: Spectra for unidentified particles. Spectra for all production modes. Calculations for CMS setting, i.e. $\sqrt{s} = 2.76$ TeV and scaled centralities (a) $\sigma/\sigma_{geo} = 0 - 5\% \times 10^4$, (b) $\sigma/\sigma_{geo} = 10 - 20\% \times 10^3$, (c) $\sigma/\sigma_{geo} = 20 - 30\% \times 10^2$ and (d) $\sigma/\sigma_{geo} = 30 - 40\% \times 10$ and (e) $\sigma/\sigma_{geo} = 40 - 50\%$. Experimental data included for comparison (CMS) [133].

The spectra for unidentified particles is simulated (Fig. 4.3). The calculated spectra agrees to a fair extent with the experimental data. Scaled centralities are displayed in the top pane and the HYDJET++ versus CMS ratio is displayed in the bottom pane for clarity. The spectra will be used for different production modes below as an aid in examining the anisotropic flow. From the plot, a nice agreement is seen between experimental data and simulation data for thermal, low p_T regime and the higher power law transverse momentum regime. Integration is mainly done in the $1 < p_T < 2$

and $2 < p_T < 3$ regime. The ratio is fairly flat in these regimes, so the integration error should be kept to a minimum, at least from the transverse momentum spectra.

The elliptic flow is known to be more dependent on centrality and mass than pure initial conditions (fluctuations). These type of deviations are more visible from the integrated flow. The integration is carried out according to

$$v_n{}^{\text{Int}} = \frac{\int dp_T p_T v_n \frac{dN}{p_T dp_T}}{\int dp_T p_T \frac{dN}{p_T dp_T}}. \tag{4.6}$$

The integration is carried out in the various (p_T) regions indicated on the plots in order to investigate the influence of the initial conditions including the radius and eccentricity on the different flows. The calculation for centralities are carried out and compared to experimental data (ATLAS).

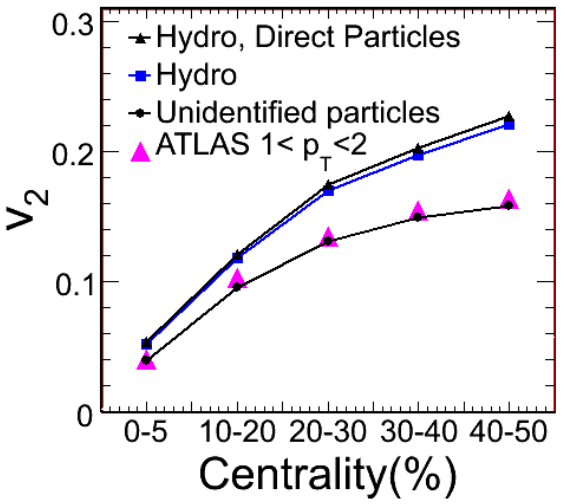

Figure 4.4: Integrated elliptic flow. The flow is calculated for $\sqrt{s} = 2.76$ TeV and $|\eta| < 2.5$ and is denoted by markers and lines. The flow is calculated for centralities: (a) $\sigma/\sigma_{geo} = 0 - 5\%$, (b) $\sigma/\sigma_{geo} = 10 - 20\%$, (c) $\sigma/\sigma_{geo} = 20 - 30\%$ and (d) $\sigma/\sigma_{geo} = 30 - 40\%$ and (e) $\sigma/\sigma_{geo} = 40 - 50\%$. Experimental data is included for comparison (ATLAS) [48].

In the integrated regime $1 < p_T < 2$ GeV/c, (Fig. 4.4), the main production mode is hydrodynamics for lower centralities and gets shifted towards fragmentation for higher centralities due to increased ellipticity. The predictive power of the calculations are seen to be quite high for the integrated elliptic flow. Deviations are seen for the larger centralities, however due to the smallness of the deviation, it is unclear whether the deviation is due to parameterization of initial conditions or the particularities of the fragmentation production mode.

The hydrodynamic flow is monotonous and increasing for centralities due to increasing eccentricity. The hydrodynamics displays an *anfang* to a limiting behaviour due the non scaling of pressure gradients and momentum production. Visible is also the scattering from decays. The effect is in this regime rather small, however consistent.

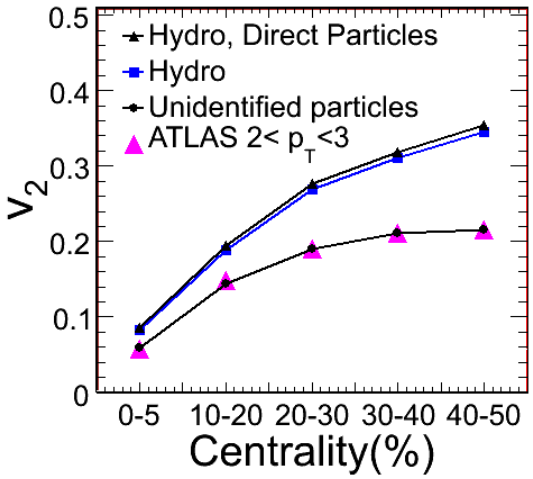

Figure 4.5: Integrated elliptic flow. The flow is calculated for $\sqrt{s} = 2.76$ TeV and $|\eta| < 2.5$ and is denoted by markers and lines. The flow is calculated for centralities: (a) $\sigma/\sigma_{geo} = 0 - 5\%$, (b) $\sigma/\sigma_{geo} = 10 - 20\%$, (c) $\sigma/\sigma_{geo} = 20 - 30\%$ and (d) $\sigma/\sigma_{geo} = 30 - 40\%$ and (e) $\sigma/\sigma_{geo} = 40 - 50\%$. Experimental data is included for comparison (ATLAS) [48].

The elliptic flow is also integrated as in Fig. 4.5, in the $2 < p_T < 3$ GeV regime according to (4.6). The flow is now believed to be dominated by fragmentation (Fig. 4.2). The flow is now reproduced to a high degree of accuracy, likely due to the more extensive calculations involved in the fragmentation regime [69]. The precision is equally high for all simulated centralities. The limiting behaviour is clearly visible in the plot. This behaviour is due to the higher levels of fragmentation in the particular p_T regime. In addition to simulations for inclusive and hydro flow, the simulated flow for directly produced particles from hydro dynamical processes is included. The flow for direct particles is slightly higher than the flow produced by inclusive hydrodynamics. This slight elevation in flow from direct particles stems from a lesser amount of scattering from decays, thus a higher degree of coherence. This decay induced scattering appears to be identical relatively in the two regimes of integration relative the hydrodynamic flow.

An attempt to integrate the elliptic flow for the $0.5 \leq p_T$ GeV regime is made (Fig. 4.6). Due to difficulties in reproducing the transverse momentum spectra in the low transverse momentum regime, the integrated flow is

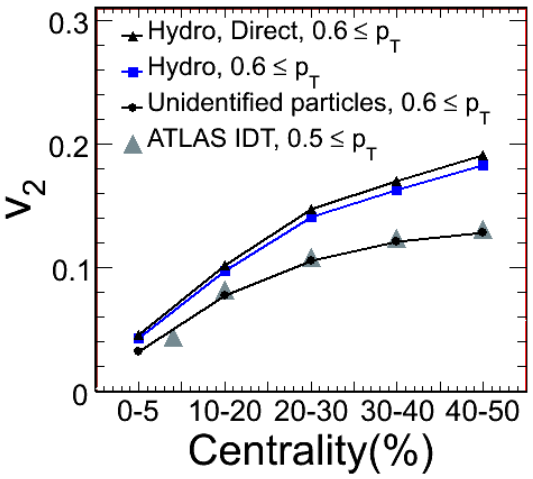

Figure 4.6: Integrated elliptic flow. The flow is calculated for $\sqrt{s} = 2.76$ TeV and $|\eta| < 2.5$ and is denoted by markers and lines. The flow is calculated for centralities: (a) $\sigma/\sigma_{geo} = 0 - 5\%$, (b) $\sigma/\sigma_{geo} = 10 - 20\%$, (c) $\sigma/\sigma_{geo} = 20 - 30\%$ and (d) $\sigma/\sigma_{geo} = 30 - 40\%$ and (e) $\sigma/\sigma_{geo} = 40 - 50\%$. Experimental data is included for comparison (ATLAS) [137].

seen to deviate substantially. This is likely a consequence of the difficulties in simulate the low p_T decays in a quantitative correct way. Some constraints on the decay thresholds might improve the situation. As a temporary remedy, the simulated flow is integrated in a slightly displaced regime, i.e. the $0.6 \leq p_T$ GeV regime. This makes it possible to draw *some* conclusions regarding the centrality dependence for the whole regime. As expected, the trend is reproduced for all centralities except for central hits. The difference is here hydrodynamics closer resemble the inclusive flow. This is due to the low transverse momentum regime, where the flow is to a large extent dimensioned by hydrodynamic particle genesis.

As a complement, the transverse momentum spectra is simulated and displayed (Fig. 4.7). The hydrodynamics spectra is seen to approximate the inclusive spectra. In the lower pane, a comparison with the inclusive spectra is made. The hydro spectra is $\sim 80\%$ of the all-particle spectra, while the direct hydro is $\sim 20\%$ in the model. Also visible is the thermal spectra for the hydro dynamical particles and the power law spectra for all particles in the high $3 \leq p_T$ region.

In order to investigate the flow further, the elliptic flow for the various production modes is simulated (Fig. 4.8). The simulation is done within the HYDJET++ model, using its projective features in order to extract the flow for different particle production modes. The flow modes are displayed for hydro dynamically produced particles, particles produced in jet processes,

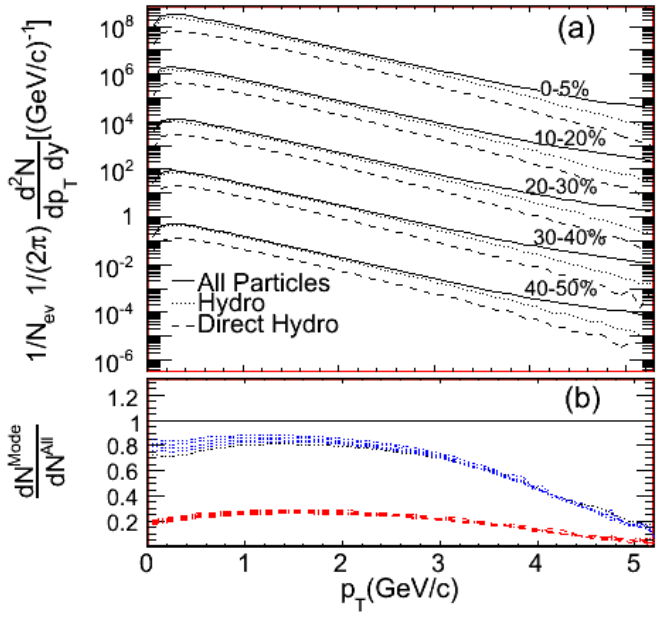

Figure 4.7: Spectra for unidentified particles and different production modes. Calculations for ATLAS setting for all particles, hydro dynamically produced particles and direct hydro. Particles simulated for $\sqrt{s} = 2.76$ TeV and scaled centralities (a) $\sigma/\sigma_{geo} = 0 - 5\%$, (b) $\sigma/\sigma_{geo} = 10 - 20\%$, (c) $\sigma/\sigma_{geo} = 20 - 30\%$ and (d) $\sigma/\sigma_{geo} = 30 - 40\%$ and (e) $\sigma/\sigma_{geo} = 40 - 50\%$.

directly produced particles and direct particles coming from hydrodynamics. The hydro dynamically produced particles has a soft p_T regime which is hard to reproduce due to physical constraints on particle decays.

The hydro part is suppressed for the low transverse regime relative direct hydro particles. The onset of decays suppresses the hydro flow through the incoherence introduced by particle decays. For the high p_T regime, the flow is monotonically increasing due to distribution momentum conservation. The flow is ordered due to the initial fireball curvature. Higher curvature equals higher ellipticity, which, in turn, produces higher hydrodynamic flow.

The particles produced in jets displays a monotonically increasing flow. The behaviour of the jet flow is due to the sparser phase space, which makes less rescattering, which combined with the collective motion create the flow. The flow for the direct particles scales with the inclusive flow due to the decay nature of the elliptic flow. For higher transverse momentum, the decay part is defining due to the specific production modes. The direct particles gains in flow due to denser media (centrality). The direct hydrodynamic particles has in general higher flow than hydro particles. The lack of soft decays makes the low transverse momentum regime higher and monotonous.

The high p_T regime is almost identical to the hydro flow. This reveals the importance of decays for the low and mid p_T range.

In general one can hypothesize that the decays suppresses the flow through the decrease of coherence introduced by decay scatter [134]. The Integrated flow displays the same difference in flow for decays vs. non-decayed hydro particles for both integration intervals. I.e. this effect is visible for all possible projections.

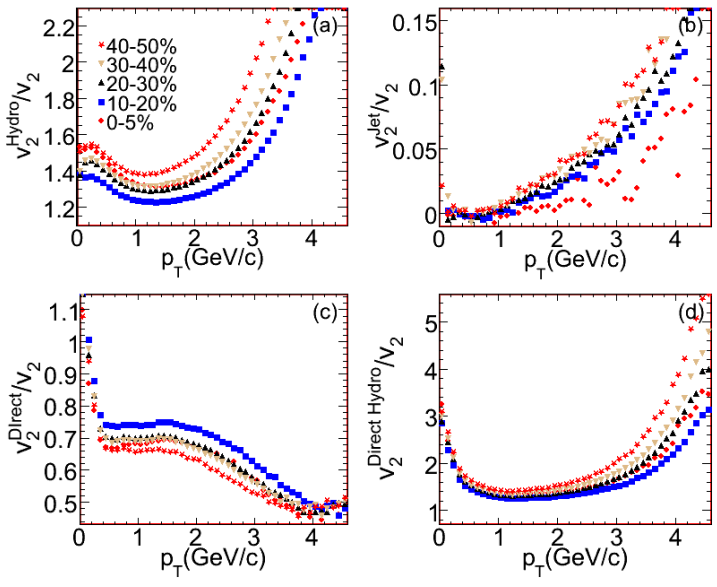

Figure 4.8: Elliptic flow for different modes. Modes simulated with HYDJET++. Flow mode is plotted relative to all inclusive flow. The flow is calculated for centralities: (a) $\sigma/\sigma_{geo} = 0 - 5\%$, (b) $\sigma/\sigma_{geo} = 10 - 20\%$, (c) $\sigma/\sigma_{geo} = 20 - 30\%$ and (d) $\sigma/\sigma_{geo} = 30 - 40\%$ and (e) $\sigma/\sigma_{geo} = 40 - 50\%$.

4.2.2 Triangular Flow

The triangular flow is believed to be generated by the third participant eccentricity

$$\epsilon_3 = -\frac{\langle r^3 e^{i3(\phi-\Psi_3)}\rangle}{\langle r^3\rangle}. \tag{4.7}$$

As stated elsewhere in present paper, the eccentricity for a smooth spherical distribution is

$$\langle r^3 e^{i3(\phi-\Psi_3)}\rangle \propto \int_0^{2\pi} \rho(r) d\phi e^{i3(\phi-\Psi_3)} \propto \rho(r) e^{i3(\phi-\Psi_3)}\Big|_0^{2\pi} = 0. \tag{4.8}$$

The triangular flow is thus dependent on fluctuations, mainly in the initial conditions. Since the triangular flow is assumed to be fluctuation dependent, the triangular flow has finer geometric characteristics, thus providing us with an observable which is sensitive to viscosity and initial geometry. The triangular flow is simulated and is displayed for centralities (Fig. 4.9). The second *and* third event plane are implemented in the model, and is referred to as Ψ_2 and Ψ_3.

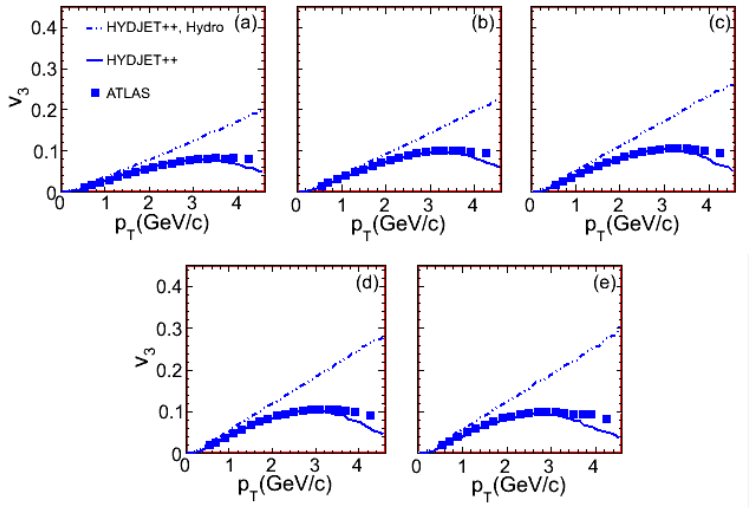

Figure 4.9: Triangular flow for unidentified particles. Differential, all inclusive flow and also for hydro dynamically produced particles. Calculations for ATLAS setting, i.e. $\sqrt{s} = 2.76$ TeV and centralities (a) $\sigma/\sigma_{geo} = 0-5\%$, (b) $\sigma/\sigma_{geo} = 10-20\%$, (c) $\sigma/\sigma_{geo} = 20-30\%$ and (d) $\sigma/\sigma_{geo} = 30-40\%$ and (e) $\sigma/\sigma_{geo} = 40-50\%$. Experimental data included for comparison (ATLAS) [48].

The triangular flow is seen in Fig. 4.9 to be reproduced to great precision. Along with the inclusive p_T dependence is the flow for hydro dynamically

produced particles. Contrary to the elliptic flow, the triangular flow hydrodynamic dependence is approximatively static, due to the dependence on fluctuations and not ellipticity. The hydro dynamical regime persist to $\sim$ 1.5 GeV for all centralities. This is consistent with the picture of fluctuating initial conditions, slightly increasing due to the diluteness of the distribution thus producing the triangular flow.

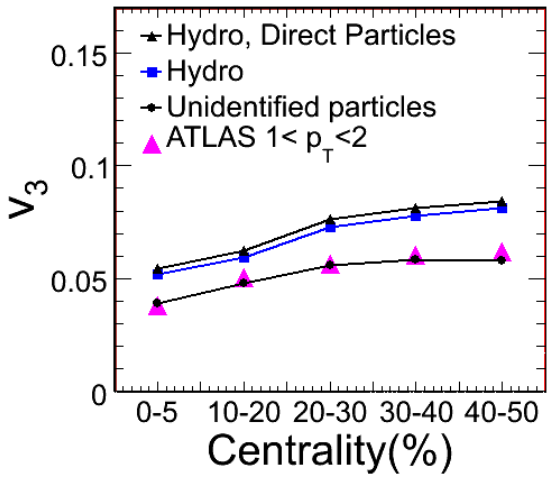

Figure 4.10: Integrated Triangular flow. The flow is calculated for $\sqrt{s} = 2.76$ TeV and $|\eta| < 2.5$ and is denoted by markers and lines. Atlas experimental data is also included for comparison (Markers) [48].

The triangular flow is integrated for different p_T regimes, in order to investigate the dependence of e.g. initial conditions and matter evolution on the v_3 (Fig. 4.10).

The flow is integrated in the $1 < p_T < 2$ regime and is fairly well reproduced. There are some minor deviations, likely to stem from parameterization of initial conditions. The flow is seen to increase slowly with centrality, up to 35%. This appears to be the optimal initial condition regarding momentum transfer in the third (fluctuating) event plane mostly due to the geometric initial distribution. Also included, is the simulated flow for hydro dynamically and direct hydro dynamically produced particles. The hydrodynamics is here seen to follow the inclusive flow to a higher degree compared to the case of elliptic flow due to the fluctuating nature of v_3. This means that the triangular flow is characterized by a lesser degree of coherence which differentiates the triangular flow less due to fragmentation throughout the whole simulation centrality range. Again, the directly produced particles produces a slightly higher flow due to the lack of decay scatter.

The triangularity is integrated for the $2 < p_T < 3$ regime as in Fig. 4.11.

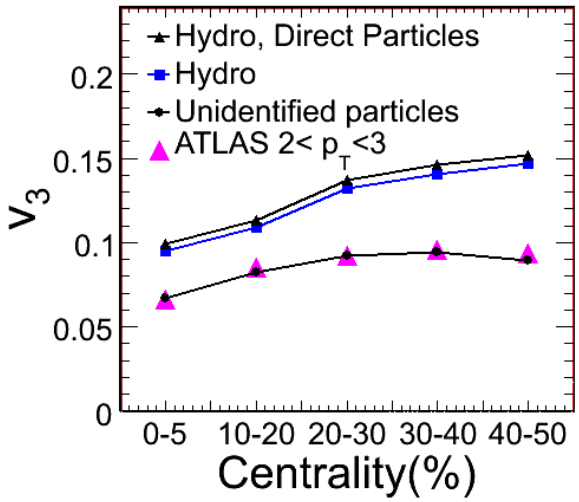

Figure 4.11: Integrated Triangular flow. The flow is calculated for $\sqrt{s} = 2.76$ TeV and $|\eta| < 2.5$ and is denoted by markers and lines. Atlas experimental data is also included for comparison (Markers) [48].

This regime is expected to be characterized by fragmentation production modes in contrast to the lower p_T regime. This is visible for the higher centralities, where the flow reaches its upper limit for the optimized $\sim 35\%$ regime and then clearly diminish for the highest centrality due to lower density. The weak dependence of centrality is also visible. This in addition to the mentioned characteristics is a display of fluctuation flow genesis. The triangular flow deviates from hydrodynamics to a higher degree for the higher transverse momentum regime, than for the $1 < p_T < 2$ regime. This is interpreted as a higher relative level of fragmentation. The direct hydro dynamical particles again possesses a higher degree of coherence due to suppressed decay scattering.

4.2.3 Relation between v_2 and v_3

The different modes of anisotropy can be related to each other as of the digress elsewhere in present paper. First, the relation between the elliptic and triangular flow is investigated. The ratio is displayed for different production modes (Fig. 4.12). The triangular flow is seen favoured by more central hits due to the fluctuative characteristics of the triangular flow versus the build-up of elliptic flow as a function of ellipticity. From the simulations, the dependence of decays works in favour of v_3 for centralities. This manifest itself as a diminishing of the centrality dependence of the ratio due to fluctuation for central hits. As mentioned elsewhere, this is an interesting feature of anisotropic flow and coherence of particle decays and the coupling

between decays and confinement related processes (coalescence).

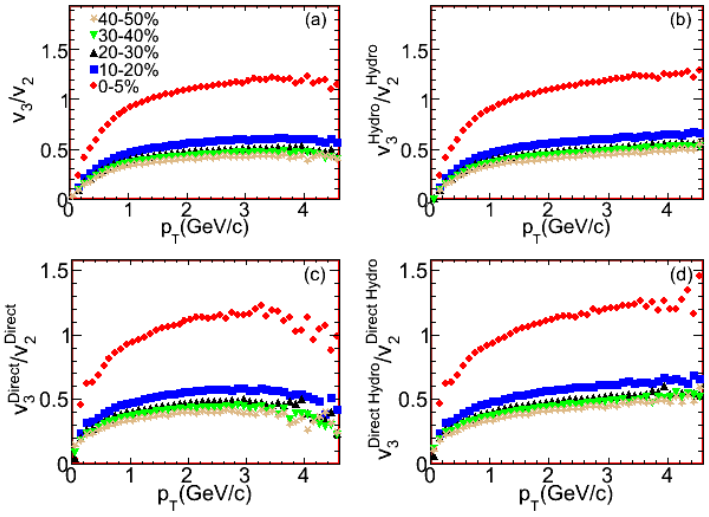

Figure 4.12: Triangular flow for modes relative same mode for elliptic flow, v_3/v_2. The flow is calculated for centralities: (a) $\sigma/\sigma_{geo} = 0-5\%$, (b) $\sigma/\sigma_{geo} = 10-20\%$, (c) $\sigma/\sigma_{geo} = 20-30\%$ and (d) $\sigma/\sigma_{geo} = 30-40\%$ and (e) $\sigma/\sigma_{geo} = 40-50\%$. Flow is calculated for an ATLAS setting. $\sqrt{s} = 2.76$ TeV, $|\eta| < 2.5$.

4.2.4 Influence of v_2 and v_3 on higher harmonics

In order to investigate the importance of the elliptic and triangular flows on higher order harmonics, the higher order flows are investigated in lower order planes as stated elsewhere in present paper [135]. The hexagonal flow is examined in the model Ψ_2 and Ψ_3 plane. For reference, the flow expansion for the hexagonal flow is stated here in addition to the theoretical chapter 2

$$\begin{aligned} v_6 =& e^{i6(\phi_6-\Psi_6)}w_6 + e^{i(2\phi_2+4\phi_4-6\Psi_6)}w_6^{24} + e^{i(6\phi_3-6\Psi_6)}w_6^{33} \\ &+ e^{i(5\phi_5+\phi_1-6\Psi_6)}w_6^{15} + e^{i(6\phi_2-6\Psi_6)}w_6^{222} + \dots . \end{aligned} \tag{4.9}$$

The third and fourth term in the expansion (4.9) is primarily examined. Here, the matter eccentricity answer, i.e. w_m^{ijk} denotes the influence of the planes i,j,k on the m:th flow. The answer is here examined as the anisotropic flow in corresponding planes. The hexagonal flow is simulated in the second and third event plane and displayed on the same plot (Fig. 4.13).

The plot displays dependence on initial conditions for the hexagonal flow in the second and third event plane (Fig. 4.13). The high levels of fluctuations are clearly seen in the simulations of the hexagonal flow in

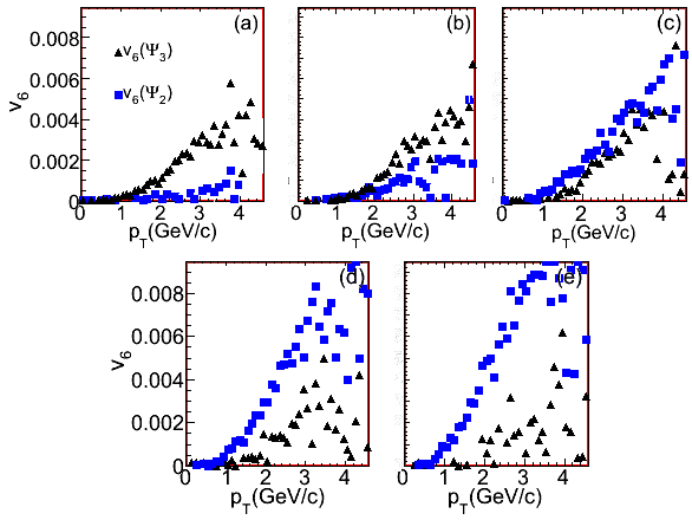

Figure 4.13: Hexagonal flow in model Ψ_2 and Ψ_3 planes. Calculations made for $\sqrt{s} = 2.76$ TeV, $|\eta| < 2.5$ and centralities (a) $\sigma/\sigma_{geo} = 0 - 5\%$, (b) $\sigma/\sigma_{geo} = 10 - 20\%$, (c) $\sigma/\sigma_{geo} = 20 - 30\%$, (d) $\sigma/\sigma_{geo} = 30 - 40\%$ and $\sigma/\sigma_{geo} = 40 - 50\%$.

the third event plane along with the dependence of initial conditions. The density effect on the triangular plane is enhanced by the higher wave number of the hexagonal flow. The sharper peaks makes a lesser coherence producing environment for the fluctuating flow. The triangular flow thus diminishes for centrality in a more articulated way than the triangular flow in its own plane. The hexagonal flow in the second event plane is displaying the characteristics of the initial eccentricity to high degree. The relative high wave number counter acts the diminishing pressure gradient answer, thus projecting the initial eccentricity to a higher degree than the elliptic flow.

The hexagonal flow is integrated for the $1 < p_T < 2$ regime and for different production modes (Fig. 4.14). The hexagonal flow displays a monotonous behaviour for the relevant centralities. The monotony is due to the ellipticity dependence and a combination of the cohering effect of higher wave numbers, thus having a fluctuation flow part. The hydro dynamically generated flows are significantly higher since jets diminishes the flow due to the elliptic initial conditions. The lack of scattering decays further elevates the flow. The decay scattering gets more severe due to the lowering of opacity, thus enhancing the in-media decay scattering relative hydrodynamics without decays. This is most prominent in the coalescence region ($1 < p_T < 2$ GeV), where quark recombination is significantly suppressed due to lowering of particle coherence.

The hexagonal flow is further investigated in the second event plane by

integrating the flow in the $2 < p_T < 3$ regime as of Fig.4.15. The flow is now higher due to the higher transverse momentum regime, which is characterized by fragmentation and dependent on ellipticity. The different hydrodynamic modes are now practically superposed. This is due to lower levels of hydro dynamical particles relative the direct particles, which makes the hydro dynamics closer to direct hydrodynamics.

The hexagonal flow in the third event plane is further integrated in

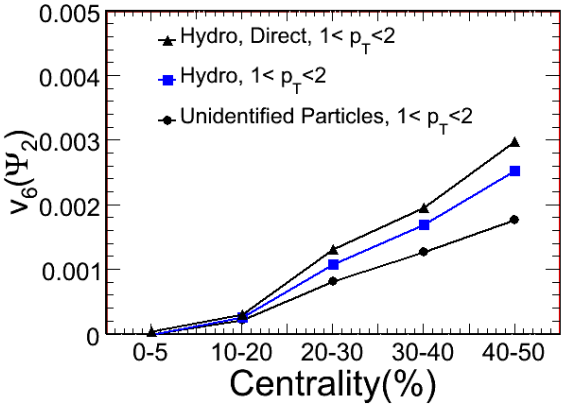

Figure 4.14: Integrated hexagonal flow in second event plane. Calculations made for $\sqrt{s} = 2.76$ TeV, $|\eta| < 2.5$ and centralities; $\sigma/\sigma_{geo} = 0-5\%$, $10-20\%$, $20-30\%$, $30-40\%$ and $40-50\%$. The flow is integrated for the regime $1 < p_T < 2$.

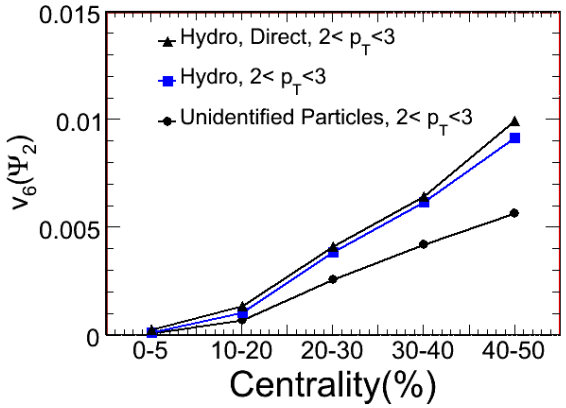

Figure 4.15: Ratio of hexagonal flow and elliptic flow squared in Ψ_2 plane. Calculations made for $\sqrt{s} = 2.76$ TeV, $|\eta| < 2.5$ and centralities; $\sigma/\sigma_{geo} = 0-5\%$, $10-20\%$, $20-30\%$, $30-40\%$ and $40-50\%$. The flow is integrated for the regime $2 < p_T < 3$.

the $1 < p_T < 2$ regime (Fig. 4.16). The flow is seen to diminish due to the initial ellipticity, in the hydro or coalescence regime. Due to the nature of v_3, the flow decreases with density of matter. The flow is hardly distinguishable for different production modes. It is also highly suppressed due to the fluctuation of the third event plane versus the high coherence production modes characterizing the p_T region.

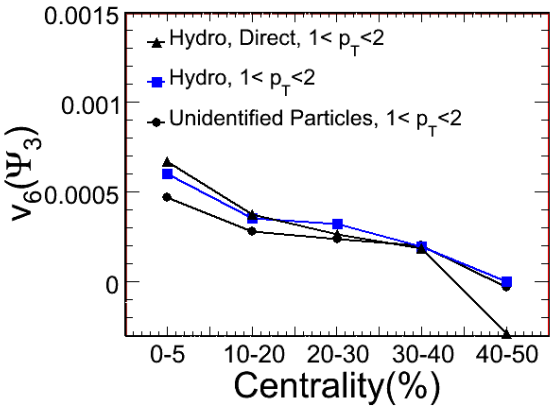

Figure 4.16: Integrated hexagonal flow in the third event plane. Calculations made for $\sqrt{s} = 2.76$ TeV, $|\eta| < 2.5$ and centralities; $\sigma/\sigma_{geo} = 0-5\%$, $10-20\%$, $20-30\%$, $30-40\%$ and $40-50\%$. The flow is integrated for the regime $1 < p_T < 2$.

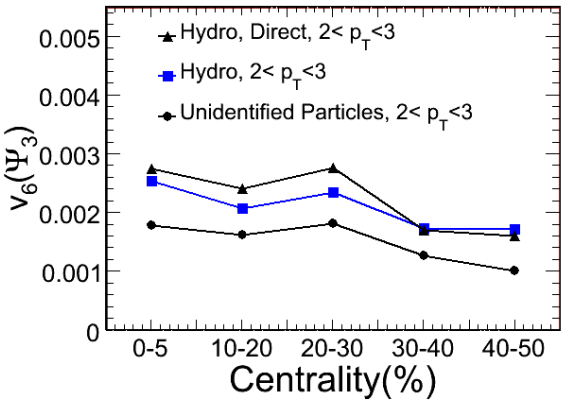

Figure 4.17: Integrated hexagonal flow in the third event plane. Integration made for all modes, hydro dynamical modes and direct hydro dynamical produced particles. Calculations made for $\sqrt{s} = 2.76$ TeV, $|\eta| < 2.5$ and centralities; $\sigma/\sigma_{geo} = 0-5\%$, $10-20\%$, $20-30\%$, $30-40\%$ and $40-50\%$. The flow is integrated for the regime $2 < p_T < 3$

The flow is also integrated in the third event plane for the higher transverse momentum regime $2 < p_T < 3$ in Fig. 4.17. The hexagonal flow is now seen to be higher in the $2 < p_T < 3$ regime than in the lower transverse momentum regime. Now the particle production modes are of a more fluctuating nature. Given the lesser dependence on initial ellipticity due to production mode, the flow is now significantly less dependent on centrality. The jets still provides an incoherence due to the fluctuations of the third event plane, thus suppressing the hexagonal flow significantly. The incoherence produced by the inclusive hydro dynamical flow is here suppressing the flow to a minor degree.

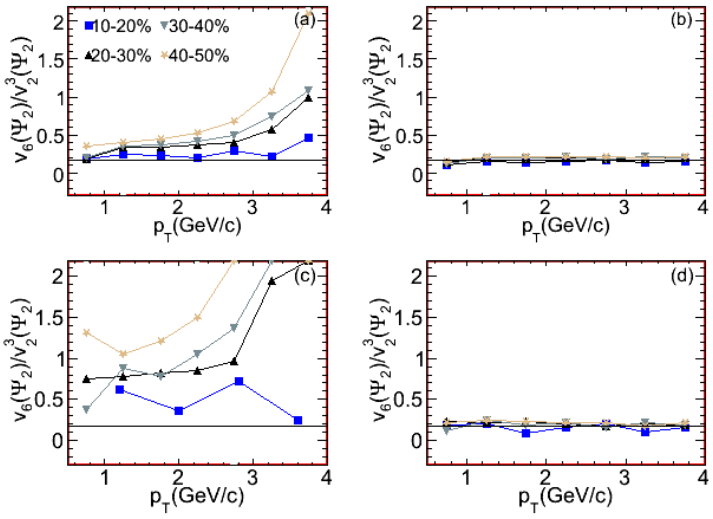

Figure 4.18: Ratio of hexagonal flow and elliptic flow in Ψ_2 plane. Calculations made for $\sqrt{s} = 2.76$ TeV and centralities (a) $\sigma/\sigma_{geo} = 0 - 5\%$, (b) $\sigma/\sigma_{geo} = 10 - 20\%$, (c) $\sigma/\sigma_{geo} = 20 - 30\%$, (d) $\sigma/\sigma_{geo} = 30 - 40\%$ and $\sigma/\sigma_{geo} = 40 - 50\%$.

Factorization is investigated as $v_6(\Psi_2) \propto v_2^3(\Psi_2)$ (4.9). The ratio $\frac{v_6}{v_2^3}$ is tested for different modes in Fig. 4.18. The ratio scales to a high degree for hydrodynamics. The scaling seem to hold with or without decays included in the simulations. Including jets, however, will elevate the flow significantly. The hexagonal flow will maintain for higher transverse momentum, due to the increase in wave number, the sixth harmonic does not get "quenched" in the same rate as the elliptic flow. As a conclusion, the scaling is approximately true, at least for hydro dynamically produced particles since the higher wave number is incompatible to the second order plane for fluctuations.

The same investigation is made for the quadratic Ψ_3 term in (4.9). The ratio is displayed for different production modes, i.e. all inclusive particles,

hydro dynamically produced particles and direct hydro particles Fig. 4.19. The scaling is seen to be weak for all particles, largely due to jet production. The non scaling is highest for lower centralities due to the initial geometry of the fireball. The higher p_T particles tends to fluctuate to a higher degree, and is therefore enhancing the hexagonal flow relative the triangular product. In line with this statement, the hydro dynamically produced particles displays a higher degree of scaling. This is due to jet production, which differs in coherence relative the sixth and third event plane, and again the difficulties in scaling the coherence incompatible sixth and third harmonics is evident.

The ratio v_6/v_3^2 is integrated and displayed for different production modes (Fig. 4.20). The ratio diminishes for higher ellipticity as a consequence of the ellipticity of the fireball, or the directionality of the geometry, which makes the Ψ_3 lose coherence, and more so with a higher wave number. The ratio is seen to be independent of production mode for the specific p_T regime. This is in turn due to the low levels of jet production for the low p_T regime.

The ratio is further integrated for the regime $2 < p_T < 3$ GeV (Fig. 4.21). The ratios jet dependence is now clearly visible for all centralities due to its higher wave number. The difference is constant for all centralities as a consequence of the model proportionality of jet production [69].

In order to investigate the ratio v_6/v_2^3, the ratio displayed in Fig. 4.22 is integrated for the two transverse momentum regimes $1 < p_T < 2$ GeV and $2 < p_T < 3$ GeV. The ratio is seen to increase for centralities (Fig.

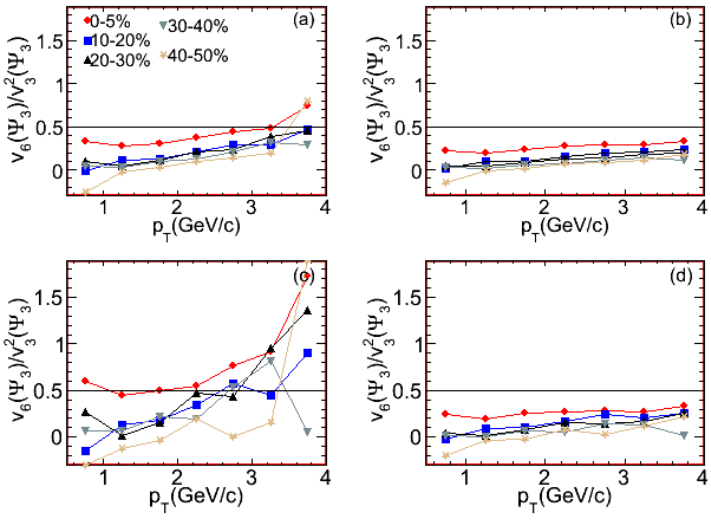

Figure 4.19: Ratio of hexagonal flow and triangular flow squared in Ψ_3 plane. Calculations made for $\sqrt{s} = 2.76$ TeV, $|\eta| < 2.5$ and centralities; $\sigma/\sigma_{geo} = 0-5\%$, $10-20\%$, $20-30\%$, $30-40\%$ and $40-50\%$.

4.22). This increase is due to the monotony of the ellipticity. The jets will because of this increase in importance with centrality due to the higher wave number of the elliptic dependent hexagonal flow. The hydro dynamically produced particles displays an approximate invariance to initial ellipticity. This less fluctuating production mode is scaling due to its elliptic compatible behaviour. It is seen that the hexagonal flow is favoured by the less scattered direct particle mode in the specific coalescence production regime.

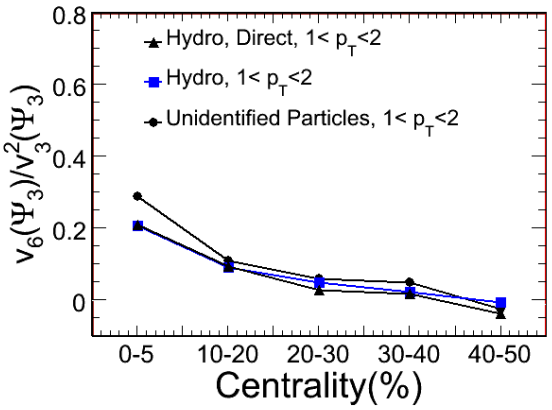

Figure 4.20: Integrated ratio of hexagonal flow in third event plane and triangular flow squared. Calculations made for $\sqrt{s} = 2.76$ TeV, $|\eta| < 2.5$ and centralities; $\sigma/\sigma_{geo} = 0-5\%$, $10-20\%$, $20-30\%$, $30-40\%$ and $40-50\%$. The ratio is integrated in the regime $1 < p_T < 2$ GeV.

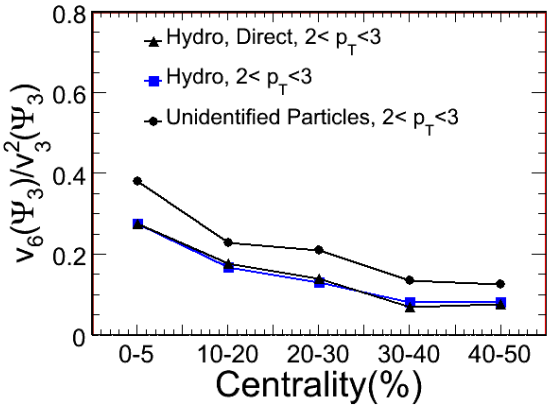

Figure 4.21: Integrated ratio of hexagonal flow in the third event plane and triangular flow squared. Calculations made for $\sqrt{s} = 2.76$ TeV, $|\eta| < 2.5$ and centralities; $\sigma/\sigma_{geo} = 0-5\%$, $10-20\%$, $20-30\%$, $30-40\%$ and $40-50\%$. The flow is integrated for $1 < p_T < 2$ GeV.

The higher transverse momentum regime is also integrated (4.23). The same behaviour is seen here as for the low p_T regime. The particle production mode favours the jet dependent hexagonal flow to an even higher degree due to the fragmentation regime. Here the lesser degree of decays makes the hydro dynamical particles indistinguishable.

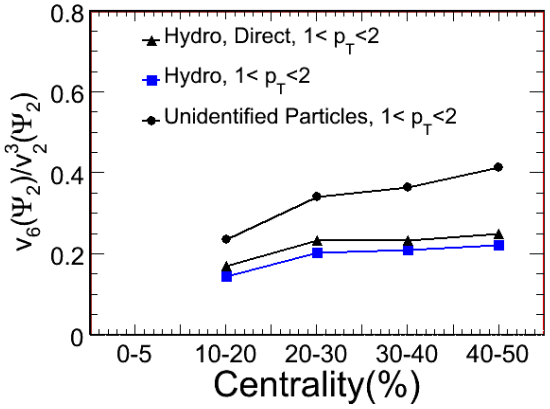

Figure 4.22: Integrated hexagonal flow in the second event plane. Calculations made for $\sqrt{s} = 2.76$ TeV, $|\eta| < 2.5$ and centralities; $\sigma/\sigma_{geo} = 0 - 5\%$, $10 - 20\%$, $20 - 30\%$, $30 - 40\%$ and $40 - 50\%$. The flow is integrated for $1 < p_T < 2$ GeV.

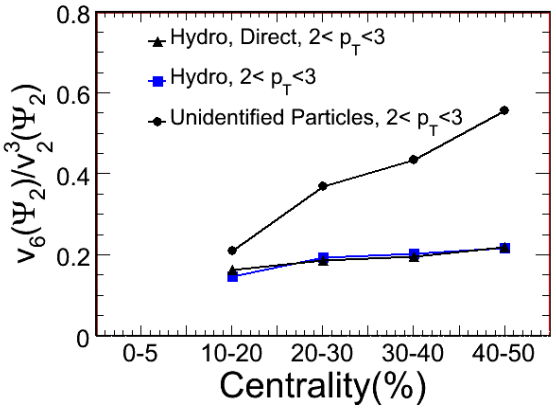

Figure 4.23: Integrated hexagonal flow third event plane. Integration made for $2 < p_T < 3$ GeV.

In order to further investigate the influence of elliptic and triangular flow on higher order harmonics, the contribution from the second and third event plane to the pentagonal flow as the second term in the expansion (chap. 2)

$$\begin{aligned} v_5 = e^{i5(\phi_5-\Psi_5)}w_5 + e^{i(2\phi_2+3\phi_3-5\Psi_5)}w_5^{23} + e^{i(4\phi_4+\phi_1-5\Psi_5)}w_5^{14} \\ + e^{i(2\phi_2+2\phi_2+\phi_1-5\Psi_5)}w_5^{221} + e^{i(3\phi_3+\phi_1+\phi_1-5\Psi_5)}w_5^{311} + \dots . \end{aligned} \tag{4.10}$$

The answer to the initial ellipticity, w_5^{23}, is here assumed to be proportional to v_2v_3. The hypothesis of

$$v_2v_3 \propto v_5(\phi - \Psi_2 - \Psi_3), \tag{4.11}$$

is tested and analyzed through the hypothesized constant ratio (4.11).

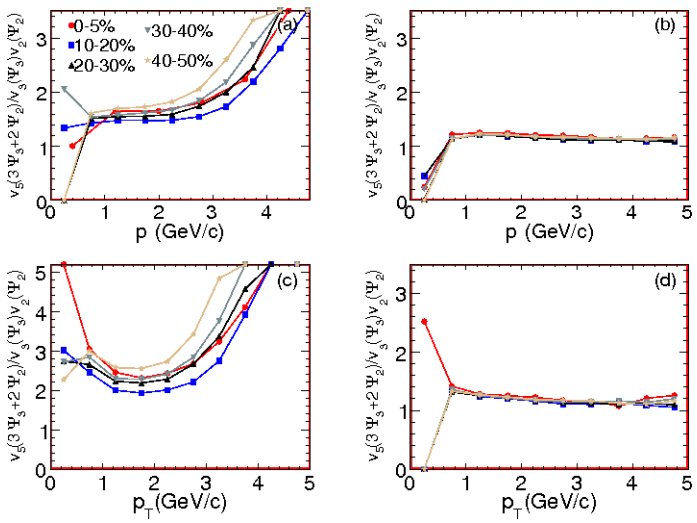

Figure 4.24: The nonlinear flow answer to the Ψ_2 and Ψ_3 plane. Lines denote calculated flow (HYDJET++). The calculations are made in an ATLAS setting, with $\sqrt{s} = 2.76$ TeV and centralities (a) $\sigma/\sigma_{geo} = 10 - 20\%$, (b) $\sigma/\sigma_{geo} = 20 - 30\%$, (c) $\sigma/\sigma_{geo} = 30 - 40\%$ and (d) $\sigma/\sigma_{geo} = 40 - 50\%$.

The ratio is tested for different centralities and particle production modes (Fig. 4.24). The scaling holds for the mid transverse momentum range ($0.5 < p_T < 3$) for all particles. The factorization is seen to be affected by jets due to initial conditions. The factorization condition for v_2v_3 is derived analogous to the discussion regarding the hexagonal flow in different event planes. The product is

$$v_2v_3 \propto \langle \cos\left(2\phi_\alpha + 3\phi_\beta - 2\Psi_2 - 3\Psi_3\right)\rangle. \tag{4.12}$$

The factorization is a "two-plane correlator". In order to factorize, the pentagonal, nonlinear flow is likely to need a lower degree of correlation to the nonlinear pentagonal plane, i.e. hydrodynamic flow. Which makes the correlator (4.12) approach the hypothesized pentagonal Ψ_2, Ψ_3 flow. The absence of jets provides for a lesser degree of coherence with the pentagonal flow, which matches the factorization and the pentagonal flow. The scaling is seen to be almost exact for hydrodynamics.

The case with direct inclusive particles is interesting. Here the effect of decays is clearly visible in the light of higher wave numbers. The scaling is fair with jets included, but gets destroyed with decays excluded. The decays thus is counteracting the non-factorization due to higher wave number in the pentagonal flow versus the $v_2 v_3$ factorization. An interesting study would be to quantify the decays through the wave number of the particular flow by investigating different factorizations versus the corresponding correlators. Further, the pentagonal flow is integrated for the $1 < p_T < 2$ GeV transverse momentum regime.

For the linear pentagonal flow, the integrated flow is seen to conform with the experimental flow to a high degree (Fig. 4.25). The flow is only weakly dependent on initial centrality thus displaying a dependence on fluctuations. The hydro dynamical flows are significantly higher, due to the absence of jets which quenches the pentagonal flow. The additional absence of decays provides an additional flow component due to lesser decay scatter.

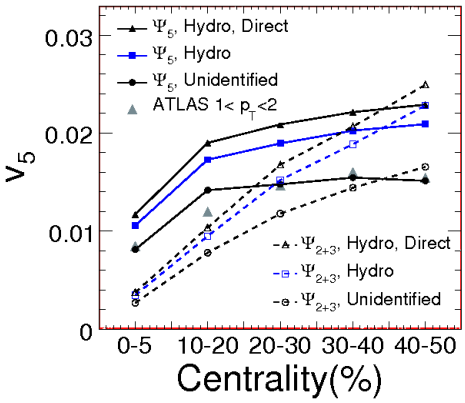

Figure 4.25: Integrated Pentagonal flow. The solid lines denote pentagonal flow in the Ψ_5 plane and the dashed lines denotes the nonlinear pentagonal flow contribution from the second and third eve plane. The calculations are made in an ATLAS setting, with $\sqrt{s} = 2.76$ TeV and centralities (a) $\sigma/\sigma_{geo} = 10 - 20\%$, (b) $\sigma/\sigma_{geo} = 20 - 30\%$, (c) $\sigma/\sigma_{geo} = 30 - 40\%$ and (d) $\sigma/\sigma_{geo} = 40 - 50\%$.

The pentagonal flow from the second and third event plane is highly

dependent on centrality due to the contributions from the second event plane. The hierarchy is the same as in the case for the pentagonal flow.

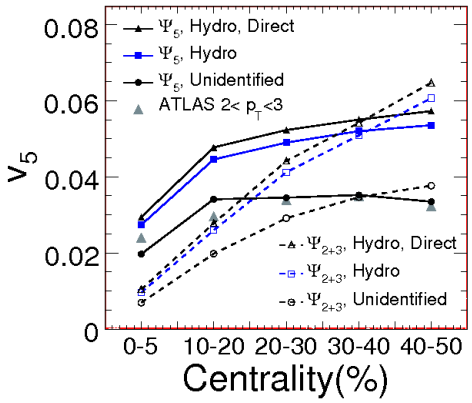

Figure 4.26: Integrated Pentagonal flow. The solid lines denote pentagonal flow in the Ψ_5 plane and the dashed lines denotes the nonlinear pentagonal flow contribution from the second and third event plane. The calculations are made in an ATLAS setting, with $\sqrt{s} = 2.76$ TeV and centralities (a) $\sigma/\sigma_{geo} = 10 - 20\%$, (b) $\sigma/\sigma_{geo} = 20 - 30\%$, (c) $\sigma/\sigma_{geo} = 30 - 40\%$ and (d) $\sigma/\sigma_{geo} = 40 - 50\%$.

The higher transverse momentum regime, displayed in Fig. 4.26, has approximately the same levels of flow as the lower transverse momentum regime.

4.2.5 Flow Correlators

The pentagonal and hexagonal flow in the elliptic Ψ_2, triangular Psi_3 event-plane are simulated. In the simulations, the correlators are displayed as:

$$C_{\Psi_2} = \frac{\langle\cos(2[\phi_1+\phi_2+\phi_2-3\Psi_2])\rangle}{v_2 v_2 v_2} \tag{4.13}$$

$$C_{\Psi_3} = \frac{\langle\cos(3[\phi_1+\phi_2-2\Psi_3])\rangle}{v_3 v_3} \tag{4.14}$$

$$C_{\Psi_5} = \frac{\langle\cos([2\phi_1+3\phi_2-2\Psi_2-3\Psi_3])\rangle}{v_2 v_3}. \tag{4.15}$$

Thus representing factorization. And also

$$C_{6\Psi_2} = \frac{\langle\cos(2[\phi_1+\phi_2+\phi_2-3\Psi_2])\rangle}{\cos(6[\phi-\Psi_2])} \tag{4.16}$$

$$C_{6\Psi_3} = \frac{\langle\cos(3[\phi_1+\phi_2-2\Psi_3])\rangle}{\cos(6[\phi-\Psi_3])} \tag{4.17}$$

$$C_{5\Psi_5} = \frac{\langle\cos([2\phi_1+3\phi_2-2\Psi_2-3\Psi_3])\rangle}{\cos(5\phi-2\Psi_2-3\Psi)}. \tag{4.18}$$

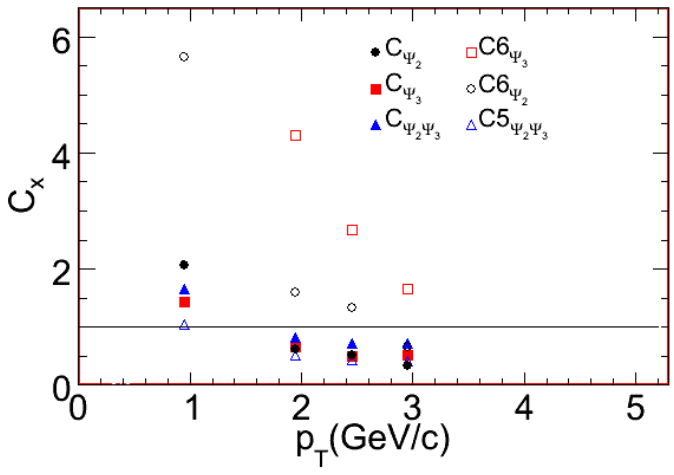

Figure 4.27: Multi particle correlators. Flow correlators in second, third and fifth event plane. The correlators are displayed relative corresponding flow factorization. Calculations made with $\sqrt{s} = 2.76$ TeV and centrality $\sigma/\sigma_{geo} = 20 - 30\%$.

The flow correlators are displayed in Fig. 4.27 relative the factorization $(C_{\Psi_2}, C_{\Psi_3}, C_{\Psi_2+\Psi_3})$ and also relative the pentagonal and hexagonal flow in the elliptic, triangular and pentagonal planes $(C6_{\Psi_2}, C6_{\Psi_3}, C5_{\Psi_2\Psi_3})$. Factorization for the flow is seen for $p_T \sim 1.5$ GeV. The correlator is equal to higher harmonics only for higher transverse momentum.

The correlators are also displayed on their own (Fig. 4.28)

$$C_2 = \frac{\langle\cos(2[\phi_1+\phi_2-3\Psi_2])\rangle}{\cos(6[\phi-\Psi_2])} \tag{4.19}$$

$$C_3 = \frac{\langle\cos(3[\phi_1+\phi_2-2\Psi_3])\rangle}{\cos(6[\phi-\Psi_3])} \tag{4.20}$$

$$C_5 = \frac{\langle\cos([2\phi_1+3\phi_2-2\Psi_2-3\Psi_3])\rangle}{\cos(5\phi-2\Psi_2-3\Psi)}. \tag{4.21}$$

Here, the correlators are displaying their differentiated transverse momentum. The pentagonal correlator displays a momotonous behaviour due to the elliptic and triangular contributions, while the elliptic correlator displays an alternating p_T behaviour, while the triangular correlator displays a quenched behaviour due to fluctuations.

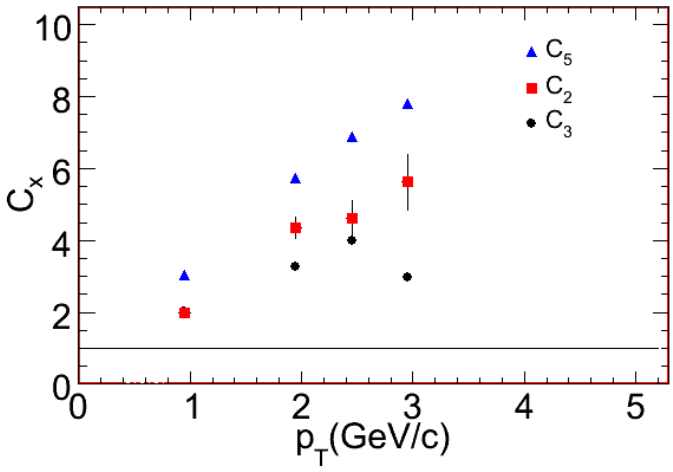

Figure 4.28: Multi particle correlators. Flow correlators in second, third and fifth event plane. Calculations made with $\sqrt{s} = 2.76$ TeV and centrality $\sigma/\sigma_{geo} = 20 - 30\%$.

4.3 Coalescence model

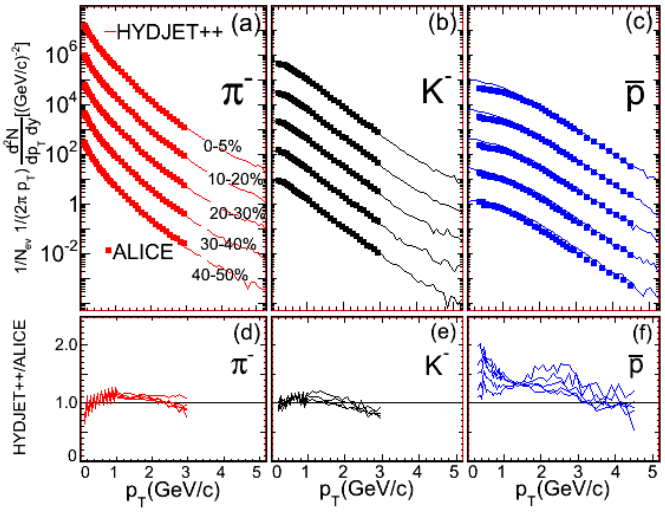

Figure 4.29: Spectra for identified particles. The calculations are made in an ALICE setting, with $\sqrt{s} = 2.76$ TeV and rapidity $|\eta| < 0.8$. Comparison between theory and experimental data in lower panes. Simulations and data is scaled for.

The relativistic heavy ion collisions provides a laboratory for investigating strongly interacting matter. The matter produced in the collisions is hypothesized to undergo phase transitions in its path to detection. Under investigation is parton deconfinement and chiral symmetry restoration. The observable commonly in use is the anisotropic flow. Anisotropic flow is characterized by momentum transfer and particle coherence. This makes for a suitable observable connected to properties of the early stages of the produced matter evolution. The coalescence models main thesis is the concept of constitutive, or dressed (massive) quarks [117].

The mass scaling observed in the spectra (Fig. 4.29), is probably due to the increase in mean transverse momentum, since the differential flow does not change with significance. The ordering is totally reversed for higher momentum $\sim 3GeV$. This reversal is due to the number of constituents. I.e. the baryons carries more flow due to a larger number of constituents. At large transverse momentum, the yield is assumed to have a large fragmentation contribution of energetic partons produced in initial scatterings with a high level of momentum transfer. These high energy partons loses energy when travelling through the media. The energy loss is treated elsewhere in present paper and is dependent on the path length travelled and thus the azimuth of the particles are affected. This will generate an anisotropy and consequently an elliptic flow component due to the energy loss, which

persists to $p_T \sim 8 - 20$ GeV. To separate the coalescence regime from the partonic loss regime, the flow of identified particles is examined. The coalescence regime is thus approximated to end where the protonic and pionic flow coincides.

The model is based on the idea of the proportionality of the particle spectra to the product of the invariant particle spectra, i.e. [117].

$$\frac{dN_B}{dp_x dp_y} = A_B \left[\frac{dN_q}{dp_x dp_y} (\frac{p_T}{3}) \right]^3 \tag{4.22}$$

$$\frac{dN_M}{dp_x dp_y} = A_M \left[\frac{dN_q}{dp_x dp_y} (\frac{p_T}{2}) \right]^2. \tag{4.23}$$

Here, the constant A is dependent on the number of constituents in the observed hadron. The alternatives 3 and 2 in the formula reflects the fact of the dependence on constitutive quarks, three for baryons (B), and two for mesons (M). This approach is connected to non-conservation of energy and narrow phase space wave functions. Assuming a truncated azimuthal distribution and (4.22), some algebra yields

$$\begin{aligned} 1 + 2v_{2B}\cos(2\phi) &\propto (1 + 2v_{2q}(p_T/3)\cos(2\phi))^3 \\ &= 1 + 6v_{2q}(p_T/3)\cos(2\phi) + 12v_{2q}^2(p_T/3)\cos^2(2\phi) \\ &+ 8v_{2q}^3(p_T/3)\cos^3(2\phi) \\ &\approx 1 + 6v_{2q}(p_T/3)\cos(2\phi). \end{aligned} \tag{4.24}$$

Here, the right side of (4.24) is dependent on the quark flow v_q. An identification yields the coalescence flow relation between hadrons and constituent (massive) quarks.

$$v_{2B} = 3v_{2q}(p_T/3) \tag{4.25}$$

$$v_{2M} = 2v_{2q}(p_T/2). \tag{4.26}$$

As seen from (4.25), the coalescence model depends on collectivity in the expanding fireball. The relation (4.24) might be dependent on higher order terms on either left or right side. The modes can be and are several and dependent on e.g. transverse momentum [118]. In the high p_T regime, where the flow is at its peak, the coalescence model breaks down. Here, the formed hadron have larger transverse momentum and the partons only carries a fraction of the hadron momentum $dN_h(p_T) \sim dN_q(p_T/z)$. In the soft region with its high and different quark distributions, where the interactions are of a non-linear kind, the coalescence model (4.22) breaks down. The second semi soft regime might be considered as the most beneficial for quark coalescence, due to the linear interactions which provides for the coalescence model.

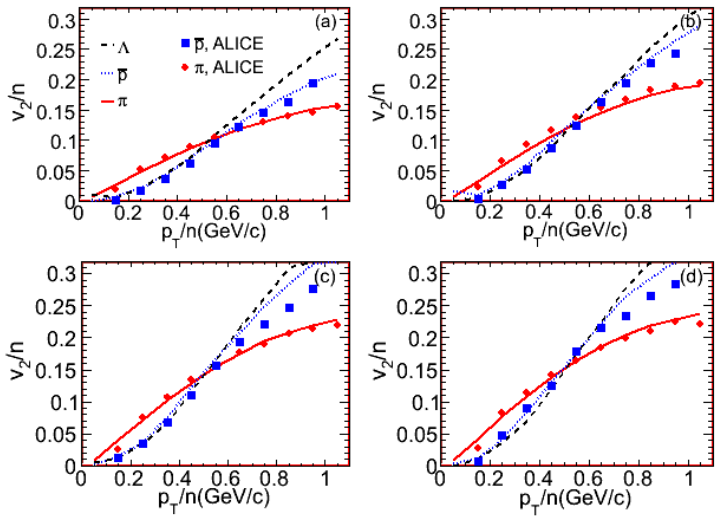

Figure 4.30: Elliptic flow in coalescence model. Lines denote calculated flow (HYDJET++), and markers denote experimental data [121] for species. The calculations are made in an ALICE setting, with $\sqrt{s} = 2.76$ TeV and centralities (a) $\sigma/\sigma_{geo} = 10 - 20\%$, (b) $\sigma/\sigma_{geo} = 20 - 30\%$, (c) $\sigma/\sigma_{geo} = 30 - 40\%$ and (d) $\sigma/\sigma_{geo} = 40 - 50\%$.

In Fig. 4.30, the predicted coalescence behaviour is clearly visible. The non-linear interactions makes the flow in the soft regime deviate from the assumption of superposition (scaling). The meson and baryon flow thus deviate and are not found to be superimposed. In the semi-soft regime, the meson and baryon flow scales to a first approximation. This might be interpreted as an indication of quark coalescence due to factorization of the distributions (4.22). In this regime, the quarks are seen as dressed partons. As an effect of deconfinement, at least in the early stages of the matter evolution, the meson (baryons) achieves two (three) times the flow of a quark, due to the increase in coherence relative to single quarks as a consequence of the confined mesonic (baryonic) state. For the high transverse momentum regime, the coalescence model breaks down due to the mentioned increase in hadron production through fragmentation due to the non scaling of transverse momentum.

The quark scaled flow is calculated for particles directly generated by hydrodynamics, displayed in Fig. 4.31. The coalescence regime is here seen to set in at $p_T \sim 0.7$ GeV. This is due to the prolonged dense phase space regime, where the quark distributions convolve. Also seen here, is the effect of the absence of decays for lighter hadrons. The pions display an elevated flow in the softer region due lesser scattering from decays. Further, the decays are seen to differentiate the proton and lambda flow due to different

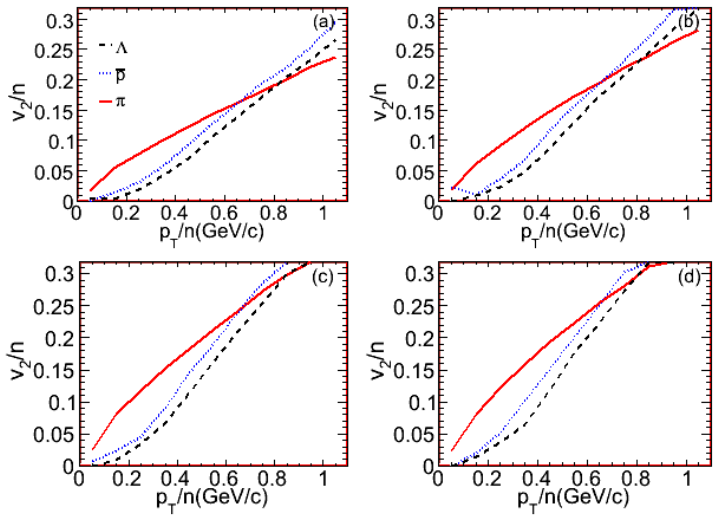

Figure 4.31: Elliptic flow in coalescence model. Flow is calculated for directly produced particles from hydrodynamic flow generation. Lines denote calculated flow (HYDJET++). The calculations are made in an ALICE setting, with $\sqrt{s} = 2.76$ TeV and centralities (a) $\sigma/\sigma_{geo} = 10 - 20\%$, (b) $\sigma/\sigma_{geo} = 20 - 30\%$, (c) $\sigma/\sigma_{geo} = 30 - 40\%$ and (d) $\sigma/\sigma_{geo} = 40 - 50\%$.

decay channels.

Constituent Mass Scaling

One of the major goals of RHIC studies is the study of hot and dense strongly acting matter with partonic constituents. The difficulty of observing the different phases of matter is setting the agenda for finding new observables. I.e. the actual matter under observation is the particles which travelled the macroscopic distances of the detector and thus is detected as a distinct particle with a certain momentum. Studies at RHIC has led to the hypothesis that hadrons form via coalescence or recombination of massive quarks. A key to understand this type of particle formation mode, is the observation of quark number constituent scaling. This observable, under the hypothesis, carries information of chiral symmetry restoration, and deconfinement and thus have great importance. The shared view is that the constituent number quark scaling (NCQ) is directly connected to the additivity of partonic cross sections. As of above, the scaling (4.25) is in both anisotropy and in transverse momentum. The differentiation in flow for species is mass dependent due to hydrodynamics. The mass dependence is clearly visible in e.g. Fig.4.30. In order to explore this hypothesis, the flow is attempted to be made mass invariant using the derivation above. The starting point is then the (mass dependent) spectra

$$\frac{dN}{p_T dp_T} = \frac{dN}{m_T dm_T} \propto \frac{dN}{dm_T^2}. \tag{4.27}$$

In order to make (4.27) mass independent the squared mass translates the squared transverse mass as $\{m_T^2 \rightarrow m_T^2 - m^2\}$. This yields the distribution

$$\frac{dN}{dm_T^2} = \frac{dN}{d\big[(m_T - m)(m_T + m)\big]} = \frac{dN}{(m_T + m)dm_T + (m_T - m)dm_T}, \tag{4.28}$$

which is interpreted as the approximate mass scaled distribution, given the dimensioning part $(m_T - m)dm_T = (m_T - m)d(m_T - m)$,

$$\frac{dN}{dm_T^2} \sim \frac{dN}{(m_T - m)d(m_T - m)}. \tag{4.29}$$

The mass scaling variable is then defined as

$$KE_T = m_T - m_0, \tag{4.30}$$

where m_T is commonly referred to as transverse mass, $m_T^2 = m^2 + p_T^2$. In order to compensate for the constitutive differences in baryons and mesons, the flow *and* the kinetic transverse energy is scaled by the number of quarks as of (4.25) such that $v_2 \rightarrow v_2/n_q$, and $KE_T \rightarrow (m_T - m_0)/n_q$. This hypothesis is then investigated, using the flow simulations and the experimental data.

The flow for identified particles is calculated and scaled according to the prescription above. The calculations are compared to experimental data and are made only with a LHC (2.76 TeV) setting in Fig. 4.32. For the transverse momentum and the mass scaled flow, the particular features of the particle species are identified. Antiproton shows a smaller flow than the mesons for low transverse momentum. This feature is reproduced in the HYDJET model and is likely due to the mass scaling hypothesis where the antiproton suffers a higher level of coherence loss due to coalescence. Further, the antiproton simulation differs slightly from experimental data for higher KET. This is likely due to later (inelastic) [41] rescattering and possible annihilation and pair production. Pions are simulated with excellent precision. The soft regime has some minor deviations, likely due to the difficulties in reproducing the particle number cross sections to the highest degree of precision. The precise simulation is maintained for the whole measured p_T region. The flow scales as a good approximation for $KE_T < 1GeV/c^2$. In that regime, the mass ordering is due to the fact that the pressure gradient acting on the different species characterizes the flow. Between the protons and the pions, the direct connection between pressure gradients and flow is not linear. The prediction from the simple hypothesis of mass scaling would be that the flow scales with transverse kinetic energy with minor deviations. I.e. the pressure gradient or eccentricity, and the kinetic energy of the particle is

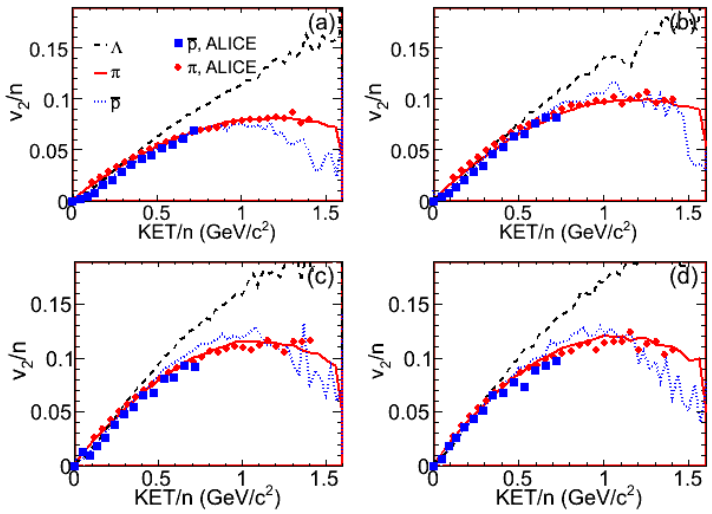

Figure 4.32: Elliptic flow in constituent mass scale model. Flow is calculated for identified particles; pions, antiprotons and lambdas. Lines denote calculated flow (HYDJET++). The calculations are made in an ALICE setting, with $\sqrt{s} = 2.76$ TeV, transverse rapidity $|\eta| < 0.8$ and centralities (a) $\sigma/\sigma_{geo} = 10 - 20\%$, (b) $\sigma/\sigma_{geo} = 20 - 30\%$, (c) $\sigma/\sigma_{geo} = 30 - 40\%$ and (d) $\sigma/\sigma_{geo} = 40 - 50\%$. Experimental data for comparison [121].

connected. The relative mesonic and baryonic scaling might be interpreted as a sign of early quark degrees of freedom and initial deconfinement.

The same mass scaling simulations are made for hydro dynamically produced particles, in order to investigate the deviations from the mass scale model. As of Fig. 4.33, mass scaling is quite accurate. Pions deviate slightly from protons and lambdas in the soft region, likely due to the mentioned deviation from mass scale due to formation potentiality. The increase in the calculated mass scaling is now hypothesized to stem from the absence of hard processes such as jets and inelastic scattering, which may be hypothesized to produce coherence. The simulations still include decays, which means that only hard processes are left out in this particular simulation.

In order to investigate the mass scaling further, the scaled flow is calculated for directly produced soft particles (hydro dynamical) Fig. 4.34. The flow is now calculated for particles produced in soft processes without decay products. The baryon and mesonic flow is now seen to deviate. The lack of decays means that the light (mesonic) pion distribution scatters less and as a consequence gains the most. The particle decays thus are essential in order to fulfil the constituent quark number mass scaling.

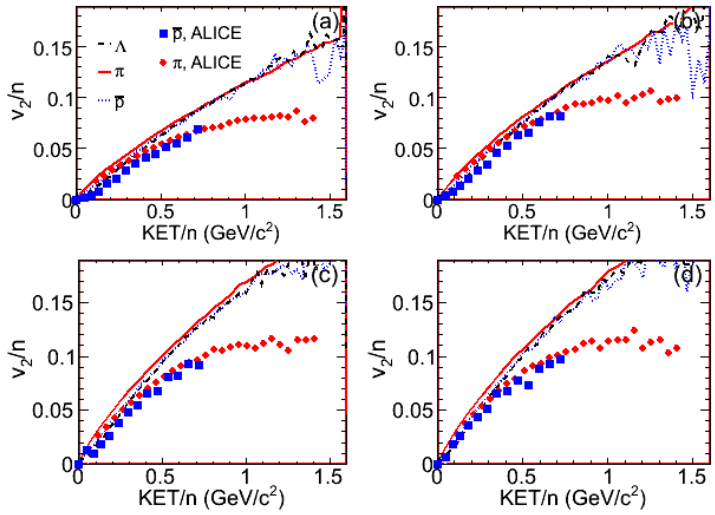

Figure 4.33: Elliptic flow in constituent mass scale model. Flow is calculated for identified particles which originates from hydrodynamics and soft processes. Experimental data is included for reference (Markers). Lines denote calculated flow (HYDJET++). The calculations are made in an ALICE setting, with $\sqrt{s} = 2.76$ TeV, transverse rapidity $|\eta| < 0.8$ and centralities (a) $\sigma/\sigma_{geo} = 10 - 20\%$, (b) $\sigma/\sigma_{geo} = 20 - 30\%$, (c) $\sigma/\sigma_{geo} = 30 - 40\%$ and (d) $\sigma/\sigma_{geo} = 40 - 50\%$. Experimental data is included [121].

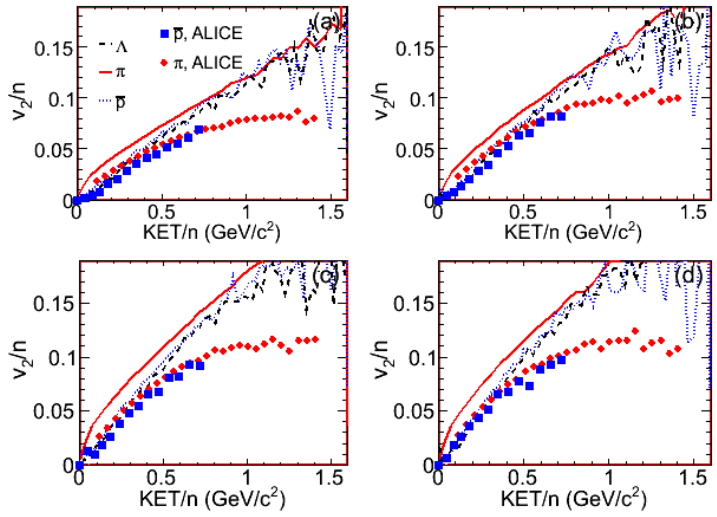

Figure 4.34: Elliptic flow in constituent mass scale model. Flow is calculated for identified particles directly produced out of hydro dynamical processes. Experimental data from [121] Lines denote calculated flow (HYDJET++). The calculations are made in an ALICE setting, with $\sqrt{s} = 2.76$ TeV and centralities (a) $\sigma/\sigma_{geo} = 10 - 20\%$, (b) $\sigma/\sigma_{geo} = 20 - 30\%$, (c) $\sigma/\sigma_{geo} = 30 - 40\%$ and (d) $\sigma/\sigma_{geo} = 40 - 50\%$. Experimental data is included [121].

4.4 Summary

The elliptic and triangular flow is seen to be reproduced with a high level of accuracy for the $p_T < 3.5$ GeV. The associated transverse momentum spectra is also reproduced with a fair level of accuracy. This makes the integrated flow reproduced with excellent precision also. The soft regime of the transverse momentum spectra has minor deviations from the experimentally obtained spectra, likely due to soft decays and associated thresholds. The different particle production modes are projected and displayed. The particles produced in soft processes, in general displays higher levels of coherence. The soft flow without decays, in general produces an even higher level of coherence due to the lack of scattering decays. The results for the elliptic and triangular flows are all coherent, displaying values, not deviating form theoretical predictions. Higher order flows are also simulated and displays coherent results. The different higher order flows displays factorizations to some extent. Corresponding two, three and nonlinear compound correlators are displayed and may be of use investigating experimental flow. Constituent quark number scaling is investigated for the elliptic flow. The elliptic flow is simulated with great precision for the $p_T < 3.5$ GeV regime for protons and pions. Lambdas are also simulated without any comparison to experimental data. The particles displays scaling in line with experimental data. The production modes for the particles are projected and displays a coherent behaviour. The decays are seen to couple with the coalescence regime and are necessary in order for light mesons to scale in the constituent quark number scaling model.

Chapter 5

Discussion

The anisotropic flow is hypothesized to be possible to simulate with great precision, in order to make higher order predictions in the transverse momentum space and also for centrality bins in the (0-50%) regime.

The different flows are bound to be simulated from the same statistical set of generated hadrons [114, 69]. This, together with the reproduction of the transverse momentum spectra is providing a solid foundation for further work related to high energy, heavy ion collisions. Given this hypothesis, the modes for hadron genesis are possible to simulate and extract. Further, the compound, higher order flows built on the hypothesized Ψ_2, Ψ_3, Ψ_5 paradigm is then hypothesized to reveal novel information regarding particle coherence.

Connected to the investigation of hadron genesis for unidentified particles, is the investigation of identified particle flow and associated transverse momentum spectra. Hypothesized for this thesis is the observations of particle decays and confinement within the constituent quark number scaling model, which are to be seen in connection with the investigation of unidentified particle flow and transverse momentum spectra.

The distributions observed in experiments for unidentified particles are simulated with great accuracy [64, 152]. The azimuthal anisotropy and the transverse momentum spectra are compared to experimental LHC data [48, 132, 133], and displays great accuracy in the $p_T < 3.5$ GeV regime. A corresponding precision is seen in the centrality dependence $(0 - 50\%)$ of the simulated particle flow [48, 137]. The flows are also integrated in order to compare the centrality dependence for different hadronization modes.

The elliptic flow displays lower transverse momentum dependence for lower centralities. The lower dependence is due to lesser direction of pressure gradients in the initial momentum distribution. The flow is then more isotropic, thus displaying lower levels of flow. For higher centralities, the higher pressure gradients corresponds to higher transverse momentum, seen for the hydro dynamical projection. The transverse momentum dependence

displays a limiting behaviour for the higher centralities. This is due to the increasing fluctuations and dilution of the matter, which curbs the build up of flow due to increasing eccentricity. The simulated projection seem reasonable due to the reasoning above, thus seen upon as relevant results.

The triangular transverse momentum dependence has lesser dependence on transverse momentum for the lower centralities. This points to the dependence of in plane flow, which also display a limiting behaviour due to a more dilute matter, which transfers the fluctuation to a lesser degree. The triangular flow is thus also seen as reproduced in the transverse momentum space, including the projections of hadronization.

The integrated elliptic and triangular flow displays high levels of accuracy for the all inclusive $1 < p_T < 2$ GeV regime and also for the $2 < p_T < 3$ GeV regime. Integration over the entire transverse momentum regime displays minor deviations. These deviations are due to differences between the simulated and experimental transverse momentum spectra in the softest parts, i.e. $0.5 < p_T$ GeV, which may stem from the implemented decay criteria. The integrated elliptic flow displays a monotonically increasing, hydrodynamic behaviour for the low transverse momentum regime, due to pressure gradients in the initial distribution. The centrality dependence points to the fact stated above regarding the direction of the pressure gradients, thus producing increasing flow for higher centralities. The decays are also seen to lower the flow to a minor extent[138, 139, 140, 141] due to additional scattering.

A more quenched behaviour is found for the high p_T regime, due to fragmentation, which will scatter the media, thus lowering the coherence of the particle distribution. The higher p_T regime displays higher flow due to higher pressure gradients in the initial distribution. When comparing the two transverse momentum regimes, the governing particle production mode is seen to lean more towards hydrodynamics in the low momentum regime. However, due to higher transverse momentum, the particles are more in-plane distributed, thus producing higher all inclusive flow.

The triangular flow displays a lower dependence on centrality due to the fluctuative dependence. The triangular flow is increasing for the higher transverse momentum regime of fragmentation. Fragmentation is making the matter fluctuate, thus elevating the flow. The triangular flow is also displaying dependence on the in-plane coherence to a lower extent than the elliptic flow. Thus, the pressure gradients do play a part in evolving the initial fluctuations.

The pentagonal flow is also integrated and displays a lower dependence on centrality, and a rising dependence for lower levels of ellipticity. This integration may serve as an validation of the pentagonal plane.

The simulations for elliptic, triangular and pentagonal flow are thus considered of high relevance within the relevant regimes. The simulations of the projected modes are viewed as relevant due to the reproduction of all in-

clusive flow, and use of accepted theoretical concepts when modelling the particle genesis. The particle production projections seem trustworthy and the simulations are in line with theoretical predictions. The particle fluctuations is not implemented in present model. Present fluctuations are only in the particle production phase and also in the implementation of the event planes. This will, in spite of almost perfect accuracy when the elliptic and triangular flows are compared to data, likely reveal itself for second order simulations. This makes present author conclude that the elliptic, triangular and pentagonal flows are reproduced and is also to some degree relevant to higher order. The degree of relevance should logically be in the $v_2 - v_5$ harmonic regime, thus diminishing outside this regime.

The elliptic flow for identified particles was investigated for centralities in a constituent quark number scaling model. The simulated flow fulfils quark number scaling to a high degree and display a high degree of accuracy when compared to experimental data [121, 67]. The flow is reproduced to a high degree for the $p_T \leq 3.5$ GeV regime and also for the centralities $0-50\%$. The protons display a lesser degree of precision than pions when compared to data. This is likely due to the specifics of the implementation of decays and also due to thermal rescattering in the late stages of the collision [39, 40, 41].

The decay scattering for identified particles, is here seen to provide a lowering of the particle coherence, when comparing the hydro dynamical flow with the hydro dynamical flow without decays. In particular, the lighter mesons are heavily affected by the decays, thus fulfilling constituent quark number scaling due to resonance decays [153, 134]. The decays are coupled with the coherence production of pion coalescence, thus leading to the observation of confinement [142, 88]. This decay scattering differentiates the light mesons from the heavier baryons in the coalescence model, likely due to the differentiated dynamics of hadronization. The investigation of the hydro dynamical projection of the elliptic flow reveals the expected in-plane flow, due to the driving pressure gradients in the initial conditions, thus increasing with centrality. The jets are seen to lose energy while traversing the matter and the rescattering will diminish the flow for higher transverse momentum [129, 130, 62]. The simulations of flow for different particle production modes seem physically sound. The simulation reproduces the theoretical predictions and experimental data, thus displaying a high level of accuracy and relevance for the identified particle flow when compared to experimental data. The upper transverse momentum limit of ($p_T < 3.5$) GeV, for accurate reproduction of the azimuthal anisotropy and transverse momentum spectra for unidentified and identified particles, is mainly due to lack of reliable experimental data, which imposes great difficulties in tuning the model. These projections are revealing the dynamics of hadronization, thus providing means of probing matter.

The transverse momentum spectra for identified particles displays a corresponding high level of precision [132, 149, 136]. The precision is seen for

the low transverse momentum regime, with its thermal behaviour, and also for the higher p_T regime, where the spectra is characterized by power laws. A slight deviation is seen in the proton spectra. This anomaly is hypothesized to be due to late stage scattering, i.e. post freeze out, as mentioned above. Also, the mid transverse momentum regime for kaons and for pions displays a slight overshoot in the simulated spectra. This likely depends on the thermo dynamical freeze out conditions for the individual species. The observed transverse momentum distributions for identified particles are reproduced to a very high level of precision for the $p_T \leq 3.5$ GeV regime and also for centralities, where the particle distribution is reproduced for $(0 - 50\%)$.

The high levels of accuracy of the simulated elliptic and triangular flow is used in order to compose higher order terms [135] of combinations of lower order flows [78, 79, 80]. The higher order flows are examined in terms of factorization and also in terms of particle correlators. The correlators are derived in present thesis and simulated and compared to the hexagonal flow in the second and third event plane, and also compared to the corresponding factorizations. The correlators displays an interesting behaviour, being continuous and specific to the transverse momentum regimes. This implies that the correlators can provide relevant information regarding hadron genesis [146, 147, 148]

$$\langle \cos 2\left(\phi_1 + \phi_2 + \phi_3 - 3\Psi_2\right)\rangle \overset{\text{Factorization}}{\rightarrow} \langle \cos 6(\phi - \Psi_2)\rangle \quad (5.1)$$

$$\langle \cos 3\left(\phi_1 + \phi_2 - 2\Psi_3\right)\rangle \overset{\text{Factorization}}{\rightarrow} \langle \cos 6(\phi - \Psi_3)\rangle \quad (5.2)$$

$$\langle \cos(2\phi_1 + 3\phi_2 - 2\Psi_2 - 3\Psi_3)\rangle \overset{\text{Factorization}}{\rightarrow} \langle \cos(5\phi - 2\Psi_2 + 3\Psi_3)\rangle. \quad (5.3)$$

The correlators (5.1) has specific characteristics [150, 151], thus providing information regarding the particle coherence. The correlators are related in present form, to the event planes. The event planes may be seen as a particle defining a reference plane, thus defining a true multiparticle correlator. In the future, the correlators can be tested with particles obtained from particle detectors. This part of present thesis may serve as an evaluation of the particle correlators versus the higher flow harmonics. The particle correlators displays more coherence dependence than the higher order harmonics, thus being richer in information content. Also, the correlators may represent a more self contained paradigm in investigating the particle distributions. The present infrastructure is not directed toward correlator work, but instead event plane based flow.

The higher order flow is simulated in the elliptic and triangular event plane. The scaling between the higher order flow, e.g. pentagonal and hexagonal, is investigated. The scaling, or factorization is in general closer for hydrodynamic flow, due to the uniform particle production mode, which in turn displays a uniform particle coherence, thus not amplified or filtered

by the higher wave number harmonics. This is again an indication of the coherence dependence of higher order flows. The hydro dynamically produced particles generally displays a higher degree of flow compared to the all inclusive flow. This is due to the production modes, which predominately recombine comoving partons. The observed flow may thus be seen upon as pressure gradient driven, and as such, the hydro dynamically produced particles are distributed around the event plane, not considering fluctuations [145].

The decays are seen to provide scattering and factorization for higher order factorizations. This is due to the higher order wave number of the high harmonics, which in general are jet observables due to their narrower and more "bins", which observes the "jet axes" [144], with their correlated hadrons ,albeit angular more dispersed. Scattering modes, such as decays provide factorization of higher order flows when coupled to coalescence. The scatter is counter weighting the coherence production of coalescence and jets for high wave numbers. The centrality dependence of the ratios support this statement, since the hexagonal flow in the Ψ_2 plane is elevated for higher centralities, thus being amplified by the high wave number coherence producing jets, relative its factorization.

The simulation of higher order flow in the elliptic, triangular and pentagonal plane provides observables for jets, confinement and particle coalescence. The decays is seen to provide factorization for the higher order flows.

The simulation of the particle distributions observed from the relativistic heavy ion collisions at LHC, are reproduced to a high degree for transverse momentum and azimuthal anisotropy. This azimuthal anisotropy is reproduced in terms of elliptic, triangular and pentagonal flow. This, along with the high degree of reproduction of the transverse momentum spectra for all inclusive particles and also identified particles, are providing a solid foundation in the work of simulating relativistic heavy ion collisions. This foundation to be built upon, and the analysis work, may be continued with the addition of the modifications, and also with the implementation of higher order planes in the analysis part.

Simulation of flow for higher centralities will likely be implemented in a different way in future models for higher centralities. This is due to the steepness of the eccentricity parameterization in present model, which prevents a meaningful simulation of centralities higher than $\sim 50\%$. In the future, the implementation of initial conditions will likely be of a non-scalar kind, thus implementing a full scaled simulation of initial conditions, including event-to-event fluctuations [143, 32, 38]. The initial interaction process is of high physical and conceptual interest, making the collision and evolutionary processes of the partonic matter a very relevant topic.

The code would likely be modular, i.e. the temporally associated parts would be preferred to be runnable one by one, or in sequence, of course in a

cluster version. A distributed type of code controlled by a master code might be beneficial and maybe a development in terms of numerical computing.

This would open up new frontiers in the investigations of matter and the phenomena connected to its evolution. E.g. the investigation of realistic initial conditions. Phase transitions and critical phenomena processes could be investigated within the model. Further development of the model would then be necessary, which is in line with the suggestions made above. The findings presented in this thesis is thus encouraging in terms of the results in terms of reproducability, but also due to the new physics revealing itself as the work progresses.

Chapter 6

Conclusions

The last decade has seen major steps in the observations and development of methods in relativistic heavy ion collisions. Important observations regarding phase transition has changed the hadronic gas paradigm of that time to the present quark gluon plasma view. The observations have since then provided a vast amount of information regarding strong interactions and matter genesis. The observations possible are mainly in yield of species and particle azimuth. The particle azimuthal distributions are commonly investigated through the observable "flow", which is the main part of this thesis.

The elliptic and triangular flow has been reproduced with great predictive power in the transverse momentum regime $0 < p_T < 3.5$ GeV. The precision is also high for the centralities simulated $(0 - 50\%)$. In order to achieve this precision, the computer code used has been slightly modified in terms of particle ellipticity and triangularity. The simultaneous tune of the second, third and fifth event plane is then used in further analysis work, examining the anisotropic flow and particle transverse spectra.

The anisotropic flow is composed of several components originating in different event planes. In particular, the different accessible components of hexagonal and pentagonal flow are examined as a combination of lower order flows. The components are seen as terms of a flow expansion of higher order, e.g. pentagonal and hexagonal flows. This expansion is a sum of all combinatoric factors of the specific flow, where the individual terms in the flow expansion along with the associated correlator, which are simulated, are specific terms which are accessible in present model. I.e. the pentagonal flow is expanded in e.g. a term dependent on the second and third event plane, and another term in the same expansion is dependent on the fourth and first event plane. The first term is accessible while the second is not due to the non established first and fourth event planes for the computational model. As expansion terms for the hexagonal and pentagonal flow, the factorizations

$$v_6\{\Psi_3\} = v_3\{\Psi_3\}v_3\{\Psi_3\} \tag{6.1}$$

$$v_6\{\Psi_2\} = v_2\{\Psi_2\}v_2\{\Psi_2\}v_2\{\Psi_2\} \tag{6.2}$$

$$v_5\{2\Psi_2 + 3\Psi_3\} = v_2\{\Psi_2\}v_3\{\Psi_3\}, \tag{6.3}$$

were investigated. The conditions for the factorizations (6.1), (6.2), (6.3) are investigated as correlation functions for two, three and five particles respectively. These correlation functions reveal the conditions for factorizations. Coherence levels were compared and the conditions for the factorization (6.1) was examined as

$$\langle \cos 3\left(\phi_1 + \phi_2 - 2\Psi_3\right)\rangle \overset{\text{Factorization}}{\rightarrow} \langle \cos 6(\phi - \Psi_3)\rangle \tag{6.4}$$

$$\langle \cos 3\left(\phi_1 + \phi_2 - 2\Psi_3\right)\rangle \overset{\text{Factorization}}{\rightarrow} \langle \cos 3(\phi - \Psi_3)\rangle \times \langle \cos 3(\phi - \Psi_3)\rangle. \tag{6.5}$$

The relation (6.4) is only fulfilled for high levels of fluctuations, i.e. the jet regime. The relation (6.1) may thus only be true for the jet regime only. This likely stems from the fact that jets produce an "two particle average", which resembles the "one particle" Ψ_3 hexagonal flow. In comparing the correlator on the left in (6.4) with flow, factorized is for ~ 1 GeV. The corresponding quadratic triangular flow is relatively higher for the fragmentation region. When the correlator in (6.4) is displayed on its own, its displays a quenched behaviour thus peaking at ~ 2.5 GeV, thus displaying an out of plane behaviour.

The hexagonal flow in the triangular plane were also examined and compared to the quadratic triangular flow. The ratio displays a weak scaling for transverse momentum. However, scaling is closer for hydro dynamical particles only, where lower, and same coherence levels are present, thus approximating (6.1). The absence of decays, will make the directly produced particle flow ratio significantly higher than in the case of all inclusive particles. This feature is pointing to a connection between flow wave number and particle decays. The decays make the factorization and event plane flow scale. The wave number is thus connected to the decays of the produced particles and thus the broadening, thus providing better scaling when decays are included.

The factorization (6.2) is investigated. The fulfilment of

$$\langle \cos 2\left(\phi_1 + \phi_2 + \phi_3 - 3\Psi_2\right)\rangle \overset{\text{Factorization}}{\rightarrow} \langle \cos 6(\phi - \Psi_2)\rangle, \tag{6.6}$$

is now under investigation. This gives a three particle relation, with better statistics, which brings the correlator closer to factorization. The scaling is now approximate due to "better" statistics from the three particle correlator. Exact factorization will occur only for high transverse momentum, where mini jets produce the coherence levels needed for exact factorization. Again, the particles originating in hydro dynamical, soft processes display

proportionality. This is due to the coherence, or non-fluctuative behaviour of hydro dynamically produced particles which provides the proportionality, but no exact scaling. The non-proportionality of direct particles is again an observation of the scaling properties of decays coupled to wave numbers.

The correlator (6.6), is examined and in line with the investigation of the flow ratio, the correlation with the elliptic event plane is better both for elliptic and hexagonal flow. The fragmentation or mixed regime is again displaying the best scaling. The correlator on the left hand side of (6.6), displays factorization for the $p_T \sim 1.5$ GeV regime.

Non-linear flow is also investigated. As a term in the flow expansion for the pentagonal flow, the term (6.3), is investigated. The main reason is the accessibility of the flow through the elliptic, triangular and pentagonal event plane, thus including effects from the elliptic and triangular plane. The flow displays an approximate scaling for mid range transverse momentum. For higher transverse momentum, the higher degree of coherence with the $\psi_2 + \Psi_3$ elevates the ratio, due to the nature of the relevant correlator

$$\langle \cos(2\phi_1 + 3\phi_2 - 2\Psi_2 - 3\Psi_3) \rangle \overset{\text{Factorization}}{\rightarrow} \langle \cos(5\phi - 2\Psi_2 - 3\Psi_3) \rangle. \quad (6.7)$$

The ratio of the non-linear flow and corresponding factorization also increases for high transverse momentum due to higher levels of coherence. Lower coherence is produced in hydrodynamics and soft processes. This coherence level is approximatively constant for hydrodynamics, which makes the ratio factorize exactly. The effects of decays are again visible for direct particles. The wave number is again seen coupled to the fluctuations. The associated correlator on the left hand side of (6.7) is also examined. The correlator displays an monotonic behaviour for transverse momentum. In line with the factorization of the nonlinear pentagonal flow, the correlator displays scaling with the flow factorization and the non-linear pentagonal flow. The investigation of the higher order compound flows reveals interesting properties regarding coherence. The three correlators displays fundamentally different behaviour for the transverse momentum regimes. The elliptic correlator displays a complex behaviour depending on both the recombination and fragmentation. The triangular correlator displays a limiting quenching behaviour, thus providing an observable for the mixed particle production regime. The pentagonal correlator mixes the Ψ_2 and the Ψ_3 planes, thus displaying the monotonous transverse momentum behaviour, thus carrying production information.

The constituent quark number scaling is also investigated, using the same model as in the analysis work (HYDJET++). The quark scaling model is investigated in different coalescence models. The anisotropic flow is examined for baryons and mesons, where pions, protons and lambdas are seen to scale to a high degree of precision. The decays are here seen to play

an important part in fulfilment of constituent quark number scaling. The absence of particle decays provides a higher level of coherence, thus elevating the anisotropic flow, this effect is only visible for the lighter hadrons. This behaviour might be considered as an indirect observation of confinement.

The use of the HYDJET++ package has proven valuable in analysis work, but also in the work of extracting physical properties of the produced matter. In specific, the extraction of matter production modes has been proven valuable in the investigation of the heavy ion collisions.

The absence of generation of realistic initial conditions and subsequent evolution of the produced matter is a limitation. The (hydro dynamical) matter is thus parameterized in the model and the produced matter distributions completely lack the features of a realistically produced matter, e.g. including initial and evolutionary fluctuations and physical eccentricity. Given this, the produced distributions *are* relevant, especially in terms of particle decays and hard physics involving multi parton fragmentation. Since the computational weight is shifted towards the fragmentation/decay regime, it seems natural to view the HYDJET++ as a tool for deeper investigations of the fragmentation/decay physics.

It may be fruitful to undertake the task of implementing physical initial conditions and maybe an evolution of the initial conditions. The two tasks are probably necessary to implement at the same time. Implementing the initial conditions would provide additional understanding regarding the chromo dynamics of non thermalized matter and its geometric consequences. This implementation would also provide the initial conditions for the hydro dynamical equation. Implementing physical initial conditions has been problematic in the past. The common Glauber model of the initial conditions is a geometric model with questionable physical relevance, thus not revealing any non trivial physics of the initial state. A more refined approach would be to implement a colour glass condensate based model for the initial conditions. This model would then be a state of the art model which yields the "correct" eccentricity levels, maybe in contrast to previous CGC models, which produced relatively high eccentricities, thus constraining the hydro dynamical evolution in a non natural way. The initial eccentricity is then defining the observed flow from the evolved initial condition. The eccentricity is fluctuating on an event-to-event basis, providing an additional feature visible in the observed distributions.

The hydrodynamics is then evolving the initial state to the final chemical freeze out state and thereafter freezes out the distributions chemical composition. The hydrodynamic phase is thus an interesting field of research. The hydrodynamics involves coalescence, parton scattering and associated energy loss. The hydrodynamic collective variable for some of the most interesting physical processes is the viscosity, which consequences are investigated through the postulated evolution. The hydro dynamical model could then be a viscous hydro model with a common interface so the com-

plete simulation code is modular in its parts. The hadronization part can also be elaborated. The phase transitions linked with the hadronization is of high interest. Critical behaviour and chiral symmetry restoration/breaking are of interest, describing hadron melting/formation. Near fields of interest are confinement and other aspects of quantum chromo dynamics. Post freeze out phenomena such as thermal rescattering are also of interest. A primary goal might then be a physically sound, complete modular model, which produces relevant data in every stage. This model should then be fully extensible and ready for further development, thus moving the understanding of relativistic heavy ion collisions forward.

The analysis work proves valuable and some progress *is* made. Development of the analysis part of the code is in progress and several high quality papers have been produced already. The model performs well and reproduces direct experimental data well, and in addition reproduces indirect observables, at least in a qualitative way. This makes the tuning work important and needs to be done continuously as work progresses. As stated, the implementation of initial conditions may provide a more stable foundation to build upon. The code is easy to work with and serves as a pedagogical tool as well as a data producing machine and is a pleasure to work with and progress is usually made. The work including fragmentation and particle decays is promising and is starting to show some progress and perhaps the decays might be possible to study in an accelerator setting due to the theoretical/computational work in present paper and others. Theoretical work is likely to become a more prominent part of the work as the model improves.

Obtaining experimental data is difficult at best. The data have to be harvested from open web pages and are erratically organised using poor technology at best. The data are often incomplete and relevant published data are missing. This is likely due to the (intentional?) monolithic organizational structures where accountability is dispersed. The common use of open web pages is likely due to this inability to cooperate and lack of professional conduct at the data sources. The data is often of very poor quality and its validity can easily be questioned. Sometimes even the physical relevance of the claimed data is dubious.

Given this, the author realizes and recognizes the process of data acquisition and the limits of the colliders and detectors in use. The data acquisition is dependent on the present collisional models, which in turn are tuned to presumably relevant data. This is a fact of frontline physics and as such a part of contemporary physics. This leads to temporarily conclusion that the precision of the experimental data may not be seen to be of highest relevance at the moment, due to the ladder like process of modern physics. However, consistency *should* likely be prioritized. This would probably provide a better situation when working on the models. Given the performance and potential of present model, it may very well be a part of this ongoing work in understanding and acquiring data out of the signals from collisional

processes in the future.

Bibliography

[1] M. Peplow, Nature **5**, 18 (2005).

[2] M. S. Turner Nature Phys. **4**, 89 (2008).

[3] M. Riordan and W. A. Zajc, Sci. Am. **294**, 34 (2006).

[4] K. Adcox *et al* (PHENIX Collaboration), Phys. Rev. Lett **86**, 3500 (2001).

[5] M. Harrison, S. Peggs and T. Roser, Annu. Rev. Nucl. Part. S. **52**, 425 (2002).

[6] M. Harrision, T Ludlam and S. Ozaki, Nucl. Instrum. Meth. A **499**, 235 (2003).

[7] V. Jamieson, New Sci. **8**, 27 (2008).

[8] G. Brumfiel, Nature **471**, 13 (2011).

[9] E. S. Reich, Nature **503**, 7475 (2013).

[10] J. Y. Ollitrault, Phys. Rev. D **46**, 229 (1992).

[11] S. Voloshin and Y. Zhang, Z. Phys. C **70**, 665 (1996).

[12] A. M. Poskanzer and S. A. Voloshin, Phys. Rev. C **58**, 1671 (1998).

[13] A. Adare *et al.*(PHENIX Collaboration), Phys. Rev. Lett. **98**, 162301 (2007).

[14] M. Gutlassy, I. Vitev and X.-N. Wang, Phys. Rev. Lett. **86**, 2537 (2001).

[15] S. Z. Belenkji and L. D. Landau, Nuovo Cimento Suppl. **3**, 15 (1956).

[16] M. Luzum and P. Romatschke, Phys. Rev. C **78**, 034915 (2008).

[17] K. Dusling, G. Moore and D. Teaney, Phys. Rev. C **81**, 034907 (2010).

[18] D. Teaney and L. Yan, arXiv:1010.1876v1.

[19] S. Ryu, S. Jeon, C. Gale, B. Schenke and C. Young, Nucl. Phys. A **904**, 389 (2013).

[20] Iu. Karpenko, P. Houvinen and M. Bleicher, Comp. Phys. Comm. **185**, 3016 (2014).

[21] C. Shun, Z. Qiu, H. Song, J. Bernhard, S. Bass and U. Heinz, arXiv:1409.8164v2.

[22] J. D. Bjorken, Phys. Rev. D **27**, 140 (1983).

[23] Y. Hatta, J. Norhona and B.-W. Xiao, Phys. Rev. D **89**, 051702 (2014).

[24] H. Marrochio, J. Noronha, G. S. Denicol, M. Luzum, S. Jeon and C. Gale, Phys. Rev. C **91**, 014903 (2015).

[25] R. J. Glauber, Phys. Rev. **100**, 242 (1955).

[26] R. J. Glauber and G. Matthiae, Nucl. Phys. B **21**, 135 (1970).

[27] P. Shukla, Phys. Rev. C **67**, 054607 (2003).

[28] M. L. Miller, K. Reygers, S. J. Sanders and P. Steinberg, Annu. Rev. Nucl. Part. S. **57**, 205 (2007).

[29] T. Hirano, U. Heinz, D. Kharzeev, R. Lacey and Y. Nara, J. Phys. G Nucl. Partic.**34**, S879 (2007).

[30] F. Gelis, E. Iancu, J. Jalilian-Marian and Raju Venugopalan, Annu. Rev. Nucl. Part. S. **60**, 463 (2010).

[31] J. Albacete, A. Dumitru and Y. Nara, J. Phys. Conf. Ser. **316**, 012011 (2011).

[32] B. Schenke, P. Tribedy and R. Venugopalan, Phys. Rev. Lett. **108**, 252301 (2012).

[33] I. Arsene *et al.* (BRAHMS Collaboration), Nucl. Phys. A **757**, 1 (2005).

[34] T. Hirano and Y. Nara, Phys. Rev. C **79**, 064904 (2009).

[35] R. Bhalerao, M. Luzum and J.-Y. Ollitrault, Phys. Rev. C **84**, 054901 (2011).

[36] A. Krasnitz and R. Venugopalan, Phys. Rev. Lett. **84**, 4309 (2000).

[37] T. Lappi and L. McLerran, Nucl. Phys. A **772**, 200 (2006).

[38] L. McLerran, Nucl. Phys. A **926**, 3 (2014).

[39] Iu. A. Karpenko, Yu. M. Sinyukov and K. Werner, Phys. Rev. C **87**, 024914 (2013).

[40] Y. Pan and S. Pratt, Phys. Rev. C **89**, 044911 (2014).

[41] F. Beccatini *et al.*, arXiv:1405.0710v3.

[42] S. S. Adler *et al* (PHENIX Collaboration), Phys. Rev. Lett **91**, 182301 (2003)

[43] A. Adare *et al* (PHENIX Collaboration), Phys. Rev. Lett **105**, 142301 (2010)

[44] A. Adare *et al* (PHENIX Collaboration), Phys. Rev. Lett **107**, 252301 (2011)

[45] A. Adare *et al.* (PHENIX Collaboration), Phys. Rev. C **85**, 064914 (2012).

[46] K. Aamodt *et al.* (ALICE Collaboration), Phys. Rev. Lett. **105**, 252302 (2010).

[47] K. Aamodt *et al.* (ALICE Collaboration), Phys. Rev. Lett. **107**, 032301 (2011).

[48] G. Aad *et al.* (ATLAS Collaboration), Phys. Rev. C **86**, 014907 (2012).

[49] B. Abelev *et al.* (ALICE Collaboration), arXiv:1208.2711v2.

[50] J. Barrette *et al*, Phys. Rev. Lett **73**, 2532 (1994)

[51] J. Barrette *et al*, Phys. Rev. C **55**, 1420 (1997)

[52] J. Barrette *et al*, Phys. Rev. C **56**, 3254 (1997)

[53] H. Appelshuser *et al* (NA49 Collaboration), Phys. Rev. Lett **80**, 4136 (1998).

[54] A. M. Poskanzer *et al* (NA49 Collaboration), Nucl. Phys. A **661**, 341c (1999).

[55] B. B. Back *et al.* (PHOBOS Collaboration), Nucl. Phys. A **757**, 28 (2005).

[56] J. Adams *et al.* (STAR Collaboration), Phys. Rev. C **72**, 014904 (2005).

[57] K. Adcox *et al.* (PHENIX Collaboration), Nucl. Phys. A **757**, 184 (2005).

[58] E. Shuryak, Progr. Part. Phys. **62**, 48 (2009).

[59] E. L. Bratovskaya, V. P. Konchakovski, V. Voronyuk, V. D. Toneev, O. Linnyk and W. Cassing, arXiv:1202.4891v1.

[60] B. Abelev *et al.* (ALICE Collaboration), arXiv:1208.2711v2.

[61] B. Abelev *et al.* (ALICE Collaboration), Phys. Lett. B **736**, 196 (2014).

[62] S. Chatrchyan *et al.* (CMS Collaboration), Eur. Phys. J. C **74**, 2847 (2014).

[63] P. Bożek, Phys. Rev. C **85**, 034901 (2012).

[64] L. V. Bravina, B. H. Brusheim Johansson, G. Kh. Eyyubova, V. L. Korotkikh, I. P. Lokhtin, L. V. Malinina, S. V. Perushanko, A. M. Snigirev and E. E. Zabrodin, Eur. Phys. J. C **74**, 2807 (2014).

[65] M. Habich, J. L. Nagle and P. Romatschke, Eur. Phys. J. C **75**, 15 (2014).

[66] G. Aad *et al.* (ATLAS Collaboration), arXiv:1405.3936v2.

[67] F. Noferini *et al.* (ALICE Collaboration), Nucl. Phys. A **904**, 483c (2013).

[68] G. Aad *et al.* (ATLAS Collaboration), arXiv:1403.0489v2.

[69] I. P. Lokhtin, L. V. Malinina, S. V. Petrushanko, A. M. Snigirev, I. Arsene and K. Tywoniuk, Comp. Phys. Comm. **180**, 779 (2009).

[70] L. Euler, Acad. Sci. Berllin **11** (1755).

[71] J. Beringer *et al*, Phys. Rev. D **86**, 010001 (2011).

[72] S. Afanasiev *et al.* (PHENIX Collaboration), Phys. Rev. C **80**, 024909 (2009).

[73] B. Schenke, S. Jeon and C. Gale, Phys. Rev. C **82**, 014903 (2010).

[74] M. Miller and R. Snellings, arXiv:nucl-ex/0312008v2.

[75] F. G. Gardim, F. Grassi, M. Luzum and J.-Y. Ollitrault, Phys. Rev. C **85**, 024908 (2012).

[76] B. Schenke, P. Tribedy and Raju Venugopalan, Phys. Rev. C **86**, 034908 (2012).

[77] L. Yan , J.-Y. Ollitrault and A. M. Poskanzer, Phys. Rev. C **90**, 024903 (2014).

[78] D. Teaney and L. Yan, Phys. Rev. C **83**, 064904 (2011).

[79] D. Teaney and L. Yan, arXiv:1312.3689v2.

[80] D. Teaney and L. Yan, Phys. Rev. C **86**, 044908 (2012).

[81] F. E. Close, *An Introduction to Quarks and Partons* (academic, London, 1979)

[82] W. Greiner, S. Schramm and E. Stein, *Quantum Chromodynamics* (Springer, Berlin, 2007)

[83] T. Muta, *Foundations of Quantum Chromodynamics* (World Scientific Publishing, Singapore, 2010), p.10.

[84] F. Mandl and G. Shaw, *Quantum Field Theory* (Wiley, Chichester, 2010)

[85] R. Devendish, A. Cooper-Sarkar *Deep Inelastic Scattering* (Oxford, Oxford, 2004)

[86] G. Altarelli, Phys. Rep. **81**, 1 (1982).

[87] C. Bachas, Phys. Rev. D **33**, 2723 (1986).

[88] J. Greensite, *An Introduction to the Confinement Problem*(Springer, Heidelberg, 2011).

[89] P. Kolb, J. Sollfrank and U. Heinz, Phys. Rev. C **62**, 054909 (2000).

[90] T. Hirano, Phys. Rev C **65**, 011901 (2001).

[91] Iu. Karpenko and Yu. M. Sinyukov **81**, 054903 (2010).

[92] B. Schenke, S. Jeon and C. Gale, Phys. Rev. Lett. **106**, 042301 (2011).

[93] C. Gale, S. Jeong and B. Schenke arXiv:1301.5893v1.

[94] P. Kolb, U. Heinz, P Houvinen, K. J. Eskola and K. Touminen, Nucl. Phys. A **696**, 197 (2001).

[95] H. deVries, C. W. deJager and C. deVries, Atomic Data and Nuclear Data Tables **36**, 495 (1987).

[96] R. Vogt, *Ultrarelativistic Heavy-Ion Collisions*(EElsevier, Amsterdam, 2007).

[97] L. P. Csernai, *Introduction to Relativistic Heavy Ion Collisions*(Wiley, Chichester, 1994).

[98] R. Baier, JHEP **0408**, 100 (2008).

[99] P. Bożek and I. Wyskiel-Piekarska, Phys. Rav. C **85**, 064915 (2012).

[100] C. Gale, S. Jeon, P. Tribedy and R. Venugopalan, Phys. Rev. Lett **110**, 012302 (2013).

[101] M. Luzum, J. Phys. Conf. Ser. **446**, 012020 (2013).

[102] U. Heinz and R. Snellings, arXiv:nucl-th/1301.2826v1.

[103] F. Cooper and G. Frye, Phys. Rev. D **10**, 186 (1974).

[104] S. V. Akkelin, P. Braun-Munzinger and Yu. M. Sinyukov Nucl. Phys. A **710**, 439 (2002).

[105] R. Baier, Yu. L. Dokshitzer, A. H. Mueller and D. Schiff, Nucl. Phys. B **484**, 265 (1996).

[106] R. Baier, Yu. L. Dokshitzer, A. H. Mueller, S. Peigne and D. Schiff, Nucl. Phys. B **483**, 291 (1997).

[107] R. Baier, Yu. L. Dokshitzer, A. H. Mueller, S. Peigne and D. Schiff, Nucl. Phys. B **531**, 403 (1998).

[108] R. Baier, Yu. L. Dokshitzer, A. H. Mueller and D. Schiff, Phys. Rev. C **60**, 064902 (1999).

[109] R. Baier, Yu. L. Dokshitzer, A. H. Mueller and D. Schiff, Phys. Rev. C **64**, 057902 (2001).

[110] N. S. Amelin, R. Lednicky, T. A. Pocheptsov, I. P. Lokhtin, L. V. Malinina, A. M. Snigirev, Iu. A. Karpenko and Yu. M. Sinyukov, Phys. Rev. C **74**, 064901 (2006).

[111] N. S. Amelin, R. Lednicky, I. P. Lokhtin, L. V. Malinina, A. M. Snigirev, Iu. A. Karpenko and Yu. M. Sinyukov, I. Arsene and L. Bravina, Phys. Rev. C **77**, 014903 (2008).

[112] C. Cleymans, H. Oeschler, K. Redlich and S. Wheaton, Phys. Rev. C **73**, 034905 (2006).

[113] G. Torieri, S. Steinke, W. Broniowski, W. Florkowski, J. Letessier and J. Rafelski, Comp. Phys. Comm. **167**, 229 (2005).

[114] T. Sjostrand, S. Mrenna and P. Skands, arXiv:0603175v2.

[115] R. Brun and F. Rademakers, Nucl. Instrum. Meth. A **389**, 81 (1997).

[116] D. Kharzeev, E. Levin and M. Nardi, Nucl. Phys. A **747**, 609 (2005).

[117] D. Molnar and S. Voloshin, Phys. Rev. Lett. **91**, 092301 (2003).

[118] V. Greco ,C. M. Ko and P. Levai, Phys. Rev. C **68**, 034904 (2003).

[119] P. Kolb, L.-W. Chen, V. Greco and C. M. Ko, Phys. Rev. C **69**, 051901 (2004).

[120] R. J. Fries, J. Phys. G Nucl. Partic. **30**, S853 (2004).

[121] M. Krezewicki, J. Phys. G Nucl. Partic. **38**, 124047 (2011).

[122] A. Adare *et al.* (PHENIX Collaboration), arXiv:1412.1038v1.

[123] J. C. Collins and D. E. Soper, Nul. Phys. B **194**, 445 (1982).

[124] B. A. Kniehl, G. Kramer and B. Pötter. Collins and D. E. Soper, Nucl. Phys. B **194**, 445 (1982).

[125] J. D. Bjorken , FERMILAB-Pub-82/59-THY (1982).

[126] E. Braaten, M. H. Thoma, Phys. Rev. **44**, 1298 (1991).

[127] I. P. Lokhtin and A. M. Snigirev, Eur. Phys. J **16**, 527 (2000).

[128] G. Y. Qin, J. Ruppert, C. Gale, S. Jeon, G. D. Moore and M. G. Mustafa, Indian J. Phys. **85**, 873 (2011).

[129] K. Aamodt *et al.* (ALICE Collaboration), Phys. Lett. B **696**, 30 (2011).

[130] S. Chatrchyan *et al.* (CMS Collaboration), arXiv:1202.2554v2.

[131] G. Aad *et al.* (ATLAS Collaboration), arXiv:1411.2357v1.

[132] B. Abelev *et al.* (ALICE Collaboration), arXiv:1208.2711v2.

[133] S. Chatrchyan *et al.* (CMS Collaboration), Phys. Rev. C **87**, 014902 (2013).

[134] L. Bravina, B. H. Brusheim Johansson, B. Eyyubova and E. Zabrodin, Phys. Rev. C **87**, 034901 (2013).

[135] L. Bravina *et al.*, Phys. Rev. C **89**, 024909 (2014).

[136] B. Abelev *et al.* (ALICE Collaboration), Phys. Rev. C **88**, 044910 (2013).

[137] G. Aad *et al.* (ATLAS Collaboration), Eur. Phys. J **74**, 2982 (2014).

[138] P. F. Kolb, J. Sollfrank and U. Heinz, Phys. Lett. B **459**, 667 (1999).

[139] P. F. Kolb, J. Sollfrank and U. Heinz, Phys. Rev. C **62**, 054909 (2000).

[140] Z. Qiu, C. Shen and U. Heinz, arXiv:1210.7010v1.

[141] T. Hirano, arXiv:nucl-th/0004029v2.

[142] G. V. Efimov and M. A. Ivanov, *The Quark Confinement Model of Hadrons*(IOP, Bristol, 1993).

[143] T. Hirano, U. Heinz, D. Karzeev, R. Lacey and Y. Nara, J. Phys. G Nucl. Part. Phys. **34**, S879 (2007).

[144] A. Accardi *et al.*, arXiv:hep-ph/0310274v1.

[145] J.-Y. Ollitrault, Eur. J. Phys. **29**, 275 (2008).

[146] C. Gupta, R. K. Shivpuri, N. S. Verma and A. P. Sharma, Nouvo Cim. A **75**, 408 (1983).

[147] J. F. Owens, Rev. Mod. Phys. **59**, 465 (1987).

[148] R. J. Fries, B. Müller, C. Nonaka and S. A. Bass, Phys. Rev. Lett. **90**, 202303 (2003).

[149] B. Abelev *et al.* (ALICE Collaboration), Phys. Rev. Lett. **88**, 044909 (2013).

[150] B. Abelev *et al.* (STAR Collaboration), Phys. Rev. C **81**, 054908 (2010).

[151] I. Selyuzenkov, J. Phys. Conf. Ser. **426**, 012002 (2010).

[152] E. Zabrodin, L. Bravina, B. H. Brusheim Johansson and G. Eyyubova, Eur. J Phys. Conf. Ser. **70**, 00010 (2014).

[153] L. Bravina, B. H. Brusheim Johansson, Gyulnara Eyyubova and Evgeny Zabrodin, PoS ConfinementX, 169 (2012).

Appendixes

.1 Effect of jets on v_4/v_2^2 ratio and constituent quark scaling in relativistic heavy-ion collisions

Effect of jets on v_4/v_2^2 ratio and constituent quark scaling in relativistic heavy-ion collisions

L. Bravina,[1] B.H. Brusheim Johansson,[1] G. Eyyubova,[1,*] and E. Zabrodin[1,*]

[1] *Department of Physics, University of Oslo, PB 1048 Blindern, N-0316 Oslo, Norway*

(Dated: February 26, 2015)

The Monte Carlo HYDJET++ model, that combines parametrized hydrodynamics with jets, is employed to study formation of second v_2 and fourth v_4 components of the anisotropic flow in ultrarelativistic heavy-ion collisions at energies of the Relativistic Heavy Ion Collider (RHIC) and the Large Hadron Collider (LHC), $\sqrt{s} = 200A$ GeV and $\sqrt{s} = 2.76A$ TeV, respectively. It is shown that the quenched jets contribute to the soft part of the $v_2(p_T)$ and $v_4(p_T)$ spectra. The jets increase the ratio v_4/v_2^2 thus leading to deviations of the ratio from the value of 0.5 predicted by the ideal hydrodynamics. Together with the event-by-event fluctuations, the influence of jets can explain quantitatively the ratio v_4/v_2^2 at $p_T \leq 2\,\mathrm{GeV}/c$ for both energies and qualitatively the rise of its high-p_T tail at LHC. Jets are also responsible for violation of the number-of-constituent-quark (NCQ) scaling at LHC despite the fact that the scaling is fulfilled for the hydro- part of particle spectra.

PACS numbers: 25.75.-q, 25.75.Ld, 24.10.Nz, 25.75.Bh

I. INTRODUCTION

The transverse collective flow of particles is an important characteristic of ultrarelativistic heavy-ion collisions because the flow is able to carry information about the early stage of the reaction. Particularly, the collective flow is very sensitive to change of the equation of state (EOS), e.g., during the quark-hadron phase transition. The azimuthal distribution of particles can be cast [1, 2] in the form of Fourier series

$$E\frac{d^3N}{d^3p} = \frac{1}{\pi}\frac{d^2N}{dp_t^2 dy}\left[1 + \sum_{n=1}^{\infty} 2v_n \cos(n\phi)\right]. \qquad (1)$$

Here ϕ, p_t, and y are the azimuthal angle, the transverse momentum, and the rapidity of a particle, respectively. The unity in the parentheses represents the isotropic radial flow, whereas the sum of harmonics refers to anisotropic flow. The first two harmonics of the anisotropic flow, dubbed directed flow v_1 and elliptic flow v_2, have been extensively studied both experimentally and theoretically in the last 15 years (see, e.g., [3] and references therein), while the systematic study of higher harmonics began quite recently [4–7].

In the present paper we investigate the ratio $R = v_4/v_2^2$ in heavy-ion collisions at energies of the Relativistic Heavy Ion Collider (RHIC) ($\sqrt{s} = 200A$ GeV) and the Large Hadron Collider (LHC) ($\sqrt{s} = 2.76A$ TeV). Interest in the study was raised due to the obvious discrepancy between the theoretical estimates and the experimental measurements. On the one hand, the exact theoretical result for hydrodynamics provided $v_4/v_2^2 = 0.5$ for a thermal freeze-out distribution [8]. On the other hand, it was found soon in RHIC experiments [9, 10] that the measured ratio R exceeded by factor 2 the theoretically predicted one. Both the STAR and the PHENIX Collaborations have reported that the R is rather close to unity for all identified particles in a broad ranges of centrality, $10\% \leq \sigma/\sigma_{geo} \leq 70\%$, and transverse momentum, $p_T \geq 0.5\,\mathrm{GeV}/c$. For the smaller p_T the ratio seems to exceed the value of 1. Note also that the PHENIX data are about 10−15% below the STAR ones.

In Ref. [11] it was argued that the experimentally measured R can be larger than 0.5 even if the ratio v_4/v_2^2 was exactly equal to 0.5 in each event. Such a distortion can be caused by event-by-event fluctuations. Namely, if the ratio v_4/v_2^2 is estimated not on an event-by-event basis but rather on averaging of both v_2 and v_4 over the whole statistics, the event-by-event fluctuations will significantly increase the extracted value of the ratio. Calculations of R at RHIC energies within both ideal and viscous hydrodynamics with different initial conditions [12] revealed that the ideal hydrodynamics provided better agreement with the data, although the STAR results remained underpredicted a bit. For LHC the hydrodynamic calculations have predicted similar behavior with slight increase at small transverse momenta [12].

The preliminary results obtained in Pb + Pb collisions at $\sqrt{s} = 2.76A$ TeV favor further increase of the v_4/v_2^2 ratio [5, 6]. Moreover, this ratio is not a constant at $p_T \geq 0.5\,\mathrm{GeV}/c$ but increases with rising transverse momentum. The first aim of the present paper is to study to what extent the hard processes, i.e., jets, can affect the ratio R predicted by the hydrodynamic calculations.

The second aim of the paper is investigation of the fulfillment of the so-called number-of-constituent-quark (NCQ) scaling, observed initially for the partial elliptic of mesons and baryons at RHIC [13, 14]. Despite the general expectations, the measurements show that the NCQ scaling is broken at LHC energies [15]. Thus, it would

*Also at Skobeltsyn Institute of Nuclear Physics, Moscow State University, RU-119991 Moscow, Russia

be interesting to elucidate the role of jets in the scaling violation. For these purposes we employ the HYDJET++ model [16], which couples the parametrized hydrodynamics to jets. The soft part of the HYDJET++ simulated event represents the thermalized hadronic state where particle multiplicities are determined under assumption of thermal equilibrium. Hadrons are produced on the hypersurface, represented by a parametrization of relativistic hydrodynamics with given freeze-out conditions. At the freeze-out stage the system breaks up into hadrons and their resonances. The table of baryon and meson resonances implemented in the model is quite extensive. This allows for better accounting of the influence of final-state interactions on the generated spectra. The hard part of the model accounts for jet quenching effect, i.e., radiation and collisional losses of partons traversing hot and dense media. The contribution of soft and hard processes to the total multiplicity of secondaries depends on both centrality of the collision and its energy and is tuned by model parameters to RHIC and LHC data.

The paper is organized as follows. A brief description of the HYDJET++ is given in Sec. II. Section III presents the results of calculations of both v_2 and v_4 for charged particles in both considered reactions. The even components of the anisotropic flow and their ratio $R = v_4/v_2^2$ are studied in the interval $10\% \leq \sigma/\sigma_{geo} \leq 50\%$ in four centrality bins. In Sec. IV the interplay between jets and decays of resonances, as well as the roles of resonance decays in better realization and the jets in violation of the number-of-constituent-quark scaling are discussed. Conclusions are drawn in Sec. V.

II. THE HYDJET++ EVENT GENERATOR

The Monte Carlo event generator HYDJET++ [16] was developed for fast but realistic simulation of hadron spectra in both central and non-central heavy-ion collisions at ultrarelativistic energies. It consists of two parts. The FASTMC [17, 18] event generator deals with the hydrodynamic evolution of the fireball. Therefore, it describes the soft parts of particle spectra with the transverse momenta $p_T \leq 2\,\mathrm{GeV}/c$. The hard processes are simulated by the HYDJET model [19] that propagates jets through hot and dense partonic medium. Both parts of the HYDJET++ generate particles independently.

To allow for really fast generation of the spectra the FASTMC employs a parametrized hydrodynamics with Bjorken-like or Hubble-like freeze-out surface parametrization. Since at ultrarelativistic energies the particle densities at the stage of chemical freeze-out are quite high, a separation of the chemical and thermal freeze-out is also implemented. The mean number of participating nucleons N_{part} at a given impact parameter b is calculated from the Glauber model of independent inelastic nucleon-nucleon collisions. After that the value of effective volume of the fireball V_{eff}, that is directly proportional to N_{part}, is generated. When the effective volume of the source is known, the mean multiplicity of secondaries produced at the spacelike freeze-out hypersurface is calculated. Parametrizations of the odd harmonics of the anisotropic flow are not implemented in the present version of HYDJET++, whereas the elliptic flow is generated by means of the hydro-inspired parametrization that depends on momentum and spatial anisotropy of the emitting source. The model utilizes a very extensive table of ca. 360 baryon and meson resonances and their antistates together with the decay modes and branching ratios taken from the SHARE particle decay table [20]. After the proper tuning of the free parameters, the HYDJET++ simultaneously reproduces the main characteristics of heavy-ion collisions at RHIC and at LHC, such as hadron spectra and ratios, radial and elliptic flow, and femtoscopic momentum correlations.

The multiple scattering of hard partons in the quark-gluon plasma (QGP) is generated by means of the HYDJET model. This approach takes into account accumulating energy loss, the gluon radiation, and collisional loss, experienced by a parton traversing the QGP. The shadowing effect [21] is implemented in the model as well. The PYQUEN routine [22] generates a single hard NN collision. The simulation procedure includes the generation of the initial parton spectra with PYTHIA [23] and production vertexes at a given impact parameter, rescattering-by-rescattering simulation of the parton path length in a dense medium, radiative and collisional energy losses, and final hadronization for hard partons and in-medium emitted gluons according to the Lund string model [24]. Then, the full hard part of the event includes PYQUEN multi-jets generated around its mean value according to the binomial distribution. The mean number of jets produced in $A + A$ events is a product of the number of binary NN sub-collisions at a given impact parameter and the integral cross section of the hard process in NN collisions with the minimal transverse momentum transfer, $p_T^{\min}$. Further details of the model can be found in Refs. [16–19].

It is worth mentioning recent important modification of the HYDJET++. After the measurement of particle spectra in pp collisions at LHC it became clear that the set of model parameters employed by the PYTHIA 6.4 version had to be tuned. Several modifications have been proposed [25, 26]. The application of standard PYTHIA 6.4 in the HYDJET++ led to too early suppression of elliptic flow of charged particles at intermediate transverse momenta in lead-lead collisions and, therefore, to the prediction of a weaker v_2 [27, 28] compared to the data. Recently, the HYDJET++ was modified [29] to implement the Pro-Q20 tune of PYTHIA. In contrast to calculations of elliptic flow presented in [27, 28, 30], all simulations of Pb + Pb reactions at LHC energies in the present paper are performed with the upgraded HYDJET++.

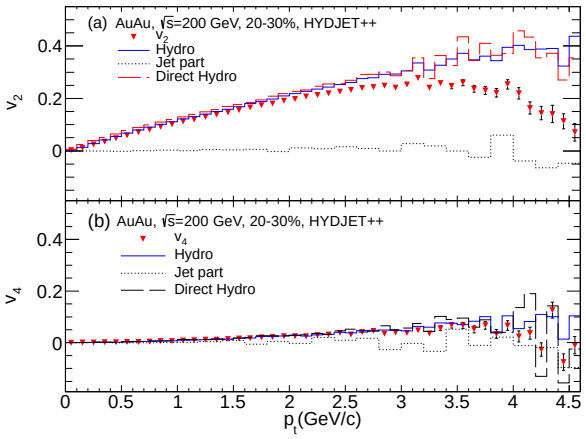

FIG. 1: (Color online) Transverse momentum dependencies (triangles) of (a) v_2 and (b) v_4 of charged hadrons calculated within the HYDJET++ for Au + Au collisions at $\sqrt{s} = 200A$ GeV at centrality $\sigma/\sigma_{\rm geo} = 20-30\%$. Histograms show flow of directly produced particles in hydro-calculations (dashed lines), total hydrodynamic flow (solid lines), and flow produced by jets (dotted lines).

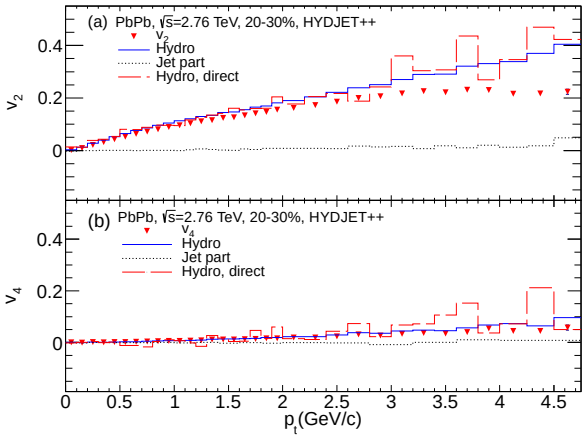

FIG. 2: (Color online) The same as Fig. 1 but for Pb + Pb collisions at $\sqrt{s} = 2.76A$ GeV.

III. v_2 AND v_4 FROM HYDRODYNAMICS AND FROM JETS

For the investigations of the second and the fourth flow harmonics, ca. 60 000 gold-gold and ca. 50 000 lead-lead minimum bias collisions have been generated at $\sqrt{s} = 200A$ GeV and $\sqrt{s} = 2.76A$ TeV, respectively. The transverse momentum dependencies of v_2 and v_4 obtained for the centralities 20−30% are shown in Fig. 1 for RHIC and in Fig. 2 for LHC energies.

Together with the resulting distributions for $v_2(p_T)$ and $v_4(p_T)$ we present separate contributions coming from (i) hadrons directly produced at the freeze-out hypersurface in the hydrodynamic part, (ii) direct and secondary hadrons created after the decays of resonances, and (iii) hadrons produced in the course of jet fragmentation. Recall briefly the main features of the $v_2(p_T)$ behavior in HYDJET++. The elliptic flow rises up to its maximum at intermediate p_T around 2.5−3 GeV/c and then rapidly drops. This falloff is observed in experimental data also. In the model its origin is traced to the interplay between the soft hydrolike processes and hard jets, as was studied in details in [27, 28]. The ideal hydrodynamics demonstrates continuous increase of the elliptic flow with rising transverse momentum. Because of the jet quenching the jets also develop an asimuthal anisotropy that increases with the p_T too; however, this effect is quite weak and does not exceed few percent. The particle yield as a function of the transverse momentum drops more rapidly for hydroproduced hadrons than for hadrons from jets. Therefore, after a certain p_T threshold jet particles start to dominate the particle spectrum, thus leading to a weakening of the combined elliptic flow. A similar tendency is observed in Fig. 1 and Fig. 2 for the v_4 also, but, because of the quite weak signal in the hydrodynamic part, the effect of the v_4 falloff is not as pronounced as that of the elliptic flow.

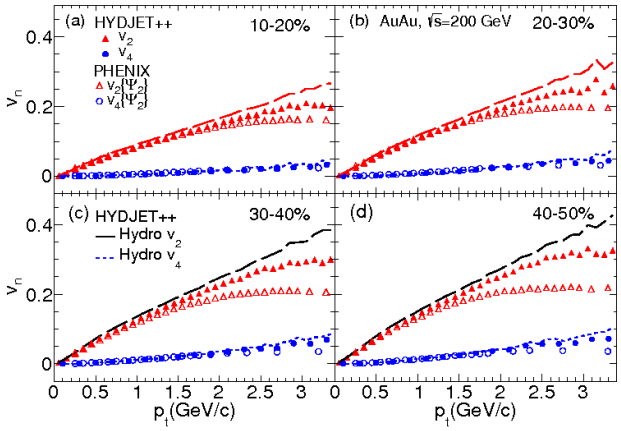

FIG. 3: (Color online) $v_2(p_T)$ (full triangles) and $v_4(p_T)$ (full circles) for charged particles in HYDJET++ calculations of Au + Au collisions at $\sqrt{s} = 200A$ GeV at centrality $\sigma/\sigma_{\rm geo}$ (a) 10−−20%, (b) 20−−30%, (c) 30−−40% and (d) 40−−50%, respectively. Dashed lines show hydrodynamic part of the calculations. Data from [10] are shown by open triangles (v_2) and open squares (v_4).

As shown in Fig. 1 decays of resonances can change the elliptic flow of directly produced hadrons with $p_T \leq 3$ GeV/c by 1−2% at RHIC and by less than 1% at LHC; see Fig. 2. For the v_4 the difference between the two histograms is negligible; i.e., resonance decays play a minor role for soft parts of both $v_2(p_T)$ and $v_4(p_T)$ distributions. At $p_T \approx 2.5$ GeV/c jets come into play and change dramatically the shapes of the elliptic and hexadecapole flows.

It is worth discussing here details concerning the determination of the flow components in the experiment

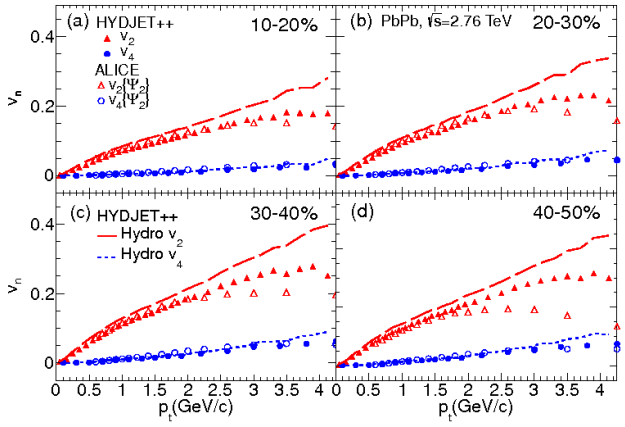

FIG. 4: (Color online) The same as Fig.3 but for Pb + Pb collisions at $\sqrt{s} = 2.76A$ GeV. Experimental data are taken from [31].

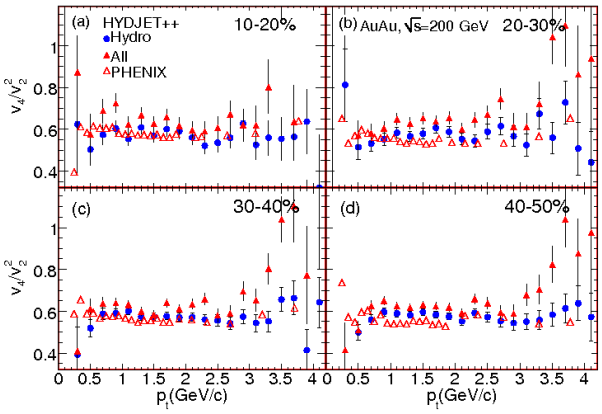

FIG. 5: (Color online) Ratio $v_4/(v_2)^2$ vs. p_T for charged particles in HYDJET++ calculations of Au + Au collisions at $\sqrt{s} = 200A$ GeV at centrality $\sigma/\sigma_{\rm geo}$ (a) $10 - -20\%$, (b) $20 - -30\%$, (c) $30 - -40\%$ and (d) $40 - -50\%$, respectively. Full circles denote the hydro+jet calculations, open circles show only hydro-part, and open squares indicate the rescaled experimental data (see text for details).

and in the model. In the HYDJET++ simulations the elliptic flow is connected to the eccentricity of overlapped volume of colliding nuclei. No fluctuations in the location of nucleons within the overlapped zone are considered. Therefore, the flow is determined with respect to the position of true reaction plane. The next even component, v_4, is not parametrized in the present version of the model; i.e., the hexadecapole flow comes out here merely due to the elliptic flow. Thus, it should also be settled by the position of the true reaction plane. Because of the absence of the fluctuations and non-flow effects, the ratio v_4/v_2^2 obtained on an event-by-event basis equals that extracted by separate averaging of v_4 and v_2 over the whole simulated statistics.

In the experiment the situation is more complex. For instance, in the standard event plane (EP) method the event flow vector $\vec{Q}_n$ for n-th harmonic is defined as (see [3] for details)

$$\begin{aligned}\vec{Q}_n &= (Q_{n,x}, Q_{n,y}) = \left(\sum_i w_i \cos(n\phi_i), \sum_i w_i \sin(n\phi_i)\right) \\ &= (Q_n \cos(n\Psi_n), Q_n \sin(n\Psi_n)) \,. \end{aligned} \quad (2)$$

The quantities w_i and ϕ_i are the weight and the azimuthal angle in the laboratory frame for the ith particle, respectively. From Eq. (2) it follows that the event plane angle Ψ_n can be expressed via the *arctan2* function, which takes into account the signs of both vector components to place the angle in the correct quadrant,

$$\Psi_n = \arctan 2(Q_{n,y}, Q_{n,x})/n \,. \quad (3)$$

The nth harmonic v_n of the anisotropic flow at given rapidity y, transverse momentum p_T, and centrality σ/σ_{geo} is determined with respect to the Ψ_n angle

$$v_n(y, p_T, \sigma/\sigma_{geo}) = \langle \cos[n(\phi_i - \Psi_n)] \rangle \quad (4)$$

by averaging $\langle \ldots \rangle$ over all particles in all measured events. It is easy to see that the event plane angle for the elliptic flow Ψ_2 does not necessarily coincide with that for the hexadecapole flow Ψ_4. To compare our model results with the experimental ones we need, therefore, the data where the fourth harmonic is extracted with respect to the Ψ_2 rather than the Ψ_4 event plane angle.

To demonstrate the development of both v_2 and v_4 at different centralities, we display the flow harmonics for charged particles in heavy-ion collisions at RHIC and LHC energies in Figs. 3 and 4, respectively. The experimental data by the PHENIX (RHIC) and the ALICE (LHC) Collaborations are plotted onto the simulations as well. One can see here that HYDJET++ overestimates the elliptic flow of charged hadrons with transverse momenta $2\,\mathrm{GeV}/c \le p_T \le 4\,\mathrm{GeV}/c$ in both reactions considered. This indicates that simplified combination of ideal hydrodynamics and jets is probably enough to simulate first two even harmonics of anisotropic flow at $p_T \le 2\,\mathrm{GeV}/c$, whereas at higher transverse momenta other mechanisms, e.g., coalescence, should be taken into account for better quantitative description of the flow behavior.

The elliptic flow produced by the jet hadrons with $p_T \le 2$ GeV/c is almost zero. Because of the jet quenching, the flow increases to $3 - -5\%$ with rising transverse momentum; however, the jets alone cannot provide strong flow signal, say $v_2 \approx 10\%$, even at LHC energies. Since the v_4 created by jets is also very small, it would be instructive to study how the admixture of jet hadrons can alter the v_4/v_2^2 ratio.

The ratio $R = v_4/v_2^2$ as a function of transverse momentum is presented in Figs. 5 and 6 for four different centralities in Au + Au collisions at RHIC and in Pb

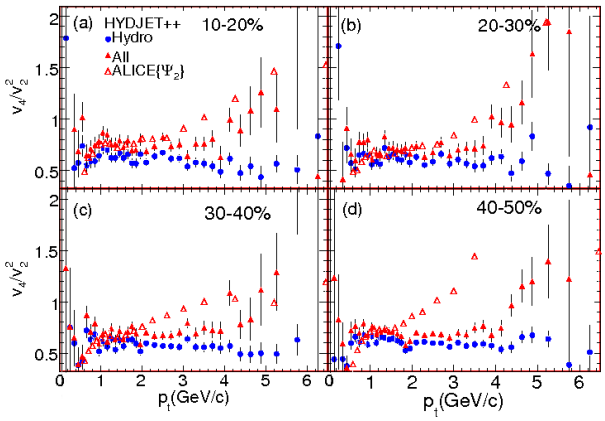

FIG. 6: (Color online) The same as Fig. 5 but for Pb + Pb collisions at $\sqrt{s} = 2.76A$ GeV.

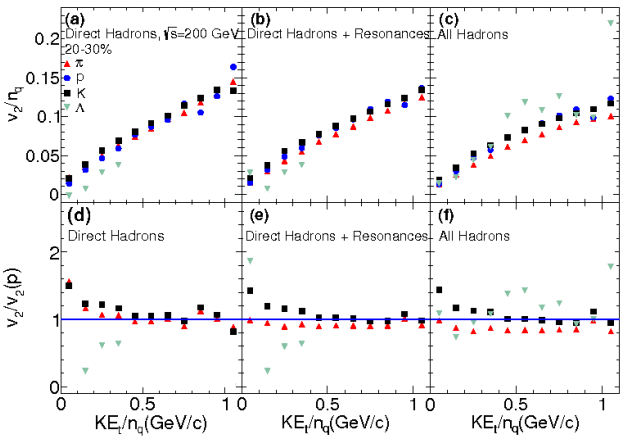

FIG. 7: (Color online) Upper row: The KE_T/n_q dependence of elliptic flow for (a) direct hadrons, (b) hadrons produced both directly and from resonance decays, and (c) all hadrons produced in the HYDJET++ model for Au + Au collisions at $\sqrt{s} = 200A$ GeV with centrality 20−−30%. Bottom row: The KE_T/n_q dependence of the ratios $(v_2/n_q)/(v_2^p/3)$ for (d) direct hadrons, (e) direct hadrons plus hadrons from the decays, and (f) all hadrons.

+ Pb collisions at LHC, respectively. The final result is compared here to the ratio obtained merely for hydro-like processes and to the experimental data. As was mentioned in [11], the measured ratio should be noticeably larger than 0.5. There are event-by-event fluctuations that increase R even if both flow harmonics are determined by means of the Ψ_2 event plane angle. The increase occurs because of the averaging of both v_2 and v_4 over the whole event sample before taking the ratio. These fluctuations are lacking in the HYDJET++; therefore, the data used for the comparison are properly reduced. See [11, 12] for details. It is seen that parametrized hydrodynamics with the extended table of resonances already provides $v_4/v_2^2 \approx 0.6$, which is higher than the theoretical value of $R = 0.5$. Jet particles increase this ratio further to value $R \approx 0.65$ at RHIC and $R \approx 0.7$ at LHC. While the ratio R is insensitive to the transverse momentum at $0.1\text{GeV}/c \leq p_T \leq 3\,\text{GeV}/c$, at higher p_T it increases with rising transverse momentum both in model simulations and in the experiment, although the RHIC data favor a weaker dependence. Thorough study of this problem within the hydrodynamic model indicates [12] that neither the initial conditions nor the shear viscosity can be accounted for the rise of high-p_T tail of the distribution. It looks like this rise can be attributed solely to jet phenomenon.

At LHC energy the increase of R with rising transverse momentum at $p_T \geq 3\,\text{GeV}/c$ is quite distinct. The difference between the model results and the data visible for semiperipheral collisions at $40\% \leq \sigma/\sigma_{geo} \leq 50\%$ can be partly explained by the imperfect description of the elliptic flow at $p_T \geq 2.5\,\text{GeV}/c$; see Fig. 4. Also, the STAR results concerning the v_2 are about 15−−20% higher than the PHENIX data, and the HYDJET++ model is tuned to averaged values provided by these two RHIC experiments. Nevertheless, the effect of hard processes is clear: The hydrodynamic part of the code yields rather flat ratio v_4/v_2^2, whereas the jets provide the rise of the high-p_T tail.

IV. NUMBER-OF-CONSTITUENT-QUARK SCALING

The number-of-constituent-quark (NCQ) scaling in the development of elliptic flow was first observed in Au + Au collisions at RHIC [13, 14]. If the elliptic flow, v_2, and the transverse kinetic energy, $KE_T \equiv m_T - m_0$, of any hadron species are divided by the number of constituent quarks, i.e., $n_q = 3$ for a baryon and $n_q = 2$ for a meson, then the scaling in $v_2(KE_T)$ holds up until $KE_T/n_q \approx 1\,\text{GeV}$ [32]. The observation of the NCQ scaling seems to favor the idea of the elliptic flow formation already on a partonic level. For instance, as pointed out in [33], the scaling is broken if hadrons are produced in the course of string fragmentation, whereas the process of quark coalescence leads to the scaling emergence. On the other hand, as was shown in Refs. [27, 28], the fulfillment of the NCQ scaling at ultrarelativistic energies depends strongly on the interplay between the decays of resonances and jets. Note that the breaking of the NCQ scaling at LHC was observed experimentally in [15, 34].

To demonstrate the importance of both resonance decays and jets for the formation of NCQ scaling we plot the reduced functions $v_2^h/n_q(KE_T/n_q)$ for several hadronic species obtained in HYDJET++ simulations of heavy-ion collisions at RHIC (Fig. 7) and at LHC (Fig. 8) energies in centrality bin 20−−30%. These distributions are then also normalized to the flow of protons, $v_2^h/n_q : v_2^p/3$, to see explicitly degree of the scaling fulfillment. The study is subdivided into three steps. The flow of hadrons

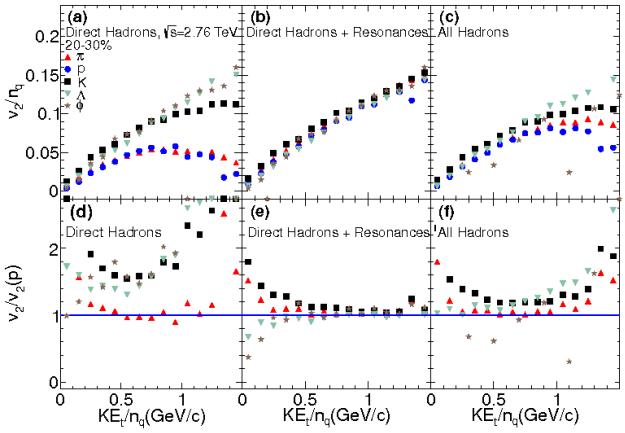

FIG. 8: (Color online) The same as Fig .7 but for Pb + Pb collisions at $\sqrt{s} = 2.76A$ TeV.

straight after the thermal freeze-out in hydrodynamic calculations is displayed in left windows. Central windows present this flow modified by the final state interactions, i.e., decays of resonances. Finally, right windows show the resulting flow of hadrons coming from all processes.

At RHIC energy, it looks like at given centrality the direct pions, protons and kaons are produced already obeying the scaling within the 5−−10% accuracy limit; see Figs. 7(a) and 7(d). The scaling holds also after decays of resonances as demonstrated in Figs. 7(b) and 7(e). Its fulfillment becomes slightly worse when hadrons from jets are taken into account; however, the NCQ scaling remains valid within 10% accuracy at least for three main hadron species. The situation is drastically changed for the collisions at LHC. Here spectra of directly produced particles do not possess any scaling properties, as one can see in Figs. 8(a) and 8(d). After final-state interactions the scaling conditions for hadrons in hydrodynamic simulations are restored, as displayed in Figs. 8(b) and 8(e). Even ϕ mesons follow the unique trend. Why? Spectra of many light hadrons, especially pions and protons, are getting feed-down from heavy resonances, whereas the spectrum of ϕ remains unchanged. The resonance boost makes elliptic flows of light hadrons harder. As a result, the NCQ scaling is fulfilled in a broad range of KE_T/n_q in the hydro sector of the model. In contrast, hard processes cause significant distortions of particle spectra and lead to violation of the scaling conditions; see Figs. 8(c) and 8(f), in accordance with experimental observations [15, 34].

V. CONCLUSIONS

Formation of elliptic v_2 and hexadecapole v_4 flows of hadrons in Au + Au collisions at $\sqrt{s} = 200A$ GeV and in Pb + Pb collisions at $\sqrt{s} = 2.76A$ TeV is studied within the HYDJET++ model. This model combines the parametrized hydrodynamics with hard processes (jets). Therefore, the main aim was to investigate the role of interplay between soft and hard processes for the development of flow. Several features have been observed. First, the jets are found to increase the ratio $R = v_4/v_2^2$ for both considered heavy-ion reactions. Second, jets lead to rise of the high-p_T tail of the ratio R. Such a behavior is observed experimentally but cannot be reproduced by conventional hydro models relying on ideal or viscous hydrodynamics. Third, the resonance feed-down significantly enhances the flow of light hadrons and modifies their spectra toward the fulfillment of number-of-constituent-quark scaling. The flow of particles produced in jet fragmentation is quite weak, thus jets are working against the scaling. Due to interplay of resonance and jet contribution, the NCQ scaling works well only at certain energies, where jets are not abundant. Because jet influence increases with rising collision energy, just approximate NCQ scaling is observed at LHC despite the fact that the scaling holds for the pure hydrodynamic part of hadron spectra. At higher collision energies scaling performance should get worse.

Acknowledgments

Fruitful discussions with I. Lokhtin, L. Malinina, I. Mishustin, and A. Snigirev are gratefully acknowledged. We are thankful to J.-Y. Ollitrault and K. Redlich for bringing to our attention the v_4/v_2^2 problem. This work was supported in part by the QUOTA Program and Norwegian Research Council (NFR) under Contract No. 185664/V30.

[1] S. A. Voloshin and Y. Zhang, Z. Phys. **C70**, 665 (1996).
[2] A. M. Poskanzer and S. A. Voloshin, Phys. Rev. C **58**, 1671 (1998).
[3] S. A. Voloshin, A. M. Poskanzer, and R. Snellings, in *Relativistic Heavy Ion Physics* (Springer, Heidelberg, 2010), vol. I-23, pp. 293−−333 (arXiv:0809.2949 [nucl-ex]).
[4] PHENIX Collaboration, S. Esumi *et al.*, J. Phys. G **38**, 124010 (2011).
[5] CMS Collaboration, J. Velkovska *et al.*, J. Phys. G **38**, 124011 (2011).
[6] ATLAS Collaboration, J. Jia *et al.*, J. Phys. G **38**, 124012 (2011).
[7] ALICE Collaboration, R. Snellings *et al.*, J. Phys. G **38**, 124013 (2011).
[8] N. Borghini and J.-Y. Ollitrault, Phys. Lett. **B642**, 227 (2006).

[9] STAR Collaboration, J. Adams *et al.*, Phys. Rev. Lett. **92**, 062301 (2004); Phys. Rev. C **72**, 014904 (2005).

[10] PHENIX Collaboration, A. Adare *et al.*, Phys. Rev. Lett. **105**, 062301 (2010).

[11] C. Gombeaud and J.-Y. Ollitrault, Phys. Rev. C **81**, 014901 (2010).

[12] M. Luzum, C. Gombeaud, and J.-Y. Ollitrault, Phys. Rev. C **81**, 054910 (2010).

[13] J. Adams *et al.* (STAR Collaboration), Phys. Rev. Lett. **92**, 052302 (2004).

[14] PHENIX Collaboration, S. S. Adler *et al.*, Phys. Rev. Lett. **91**, 182301 (2003).

[15] ALICE Collaboration, M. Krzewicki *et al.*, J. Phys. G **38**, 124047 (2011).

[16] I. P. Lokhtin, L. V. Malinina, S. V. Petrushanko, A. M. Snigirev, I. Arsene, and K. Tywoniuk, Comput. Phys. Commun. **180**, 779 (2009).

[17] N. S. Amelin, R. Lednicky, T. A. Pocheptsov, I. P. Lokhtin, L. V. Malinina, A. M. Snigirev, Iu. A. Karpenko, and Yu. M. Sinyukov, Phys. Rev. C **74**, 064901 (2006).

[18] N. S. Amelin, R. Lednicky, I. P. Lokhtin, L. V. Malinina, A. M. Snigirev, Iu. A. Karpenko, Yu. M. Sinyukov, I. Arsene, and L. Bravina, Phys. Rev. C **77**, 014903 (2008).

[19] I. P. Lokhtin and A. M. Snigirev, Eur. Phys. J. **C46**, 211 (2006); http://cern.ch/lokhtin/hydro/hydjet.html.

[20] G. Torrieri, S. Steinke, W. Broniowski, W. Florkowski, J. Letessier, and J. Rafelski, Comput. Phys. Commun. **167**, 229 (2005).

[21] K. Tywoniuk, I. C. Arsene, L. Bravina, A. B. Kaidalov, and E. Zabrodin, Phys. Lett. **B657**, 170 (2007).

[22] http://cern.ch/lokhtin/pyquen.

[23] T. Sjostrand, S. Mrenna, and P. Skands, J. High Energy Phys. **0605**, 026 (2006); http://home.thep.lu.se/~torbjorn/Pythia.html.

[24] B. Andersson, G. Gustafson, G. Ingelman, and T. Sjostrand, Phys. Rep. **97**, 31 (1983).

[25] P. Z. Skands, Phys. Rev. D **82**, 074018 (2010), arXiv:1005.3457v4 [hep-ph].

[26] ATLAS Collaboration, CERN preprint ATL-PHYS-PUB-2011-009.

[27] G. Eyyubova, L. V. Bravina, E. E. Zabrodin, V. L. Korotkikh, I. P. Lokhtin, L. V. Malinina, S. V. Petrushanko, and A. M. Snigirev, Phys. Rev. C **80**, 064907 (2009).

[28] E. Zabrodin, G. Eyyubova, L. Bravina, I. P. Lokhtin, L. V. Malinina, S. V. Petrushanko, and A. M. Snigirev, J. Phys. G. **37**, 094060 (2010).

[29] I. P. Lokhtin, A. V. Belyaev, L. V. Malinina, S. V. Petrushanko, E. P. Rogochaya, and A. M. Snigirev, Eur. Phys. J. **C72**, 2045 (2012).

[30] E. Zabrodin, G. Eyyubova, L. Malinina, and L. Bravina, Acta Phys. Polon. B, Supp. **5**, 349 (2012).

[31] ALICE Collaboration, B. Abelev *et al.*, CERN preprint CERN-PH-EP-2012-142 (unpublished) (arXiv:1205.5761 [nucl-ex]).

[32] PHENIX Collaboration, A. Adare *et al.*, Phys. Rev. Lett. **98**, 162301 (2007).

[33] J. Tian, J. H. Chen, Y. G. Ma, X. Z. Cai, F. Jin, G. L. Ma, S. Zhang, and C. Zhong, Phys. Rev. C **79**, 067901 (2009).

[34] ALICE Collaboration, F. Noferini *et al.*, arXiv:1212.1292 [nucl-ex].

.2 Higher harmonics in relativistic heavy ion collisions in HYDJET++ model

Higher harmonics of azimuthal anisotropy in relativistic heavy ion collisions in HYDJET++ model

L.V. Bravina[2], B.H. Brusheim Johansson[2,3], G.Kh. Eyyubova[1,4], V.L. Korotkikh[1], I.P. Lokhtin[1], L.V. Malinina[1], S.V. Petrushanko[1], A.M. Snigirev[1], E.E. Zabrodin[2,1]

[1] Skobeltsyn Institute of Nuclear Physics, Lomonosov Moscow State University, Moscow, Russia
[2] The Department of Physics, University of Oslo, Norway
[3] Oslo and Akershus University College for Applied Sciences, Oslo, Norway
[4] Czech Technical University in Prague, FNSPE, Prague, Czech Republic

Abstract. The LHC data on azimuthal anisotropy harmonics from PbPb collisions at center-of-mass energy 2.76 TeV per nucleon pair are analyzed and interpreted in the framework of the HYDJET++ model. The cross-talk of elliptic v_2 and triangular v_3 flow in the model generates both even and odd harmonics of higher order. Comparison with the experimental data shows that this mechanism is able to reproduce the $p_{\rm T}$ and centrality dependencies of quadrangular flow v_4, and also the basic trends for pentagonal v_5 and hexagonal v_6 flows.

1 Introduction

The study of the fundamental theory of strong interactions (Quantum Chromodynamics, QCD) in the regimes of extreme densities and temperatures is ongoing via the measurement of the properties of hot and dense multi-parton systems produced in high-energy nuclear collisions (see, e.g., reviews [1–4]). The started LHC heavy ion program makes it possible to probe the new frontiers of the high temperature QCD providing the valuable information on the dynamical behavior of quark-gluon matter (QGM), as predicted by lattice calculations. A number of interesting LHC results from PbPb runs at $\sqrt{s}_{\rm NN} = 2.76$ TeV, have been published by ALICE, ATLAS and CMS collaborations (see [5] for the overview of the results from the first year of heavy ion physics at LHC).

One of the modern trends in heavy ion physics at high energies is a study of Fourier harmonics of azimuthal particle distribution, which is a powerful probe of bulk properties of the created high density matter. It is typically described by a Fourier series of the form:

$$E\frac{d^3N}{dp^3} = \frac{d^2N}{2\pi p_{\rm T} dp_{\rm T} d\eta} \times \{1 + 2\sum_{n=1}^{\infty} v_{\rm n}(p_{\rm T},\eta)\cos\left[n(\varphi - \Psi_{\rm n})\right]\}\ , \qquad (1)$$

where φ is the azimuthal angle with respect to the reaction plane $\Psi_{\rm n}$, and $v_{\rm n}$ are the Fourier coefficients. The second harmonic, v_2, referred to as "elliptic flow", is the most extensively studied one, because it directly relates the anisotropic shape of the overlap of the colliding nuclei to the corresponding anisotropy of the outgoing momentum distribution. The momentum and centrality dependencies of the elliptic flow in PbPb collisions were measured at the LHC [6–8] in the first instance. Then, the results of measurements of the higher azimuthal harmonics [9–11] and the anisotropic flow of identified particles [12] were published. The higher order coefficients $v_{\rm n}$ (n$>$ 2) are smaller than v_2. They also carry important information on the dynamics of the medium created, and complement v_2 in providing a more complete picture of its bulk properties. The two coefficients that have been closely studied are the quadrangular (or hexadecapole) flow v_4 [13,14] and triangular flow v_3 [15]. Although the pentagonal and hexagonal flows v_5 and v_6 are studied to a lesser extent, there exist some predictions from hydrodynamics on them also [16].

At relatively low transverse momenta, $p_{\rm T} < 3 \div 4$ GeV/c, the azimuthal anisotropy results from a pressure-driven anisotropic expansion of the created matter, with more particles emitted in the direction of the largest pressure gradients [17]. At higher $p_{\rm T}$, this anisotropy is understood to result from the path-length dependent energy loss of partonic jets as they traverse the matter, with more jet particles emitted in the direction of shortest path-length [18].

In Ref. [19] the LHC data on multiplicity, charged hadron spectra, elliptic flow and femtoscopic correlations from PbPb collisions were analyzed in the frameworks of the HYDJET++ model [20]. Taking into account both hard and soft components and tuning input parameters allow HYDJET++ to reproduce these data. Another study [21] with HYDJET++ was dedicated to the influence of jet production mechanism on the ratio v_4/v_2^2 and its role in violation of the number-of-constituent-quark (NCQ) scaling [22], predicted within the HYDJET++ in [23]. In the current paper, tuned HYDJET++ is applied to analyze

the LHC data on momentum and centrality dependences of azimuthal anisotropy harmonics in PbPb collisions, and then to illuminate the mechanisms of the generation of Fourier coefficients $v_2 \div v_6$. The detailed study of hexagonal flow v_6 is also the subject of our recent paper [24].

Note that the LHC data on higher-order azimuthal anisotropy harmonics ($v_2 \div v_4$) were analyzed with a multiphase transport model (AMPT) in [25]. It was shown that AMPT describes LHC data on the anisotropic flow coefficients v_n (n=2÷4) for semi-central PbPb collisions at $p_T < 3$ GeV/c. It also reproduces reasonably well the centrality dependence of integral v_n for all but most central collisions. Another approach [26] reproducing v_n data in ultrarelativistic heavy ion collisions is the glasma flow with the subsequent relativistic viscous hydrodynamic evolution of matter through the quark-gluon plasma and hadron gas phases (IP-Glasma+MUSIC model). This model gives good agreement to p_T-dependence of v_n (n=2÷5) and event-by-event distributions of $v_2 \div v_4$ at RHIC and LHC.

The study of generation of higher flow harmonics within the HYDJET++ has several attractive features. Firstly, the presence of elliptic and triangular flow permits us to examine the interference of these harmonics and its contribution to all higher even and odd components of the anisotropic flow. If necessary, the original eccentricities of higher order can be easily incorporated in the model for the fine tuning of the distributions. Secondly, very rich table of resonances, which includes about 360 meson and baryon species, helps one to analyze all possible final state interactions. Thirdly, the interplay of ideal hydrodynamics with jets can unveil the role of hard processes in the formation of anisotropic flow of secondary hadrons. The basic features of the model are described in Sect. 2.

2 HYDJET++ model

HYDJET++ (the successor of HYDJET [27]) is the model of relativistic heavy ion collisions, which includes two independent components: the soft state (hydro-type) and the hard state resulting from the in-medium multi-parton fragmentation. The details of the used physics model and simulation procedure can be found in the HYDJET++ manual [20]. Main features of the model are sketched below as follows.

The soft component of an event in HYDJET++ is the "thermal" hadronic state generated on the chemical and thermal freeze-out hypersurfaces obtained from the parametrization of relativistic hydrodynamics with preset freeze-out conditions (the adapted event generator FAST MC [28,29]). Hadron multiplicities are calculated using the effective thermal volume approximation and Poisson multiplicity distribution around its mean value, which is supposed to be proportional to a number of participating nucleons for a given impact parameter of a AA collision. To simulate the elliptic flow effect, the hydro-inspired parametrization is implemented for the momentum and spatial anisotropy of a soft hadron emission source [20,30].

The model used for the hard component in HYDJET++ is based on the PYQUEN partonic energy loss model [27]. The approach describing the multiple scattering of hard partons relies on accumulated energy loss via gluon radiation which is associated with each parton scattering in expanding quark-gluon fluid. It also includes the interference effect in gluon emission with a finite formation time using the modified radiation spectrum dE/dx as a function of the decreasing temperature T. The model takes into account radiative and collisional energy loss of hard partons in longitudinally expanding quark-gluon fluid, as well as the realistic nuclear geometry. The simulation of single hard nucleon-nucleon sub-collisions by PYQUEN is constructed as a modification of the jet event obtained with the generator of hadron-hadron interactions PYTHIA_6.4 [31]. Note, that Pro-Q20 tune was used for the present simulation. The number of PYQUEN jets is generated according to the binomial distribution. The mean number of jets produced in an AA event is calculated as a product of the number of binary NN sub-collisions at a given impact parameter per the integral cross section of the hard process in NN collisions with the minimum transverse momentum transfer $p_T^{\min}$ (the latter is an input parameter of the model). In HYDJET++, partons produced in (semi)hard processes with the momentum transfer lower than $p_T^{\min}$, are considered as being "thermalized". So, their hadronization products are included "automatically" in the soft component of the event. In order to take into account the effect of nuclear shadowing on parton distribution functions, we use the impact parameter dependent parametrization [32] obtained in the framework of Glauber-Gribov theory.

The model has a number of input parameters for the soft and hard components. They are tuned from fitting to experimental data values for various physical observables, see [19] for details.

In order to simulate higher azimuthal anisotropy harmonics, the following modification has been implemented in the model. HYDJET++ does not contain the fireball evolution from the initial state to the freeze-out stage. Instead of application of computational relativistic hydrodynamics, which is extremely time consuming, HYDJET++ employs the simple and frequently used parametrizations of the freeze-out hypersurface [20]. Then, anisotropic elliptic shape of the initial overlap of the colliding nuclei results in a corresponding anisotropy of the outgoing momentum distribution. To describe the second harmonic v_2 the model utilizes coefficients $\delta(b)$ and $\epsilon(b)$ representing, respectively, the flow and the coordinate anisotropy of the fireball at the freeze-out stage as functions of the impact parameter b. These momentum and spatial anisotropy parameters $\delta(b)$ and $\epsilon(b)$ can either be treated independently for each centrality, or can be related to each other through the dependence on the initial ellipticity $\epsilon_0(b) = b/2R_A$, where R_A is the nucleus radius. The last option allows us to describe the elliptic flow coefficient v_2 for most centralities at the RHIC [20] and LHC [19] energies using only two independent on centrality parameters.

Non-elliptic shape of the initial overlap of the colliding nuclei, which can be characterized by the initial triangular coefficient $\epsilon_{03}(b)$, results in an appearance of

higher Fourier harmonics in the outgoing momentum distribution. Our Monte-Carlo (MC) procedure allows us to parametrize easily this anisotropy via the natural modulation of final freeze-out hypersurface, namely

$$R(b,\phi) = R_{\rm f}(b)\frac{\sqrt{1-\epsilon^2(b)}}{\sqrt{1+\epsilon(b)\cos 2\phi}}[1+\epsilon_3(b)\cos 3(\phi+\Psi_3^{\rm RP})] \ , \quad (2)$$

where ϕ is the spatial azimuthal angle of the fluid element relatively to the direction of the impact parameter. $R(b,\phi)$ is the fireball transverse radius in the given azimuthal direction ϕ with the scale $R_{\rm f}(b)$, which is a model parameter. The phase $\Psi_3^{\rm RP}$ allows us to introduce the third harmonics possessing its own reaction plane, randomly distributed with respect to the direction of the impact parameter ($\Psi_2^{\rm RP}=0$). This new anisotropy parameter $\epsilon_3(b)$ can again be treated independently for each centrality, or can be expressed through the initial ellipticity $\epsilon_0(b)=b/2R_A$. Note, that such modulation does not affect the elliptic flow coefficient v_2, which was fitted earlier with two parameters $\delta(b)$ and $\epsilon(b)$ [19,20]. Figure 1 illustrates second and third harmonics generation in HYDJET++ by representing particle densities in the transverse plane. One should be aware that the triangular deformation shown here is very strong. The actual deformations needed to describe triangular flow at LHC energies are typically order of magnitude weaker.

The modulation of the maximal transverse flow rapidity, first considered in Eq. (28) of Ref. [20] at the parametrization of 4-velocity u,

$$\rho_{\rm u}^{\rm max} = \rho_{\rm u}^{\rm max}(b=0)[1+\rho_{3\rm u}(b)\cos 3\phi + \rho_{4\rm u}(b)\cos 4\phi] \ , \quad (3)$$

also permits the introduction of higher azimuthal harmonics related, however, to the direction of the impact parameter ($\Psi_2^{\rm RP}=0$) only. In this case we get the modulation of the velocity profile in all freeze-out hypersurface, and can not "rotate" this modulation with independent phase. The new anisotropy parameters, $\rho_{3\rm u}(b)$ and $\rho_{4\rm u}(b)$, can again be treated independently for each centrality, or can be expressed through the initial ellipticity $\epsilon_0(b)=b/2R_A$.

For current simulations we have introduced the minimal modulation in HYDJET++ using just simple parameterizations $\epsilon_3(b) \propto \epsilon_0^{1/3}(b)$ and $\rho_{4\rm u}(b) \propto \epsilon_0(b)$, while $\rho_{3\rm u}(b)$ being taken equal to zero. The corresponding proportionality factors were selected from the best fit of the data to $v_3(p_{\rm T})$ and $v_4(p_{\rm T})$.

Let us mark that the azimuthal anisotropy parameters $\epsilon(b)$, $\delta(b)$ and $\epsilon_3(b)$ are fixed at given impact parameter b. Therefore they do not provide dynamical event-by-event flow fluctuations, and specify $v_{\rm n}(b)$ accumulated over many events. The main source of flow fluctuations in HYDJET++ is fluctuations of particle momenta and multiplicity. Recall, that the momentum-coordinate correlations in HYDJET++ for soft component is governed by collective velocities of fluid elements, and so the fluctuations in particle coordinates are reflected in their momenta. The fluctuations became stronger as resonance decays and (mini-)jet production are taken into account. An event distribution over collision impact parameter for each centrality class also increases such fluctuations. In the current paper we restrict ourselves to analysis of the event-averaged $v_{\rm n}(p_{\rm T})$. The detailed study of event-by-event flow fluctuations is the subject of our future investigation. The possible further modification of HYDJET++ to match experimental data on flow fluctuations would be smearing of parameters ϵ, δ and ϵ_3 at a given b.

3 Results

It was demonstrated in [19] that tuned HYDJET++ model can reproduce the LHC data on centrality and pseudorapidity dependence of inclusive charged particle multiplicity, $p_{\rm T}$-spectra and $\pi^{\pm}\pi^{\pm}$ correlation radii in central PbPb collisions, and $p_{\rm T}$- and η-dependencies of the elliptic flow coefficient v_2 (up to $p_{\rm T} \sim 5$ GeV/c and 40% centrality). However the reasonable treatment of higher and odd Fourier harmonics of particle azimuthal distribution $v_{\rm n}$ ($n>2$) needs the additional modifications of the model, which does not effect azimuthally-integrated physical observables (see previous section). We have compared the results of HYDJET++ simulations with the LHC data on $v_{\rm n}$ for inclusive as well as for identified charged hadrons.

3.1 Anisotropy harmonics for inclusive charge hadrons

The standard way of measuring $v_{\rm n}$ corresponds to the inclusive particle harmonics on the base of Eq. (1). Then $v_{\rm n}$ is extracted using the special methods, such as the event plane $v_{\rm n}\{{\rm EP}\}$ [33], or m-particle cumulant $v_{\rm n}\{m\}$ [34,35], or Lee-Yang zero methods $v_{\rm n}\{{\rm LYZ}\}$ [36,37]. In order to estimate the uncertainties related to the experimental definitions of flow harmonics, HYDJET++ results for different methods of $v_{\rm n}$ extraction were compared with its "true" values, known from the event generator and determined relatively to $\Psi_2^{\rm RP}$ for even and $\Psi_3^{\rm RP}$ for odd harmonics, respectively.

Figures 2-11 show anisotropic flow coefficients $v_{\rm n}$ as a function of the hadron transverse momentum $p_{\rm T}$. Let us discuss first the results of HYDJET++ simulations. It can be separated in two groups: (i) results obtained with respect to the true reaction plane straight from the generator, i.e., $v_{2,4,6}(\Psi_2^{\rm RP})$ and $v_{3,5}(\Psi_3^{\rm RP})$, and (ii) those obtained by using the (sub)event plane method with rapidity gap $|\Delta\eta|>3$. The last method provides us with $v_{\rm n}\{{\rm EP}\}$. The main systematic uncertainties for the methods come from non-flow correlations and flow fluctuations. The last one (as it is kept in the model currently) almost does not affect mean $v_{\rm n}$ values restored by the EP method, while the non-flow correlations can be effectively suppressed by applying η-gap in $v_{\rm n}$ reconstruction. This gives us a good reconstruction precision for elliptic v_2, triangular v_3, and quadrangular v_4 flows up to $p_{\rm T} \sim 5$ GeV/c. At higher transverse momenta some differences appear due to non-flow effects from jets. However, Figs. 8 and 9 show that pentagonal flow v_5 determined from the model w.r.t. $\Psi_3^{\rm RP}$ and v_5 restored w.r.t. the event plane of 5-th order $\Psi_5^{\rm EP}$ differ a lot. The reason is that although no intrinsic $\Psi_5^{\rm RP}$

is generated in HYDJET++, pentagonal flow v_5 emerges here as a result of the "interference" between v_2 and v_3, each is determined with respect to its own reaction plane, $v_5 \propto v_2(\Psi_2^{\rm RP}) \cdot v_3(\Psi_3^{\rm RP})$, in line with the conclusions of Ref. [38]. Hexagonal flow v_6 is also very sensitive to the methods used due to nonlinear interplay of elliptic and triangular flows generating v_6, see [24] for details. The results of HYDJET++ for $v_6\{\rm EP\}$ are not shown on the plots because of too large statisitcal errors.

Note, that the experimental situation is even more complicated, and the dependence of measured $v_{\rm n}$ on methods applied may be more crucial for all n due to apparently larger fluctuations in the data than in the model. For instance, it was shown in [39] that event-by-event fluctuations in the initial state may lead to characteristically different $p_{\rm T}$-dependencies for the anisotropic flow coefficients extracted by different experimental methods.

It is also worth mentioning here that the hump-like structure of the simulated $v_2(p_{\rm T})$ and $v_3(p_{\rm T})$ signals appears due to interplay of hydrodynamics and jets. At transverse momenta $p_{\rm T} \geq 3\,{\rm GeV}/c$ the spectrum of hadrons is dominated by jet particles which carry very weak flow. Thus, the elliptic and triangular flows in the model also drop at certain $p_{\rm T}$. Higher flow harmonics arise in the model solely due to the presence of the v_2, v_3 and its interference. Therefore, transverse momentum distributions of these harmonics inherit the characteristic hump-like shapes.

Now let us consider the ATLAS [10] and CMS [8,11] data plotted onto the model results in Figs. 2-11 for different centrality classes. The event plane for $v_{\rm n}\{\rm EP\}$ was defined experimentally with respect to n-th harmonics in all cases with the exeption of CMS data for $v_6\{\rm EP/\Psi_2\}$, which was measured using second harmonics. One can see that HYDJET++ reproduces experimentally measured $p_{\rm T}$-dependences of v_2, v_3 and $v_4\{\rm LYZ\}$ up to $p_{\rm T} \sim 5$ GeV/c. The centrality dependence of v_4 measured by event plane and two-particle cumulant methods is significantly weaker than that of v_4 measured by Lee-Yang zero method, presumably due to large non-flow contribution and increase of the flow fluctuations in more central events. Since the model is tuned to fit the $p_{\rm T}-$dependencies of $v_4\{\rm LYZ\}$, it underestimates the quadrangular flow, restored by the EP or two-particle cumulant methods, in (semi-)central collisions. Recall, that in ideal hydrodynamics (at the limit of small temperatures, large transverse momenta and absence of the flow fluctuations) $v_4\{\Psi_2\}/v_2^2 = 0.5$ [40].

The same trend is seen for $p_{\rm T}$-dependencies of the pentagonal flow. For central and semi-central topologies up to $\sigma/\sigma_{\rm geo} \approx 20\%$ the $v_5\{\rm EP\}$ in the model underestimates the experimentally measured $v_5\{\rm EP\}$, whereas for more peripheral collisions the agreement between the model and the data is good. Unfortunately, there are no data on pentagonal flow extracted by the LYZ method. As we have seen, for v_2, v_3 and v_4 in central and semi-central collisions the LYZ method provides noticeably weaker flow compared to that obtained by the EP method. One may expect, therefore, that the pentagonal flow, $v_5\{\rm LYZ\}$, almost free from non-flow contributions, should be closer to the v_5 generated by the HYDJET++. If the future experimental data on v_5 will persist on stronger flow, this fact can be taken as indication of the possible presence of additional pentagonal eccentricity $\epsilon_5(b)$ with the new phase $\Psi_5^{\rm RP}$ responsible for genuine v_5. Both parameters can be easily inserted in Eq. (2) for the modulation of the final freeze-out hypersurface.

At last, $p_{\rm T}$-dependencies of the hexagonal flow in HYDJET++ are similar to that seen in CMS data within the uncertainties related to methods used. However $v_6(\Psi_2^{\rm RP})$ in the model visibly underestimates ATLAS data on $v_6\{\rm EP\}$ for most central events. The latter fact may be explained by a siginificant v_3 contribution to $v_6\{\rm EP\}$ in central collisions, which is not presented in $v_6(\Psi_2^{\rm RP})$ component: $v_6(\Psi_3^{\rm RP}) \sim v_6(\Psi_2^{\rm RP}) < v_6\{\rm EP\}$. On the other hand, the relative contribution to $v_6\{\rm EP\}$ coming from v_2 is instantly increasing as the reaction becomes more peripheral [24], and starting from 20$-$30% centralities we already get $v_6\{\rm EP\} \sim v_6(\Psi_2^{\rm RP}) \gg v_6(\Psi_3^{\rm RP})$ with the approximate agreement between the model and the data.

Some additional checks have been done as well. In the presence of only elliptic flow all odd higher harmonics are found to be essentially zero. The quadrangular flow is zero, $v_4 = 0$, if the elliptic flow is absent. The pentagonal flow disappears, $v_5 = 0$, in case of either $v_2 = 0$ or $v_3 = 0$. The hexagonal flow is zero, $v_6 = 0$, if both elliptic and triangular flows are absent, $v_2 = 0$ and $v_3 = 0$.

3.2 Anisotropy harmonics for identified charge hadrons

Finally, let us consider distributions for some hadronic species measured in PbPb collisions at the LHC. Before addressing to azimuthal anisotropy harmonics of identified hadrons, the comparision of HYDJET++ results with ALICE data [41] on $p_{\rm T}$-spectra of negatively charged pions, kaons and anti-protons in PbPb collisions is displayed in Fig. 12. One can see that HYDJET++ reproduces well the measured transverse momentum spectra of identified hadrons within the whole range of accessible $p_{\rm T}$.

Figure 13 presents the comparision of HYDJET++ results and the ALICE data [42] for the elliptic and triangular flow of pions, kaons and anti-protons at 10–20% and 40–50% centrality of PbPb collisions. The agreement between the model and the data for kaons and anti-protons looks fair. For pions the model underestimates the data a bit. The discrepancy is more pronounced for more central collisions indicating, perhaps, presence of strong non-flow correlations in the data.

4 Conclusion

Azimuthal anisotropy harmonics of inclusive and identified charged hadrons in PbPb collisions at $\sqrt{s_{\rm NN}} = 2.76$ TeV have been analyzed in the framework of HYDJET++ model. The effects of possible non-elliptic shape of the initial overlap of the colliding nuclei are implemented in HYDJET++ by the modulation of the final freeze-out hypersurface with the appropriate fitting triangular coefficient.

This modulation is not correlated with the direction of the impact parameter, and two independent "strong" lower azimuthal harmonics, v_2 and v_3, being obtained as a result. They are of different physical origin, coded partly in the different centrality dependence. Interference between v_2 and v_3 generates as "overtones" both even and odd higher azimuthal harmonics, v_4, v_5, v_6, etc.

This mechanism allows HYDJET++ to reproduce the LHC data on $p_{\rm T}$- and centrality dependencies of the anisotropic flow coefficients v_n (n=2÷4) up to $p_{\rm T} \sim 5$ GeV/c and 40% centrality, and also the basic trends for pentagonal v_5 and hexagonal v_6 flows. Some discrepancy between the model results and the data on the pentagonal flow in central events requires further study of additional sources of the non-flow correlations and flow fluctuations, which may be absent in the model. Although the introduction of internal higher harmonics is also possible in the HYDJET++, there is no clear evidence in the data to do so at present. Obtained results show that higher harmonics of the azimuthal flow get very significant contributions from the lower harmonics, v_2 and v_3. This circumstance makes it difficult to consider the higher harmonics as independent characteristics of the early phase of ultrarelativistic heavy ion collisions.

Acknowledgments

Discussions with A.V. Belyaev and D. d'Enterria are gratefully acknowledged. We thank our colleagues from CMS, ALICE and ATLAS collaborations for fruitful cooperation. This work was supported by Russian Foundation for Basic Research (grant 12-02-91505), Grants of President of Russian Federation for Scientific Schools Supporting (No. 3920.2012.2 and No. 3042.2014.2), Ministry of Education and Sciences of Russian Federation (agreement No. 8412), Norwegian Research Council (NFR), European Union and the Government of Czech Republic under the project "Support for research teams on CTU" (No. CZ.1.07/2.3.00/30.0034).

References

1. D. d'Enterria, J. Phys. **G 34**, (2007) S53
2. *Quark Gluon Plasma 4*, edited by R.C. Hwa and X.-N. Wang (World Scientific, Singapore, 2010).
3. C. Salgado, Proceedings of European School of High-Energy Physics (2008) 239, arXiv:0907.1219 [hep-ph]
4. I.M. Dremin, A.V. Leonidov, Phys. Usp. **53**, (2011) 1123
5. B. Muller, J. Schukraft, B. Wyslouch, Ann. Rev. Nucl. Part. Sci. **62**, (2012) 361
6. K. Aamodt, et al. (ALICE Collaboration), Phys. Rev. Lett. **105**, (2010) 252302
7. G. Aad, et al. (ATLAS Collaboration), Phys. Lett. **B 707**, (2012) 330
8. S. Chatrchyan, et al. (CMS Collaboration), Phys. Rev. **C 87**, (2013) 014902
9. K. Aamodt, et al. (ALICE Collaboration), Phys. Rev. Lett. **107**, (2011) 032301
10. G. Aad, et al. (ATLAS Collaboration), Phys. Rev. **C 86**, (2012) 014907
11. S. Chatrchyan, et al. (CMS Collaboration), arXiv:1310.8651 [nucl-ex]
12. B. Abelev, et al. (ALICE Collaboration), Phys. Lett. **B 719**, (2013) 18
13. P.F. Kolb, Phys. Rev. **C 68**, (2003) 031902
14. P.F. Kolb, L.-W. Chen, V. Greco, C.M. Ko, Phys. Rev. **C 69**, (2004) 051901
15. B. Alver, G. Roland, Phys. Rev. **C 81**, (2010) 054905
16. B.H. Alver, C. Gombeaud, M. Luzum, J.Y. Ollitrault, Phys. Rev. **C 82**, (2010) 034913
17. J.Y. Ollitrault, Phys. Rev. **D 46**, (1992) 229
18. M. Gyulassy, I. Vitev, X.-N. Wang, Phys. Rev. Lett. **86**, (2001) 2537
19. I.P. Lokhtin, A.V. Belyaev, L.V Malinina, S.V. Petrushanko, E.P. Rogochaya, A.M. Snigirev, Eur. Phys. J. **C 72**, (2012) 2045
20. I.P. Lokhtin, L.V Malinina, S.V. Petrushanko, A.M. Snigirev, I. Arsene, K. Tywoniuk, Comput. Phys. Commun. **180**, (2009) 779
21. L. Bravina, B.H. Brusheim Johansson, G. Eyyubova, E. Zabrodin, Phys. Rev. **C 87**, (2013) 034901
22. F. Noferini (for the ALICE Collaboration), Nucl. Phys. **A 904-905**, (2013) 438c
23. G. Eyyubova, et al., Phys. Rev. **C 80**, (2009) 064907
24. L. Bravina, et al., arXiv:1311.0747 [hep-ph]
25. J. Xu, C.M. Ko, Phys. Rev. **C 84**, (2011) 044907
26. C. Gale, S. Jeon, B. Schenke, P. Tribedy, R. Venugopalan, Phys. Rev. Lett. **110**, (2013) 012302
27. I.P. Lokhtin, A.M. Snigirev, Eur. Phys. J. **C 45**, (2006) 211
28. N.S. Amelin et al., Phys. Rev. **C 74**, (2006) 064901
29. N.S. Amelin et al., Phys. Rev. **C 77**, (2008) 014903
30. U. Wiedemann, Phys. Rev. **C 57**, (1998) 266
31. T. Sjostrand, S. Mrenna, P. Skands, JHEP **0605**, (2006) 026
32. K. Tywoniuk, I.C. Arsene, L. Bravina, A.B. Kaidalov, E. Zabrodin, Phys. Lett. **B 657**, (2007) 170
33. A.M. Poskanzer, S.A. Voloshin, Phys. Rev. **C 58**, (1998) 1671
34. N. Borghini, P.M. Dinh, J.Y. Ollitrault, Phys. Rev. **C 64**, (2001) 054901
35. N. Borghini, P.M. Dinh, J.Y. Ollitrault, nucl-ex/0110016
36. R.S. Bhalerao, N. Borghini, J.Y. Ollitrault, Nucl. Phys. **A 727**, (2003) 373
37. N. Borghini, R.S. Bhalerao, J.Y. Ollitrault, J. Phys. **G 30**, (2004) S1213
38. D. Teaney, L. Yan, Phys. Rev. **C 86**, (2012) 044908
39. U. Heinz, Z. Qiu, C. Shen, Phys. Rev. **C 87**, (2013) 034913
40. N. Borghini, J.-Y. Ollitrault, Phys. Lett. **B 642**, (2006) 227
41. R. Preghenella (for the ALICE Collaboration), Acta Phys. Polon. **B 43**, (2012) 555
42. M. Krzewicki (for the ALICE Collaboration), J. Phys. **G 38**, (2011) 124047

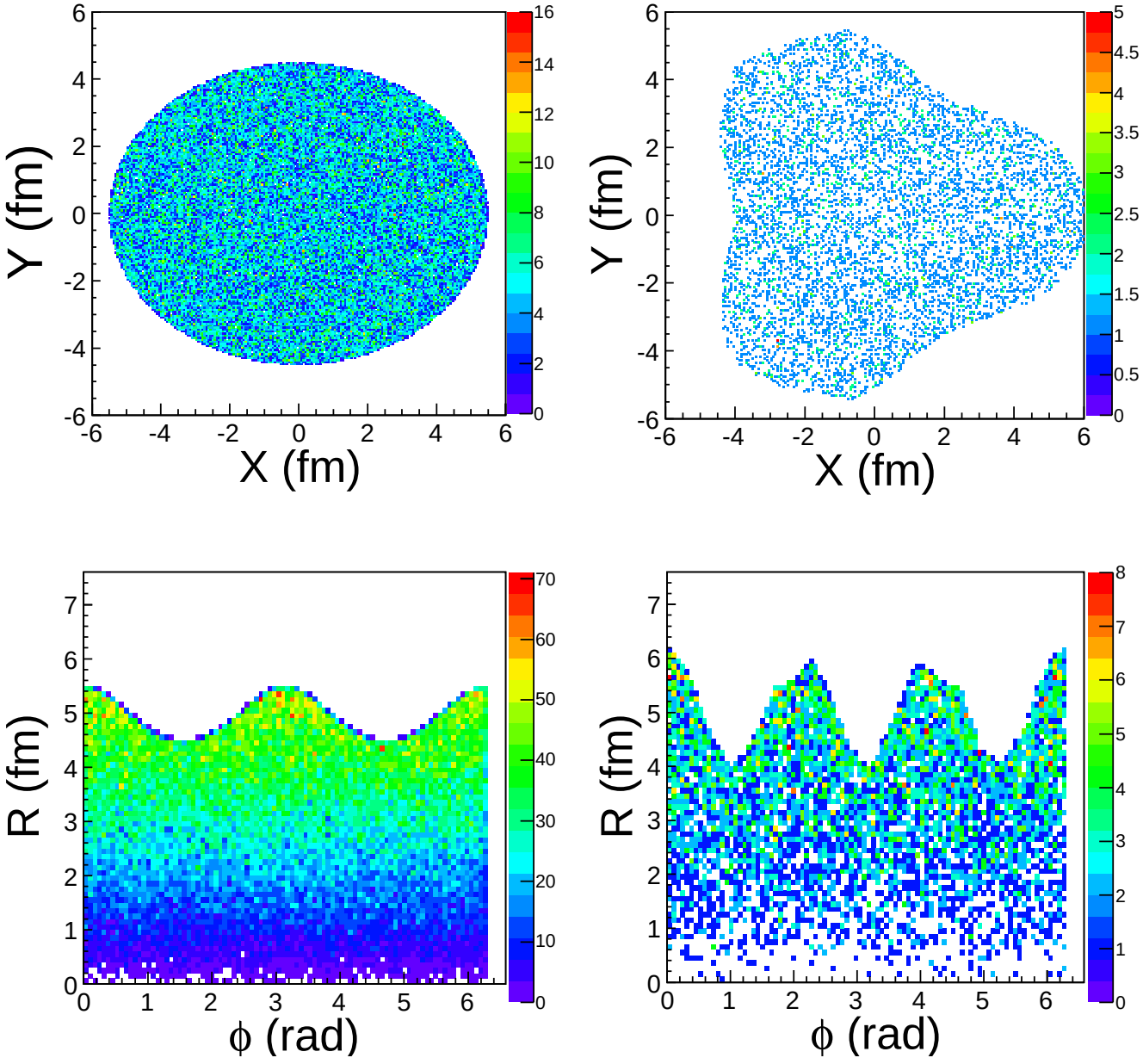

Fig. 1. The carton figure illustrating the second (left, $\epsilon_3(b) = 0$) and second+third (right, $\epsilon_3(b) = 0.2$) azimuthal anisotropy harmonics generation in HYDJET++ at $R_{\rm f}(b) = 5$ fm, $\epsilon(b) = -0.2$, $\Psi_2^{\rm RP} = 0$, $\Psi_3^{\rm RP} = 0$. Particle densities in the transverse plane are shown for X-Y (top) and R-ϕ (bottom) representations.

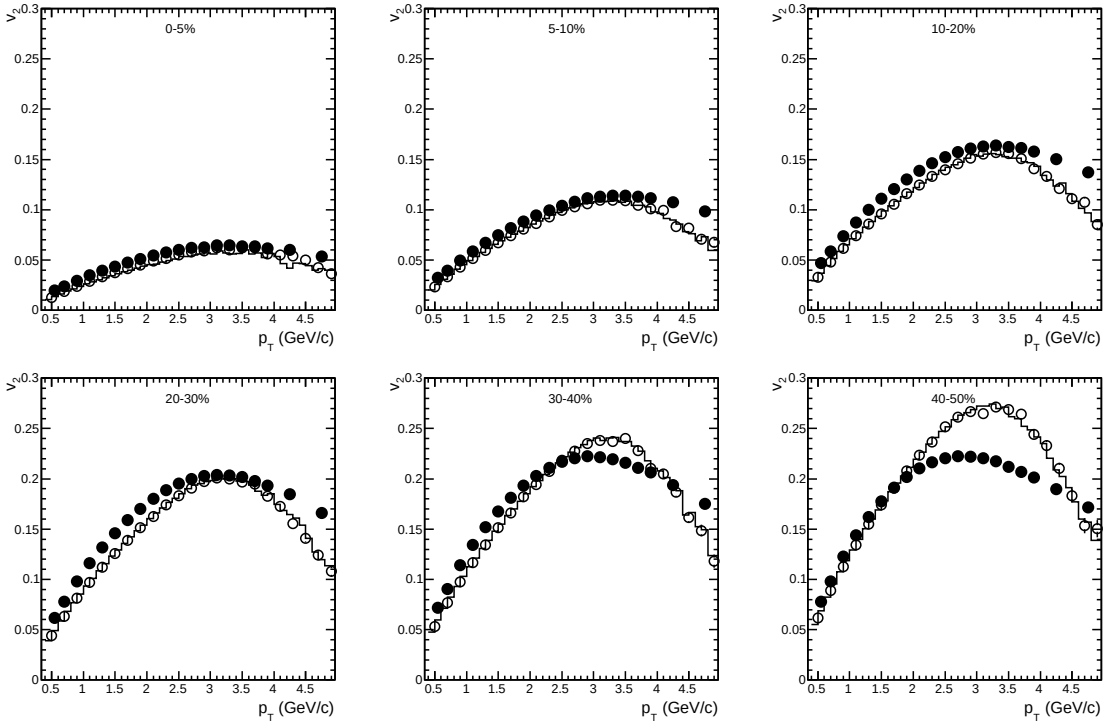

Fig. 2. Elliptic flow $v_2(p_{\rm T})$ of charged hadrons at pseudo-rapidity $|\eta| < 2.5$ for different centralities of PbPb collisions at $\sqrt{s}_{\rm NN} = 2.76$ TeV. The closed circles are ATLAS data [10] on $v_2\{\rm EP\}$, open circles and histograms represent $v_2\{\rm EP\}$ and $v_2(\Psi_2^{\rm RP})$ for HYDJET++ events, respectively.

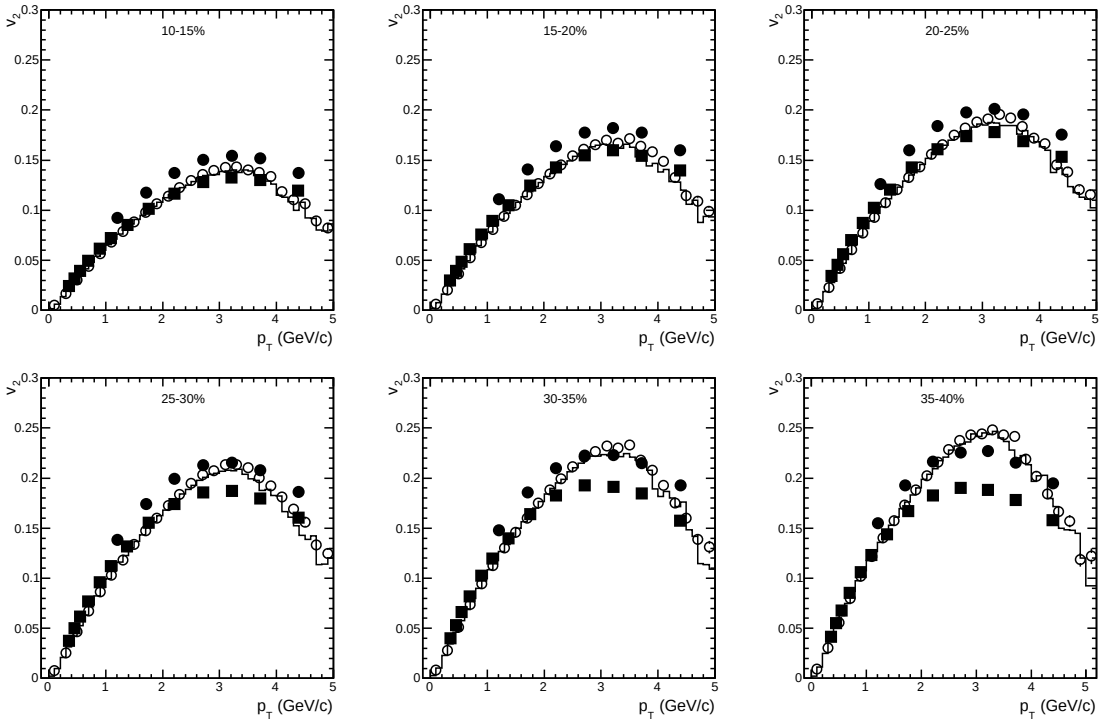

Fig. 3. Elliptic flow $v_2(p_{\rm T})$ of charged hadrons at pseudo-rapidity $|\eta| < 0.8$ for different centralities of PbPb collisions at $\sqrt{s}_{\rm NN} = 2.76$ TeV. The closed points are CMS data [8] ($v_2\{2\}$ — circles, $v_2\{\rm LYZ\}$ — squares), open circles and histograms represent $v_2\{\rm EP\}$ and $v_2(\Psi_2^{\rm RP})$ for HYDJET++ events, respectively.

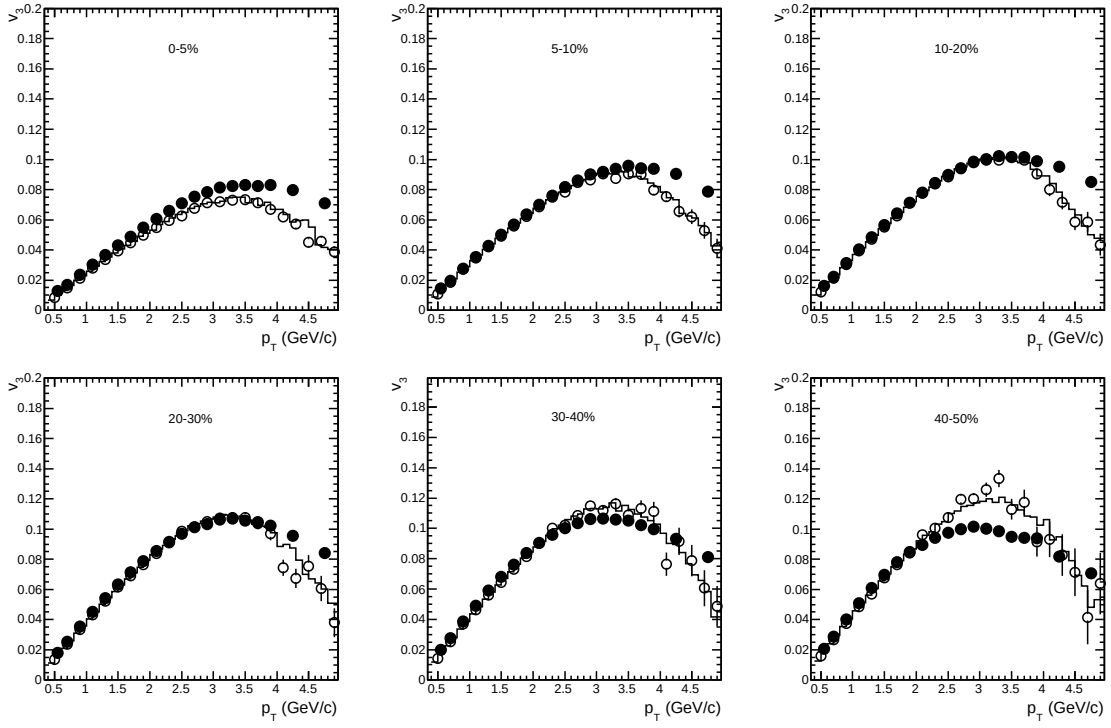

Fig. 4. Triangular flow $v_3(p_{\rm T})$ of charged hadrons at pseudo-rapidity $|\eta| < 2.5$ for different centralities of PbPb collisions at $\sqrt{s}_{\rm NN} = 2.76$ TeV. The closed circles are ATLAS data [10] on $v_3\{\rm EP\}$, open circles and histograms represent $v_3\{\rm EP\}$ and $v_3(\Psi_3^{\rm RP})$ for HYDJET++ events, respectively.

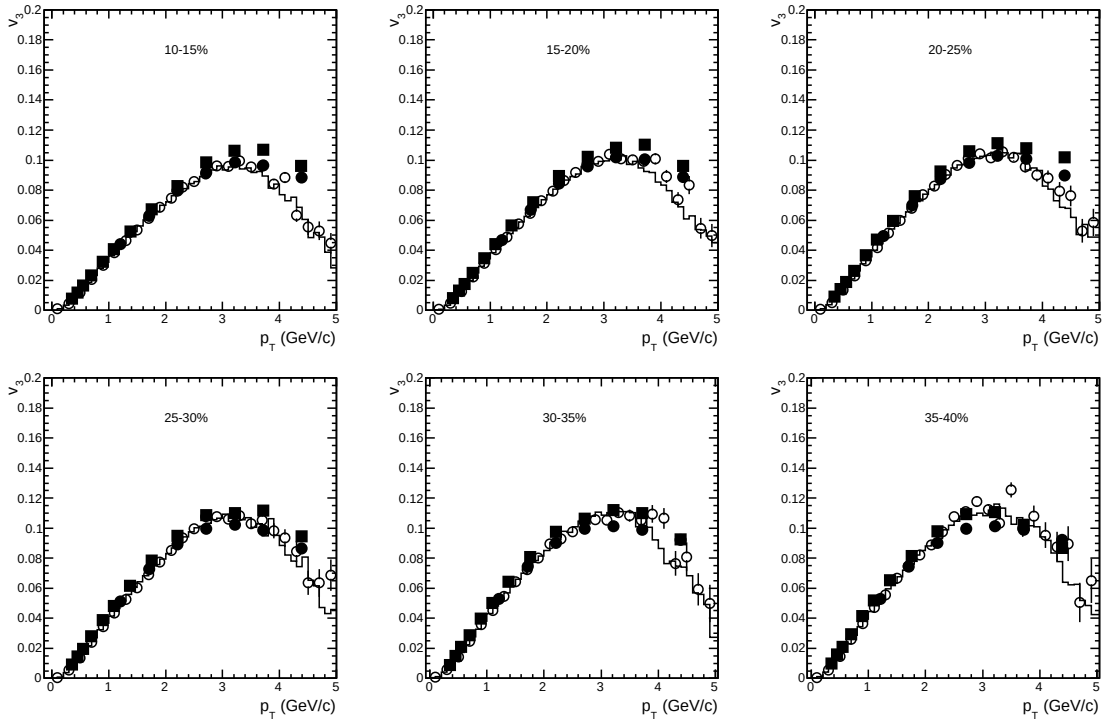

Fig. 5. Triangular flow $v_3(p_{\rm T})$ of charged hadrons at pseudo-rapidity $|\eta| < 0.8$ for different centralities of PbPb collisions at $\sqrt{s}_{\rm NN} = 2.76$ TeV. The closed points are CMS data [11] ($v_3\{2\}$ — circles, $v_3\{\rm EP\}$ — squares), open circles and histograms represent $v_3\{\rm EP\}$ and $v_3(\Psi_3^{\rm RP})$ for HYDJET++ events, respectively.

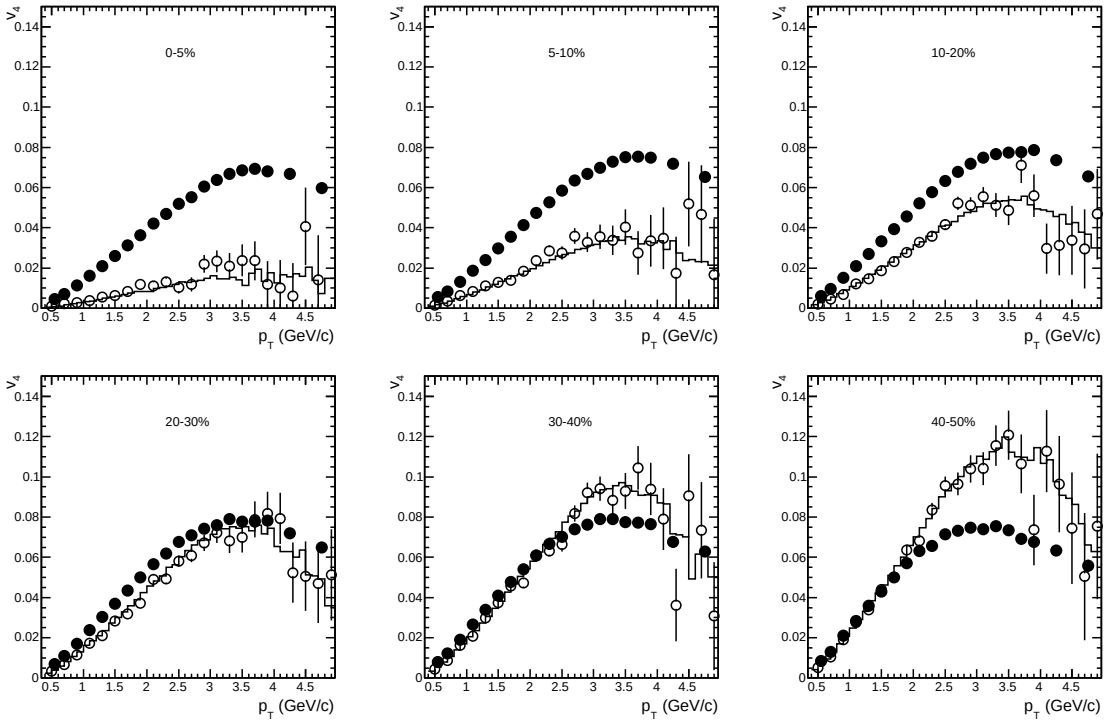

Fig. 6. Quadrangular flow $v_4(p_{\rm T})$ of charged hadrons at pseudo-rapidity $|\eta| < 2.5$ for different centralities of PbPb collisions at $\sqrt{s}_{\rm NN} = 2.76$ TeV. The closed circles are ATLAS data [10] on $v_4\{\rm EP\}$, open circles and histograms represent $v_4\{\rm EP\}$ and $v_4(\Psi_2^{\rm RP})$ for HYDJET++ events, respectively.

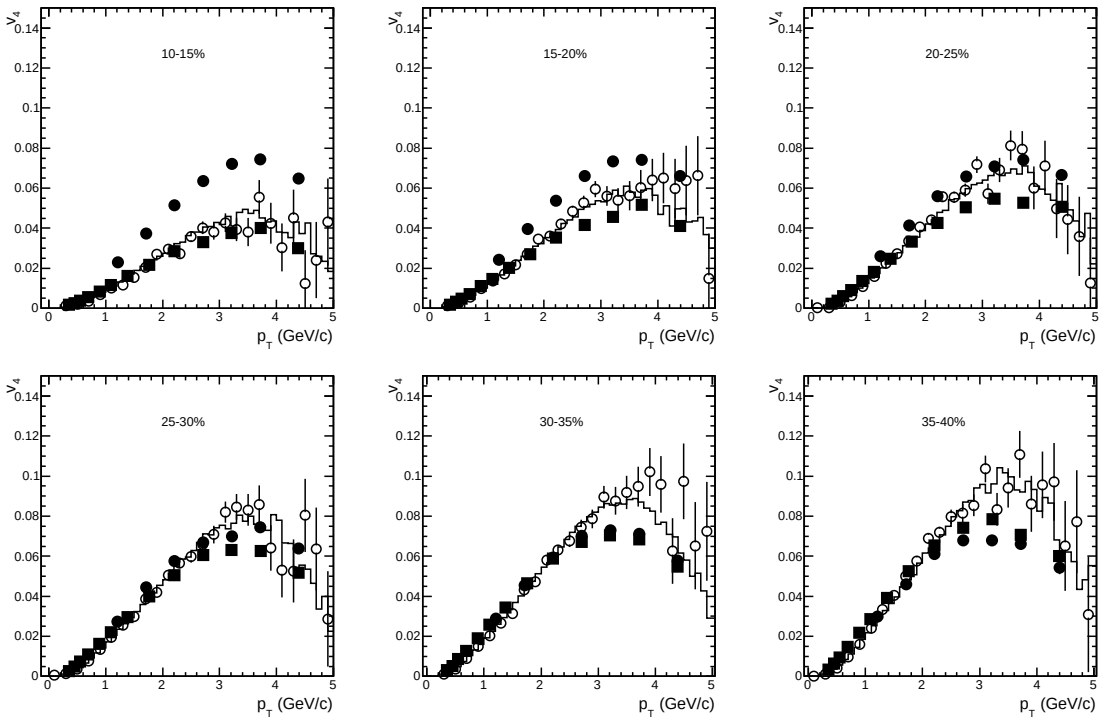

Fig. 7. Quadrangular flow $v_4(p_{\rm T})$ of charged hadrons at pseudo-rapidity $|\eta| < 0.8$ for different centralities of PbPb collisions at $\sqrt{s}_{\rm NN} = 2.76$ TeV. The closed points are CMS data [11] ($v_4\{2\}$ — circles, $v_4\{\rm LYZ\}$ — squares), open circles and histograms represent $v_4\{\rm EP\}$ and $v_4(\Psi_2^{\rm RP})$ for HYDJET++ events, respectively.

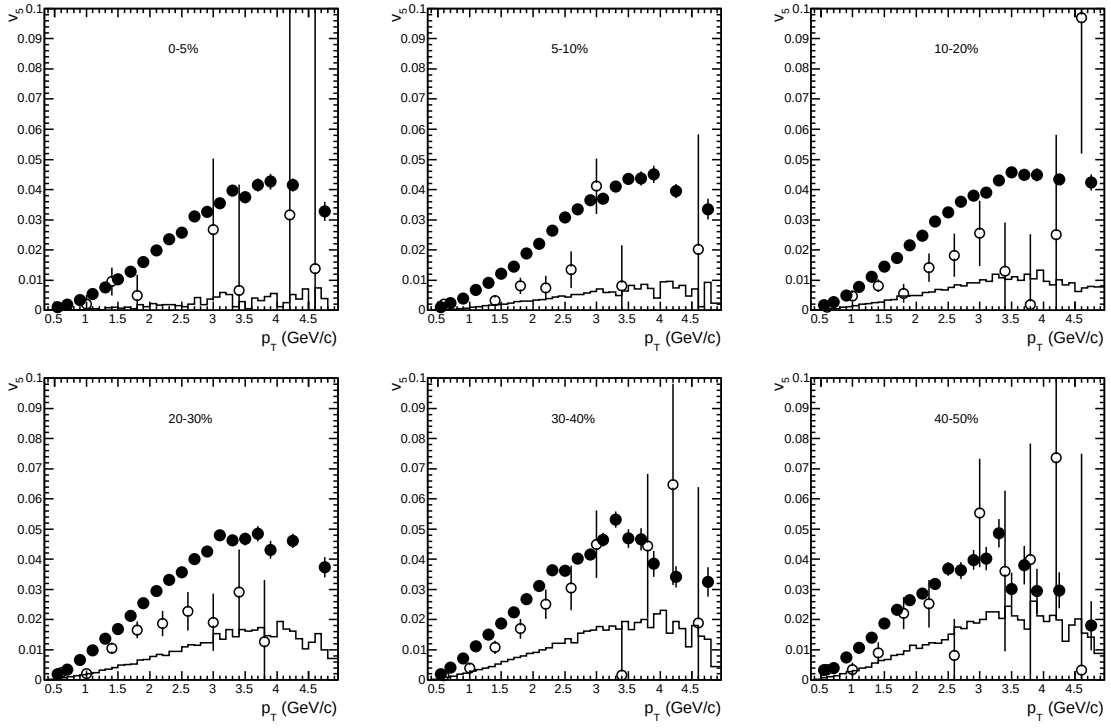

Fig. 8. Pentagonal flow $v_5(p_{\rm T})$ of charged hadrons at pseudo-rapidity $|\eta| < 2.5$ for different centralities of PbPb collisions at $\sqrt{s}_{\rm NN} = 2.76$ TeV. The closed circles are ATLAS data [10] on $v_5\{\rm EP\}$, open circles and histograms represent $v_5\{\rm EP\}$ and $v_5(\Psi_3^{\rm RP})$ for HYDJET++ events, respectively.

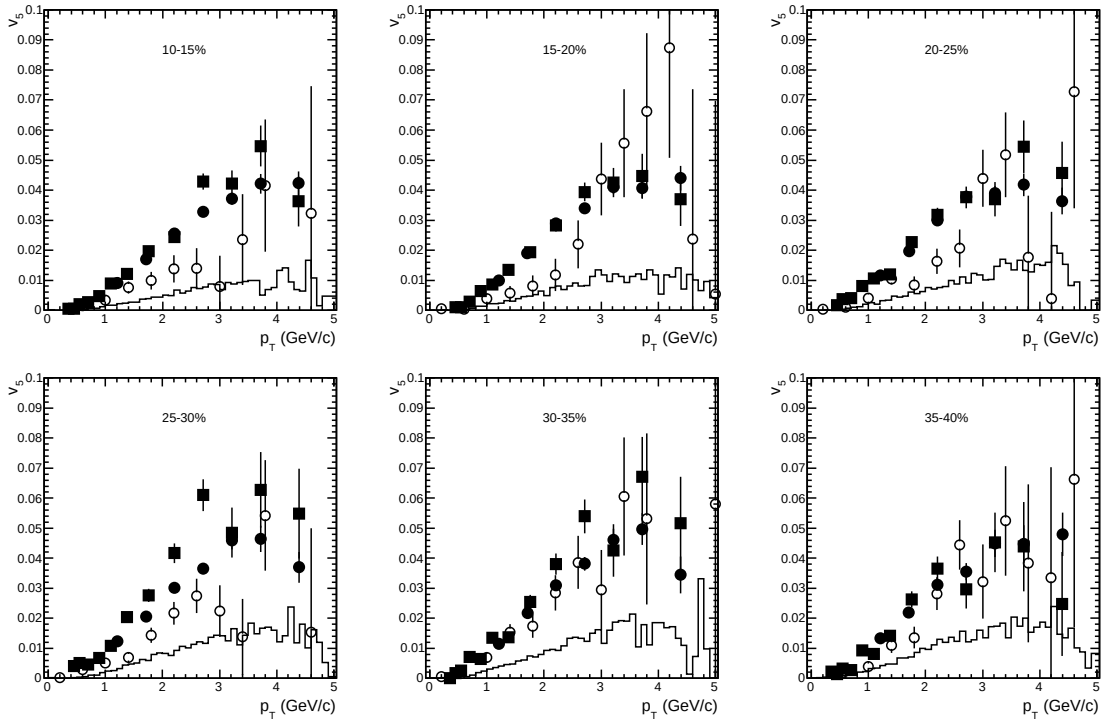

Fig. 9. Pentagonal flow $v_5(p_{\rm T})$ of charged hadrons at pseudo-rapidity $|\eta| < 0.8$ for different centralities of PbPb collisions at $\sqrt{s}_{\rm NN} = 2.76$ TeV. The closed points are CMS data [11] ($v_5\{2\}$ — circles, $v_5\{\rm EP\}$ — squares), open circles and histograms represent $v_5\{\rm EP\}$ and $v_5(\Psi_3^{\rm RP})$ for HYDJET++ events, respectively.

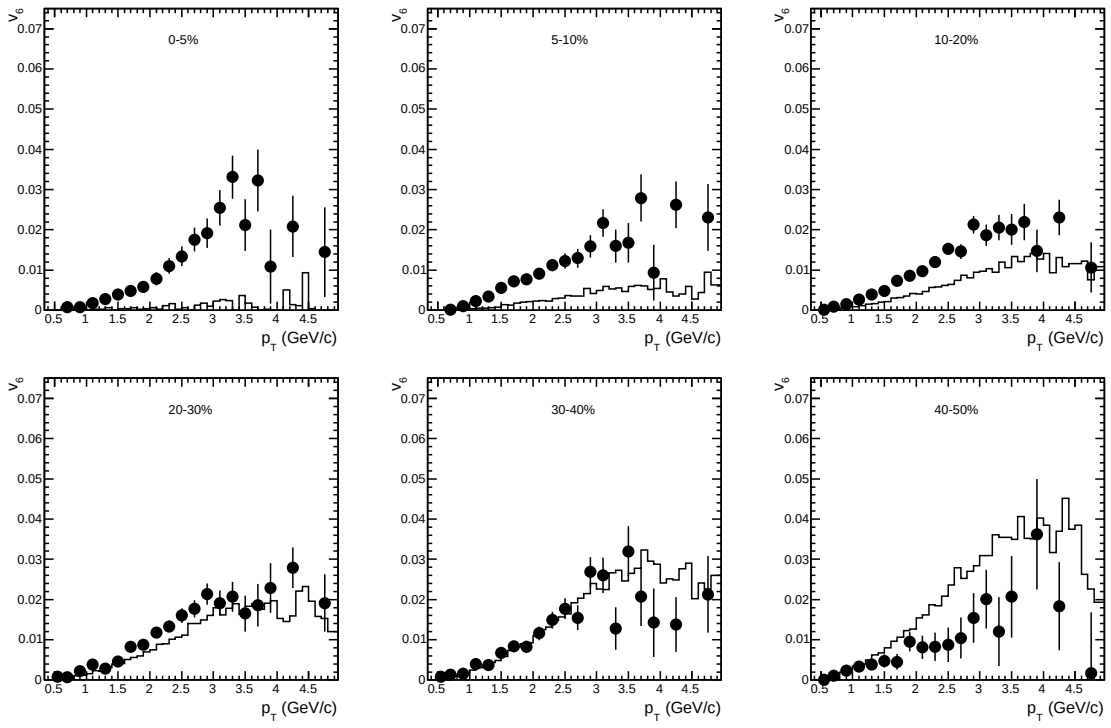

Fig. 10. Hexagonal flow $v_6(p_{\rm T})$ of charged hadrons at pseudo-rapidity $|\eta| < 2.5$ for different centralities of PbPb collisions at $\sqrt{s}_{\rm NN} = 2.76$ TeV. The closed circles are ATLAS data [10] on $v_6\{\rm EP\}$, histograms represent $v_6(\Psi_2^{\rm RP})$ for HYDJET++ events.

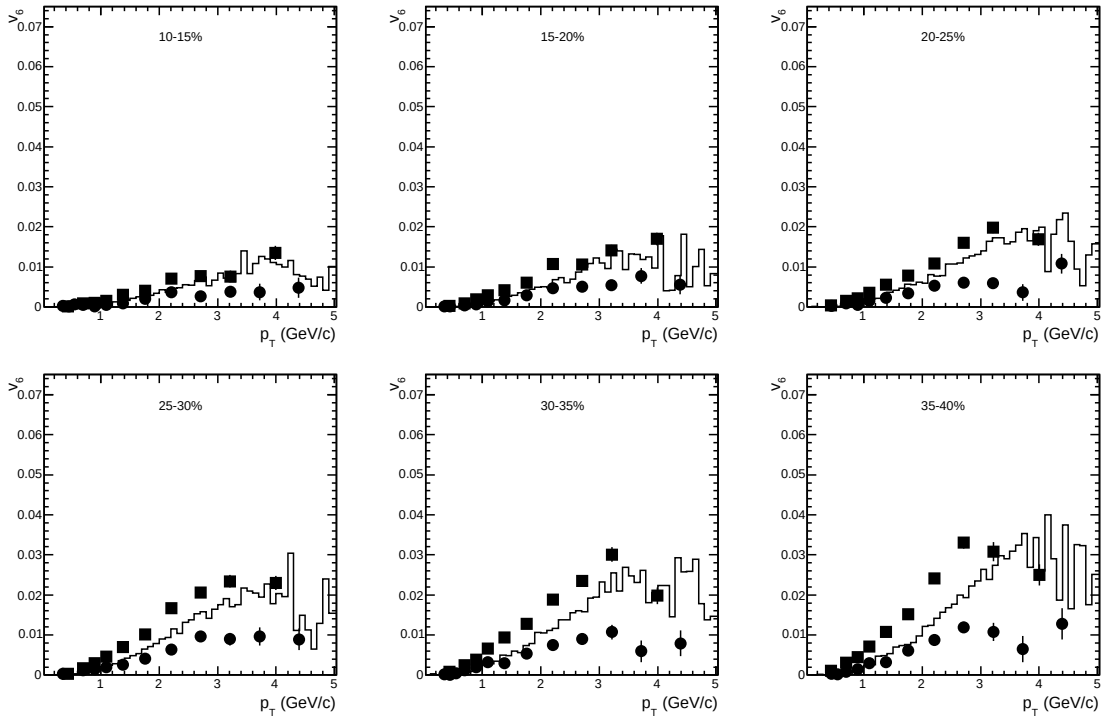

Fig. 11. Hexagonal flow $v_6(p_{\rm T})$ of charged hadrons at pseudo-rapidity $|\eta| < 0.8$ for different centralities of PbPb collisions at $\sqrt{s}_{\rm NN} = 2.76$ TeV. The closed points are CMS data [11] ($v_6\{\rm EP/\Psi_2\}$ — circles, $v_6\{\rm LYZ\}$ — squares), histograms represent $v_6(\Psi_2^{\rm RP})$ for HYDJET++ events.

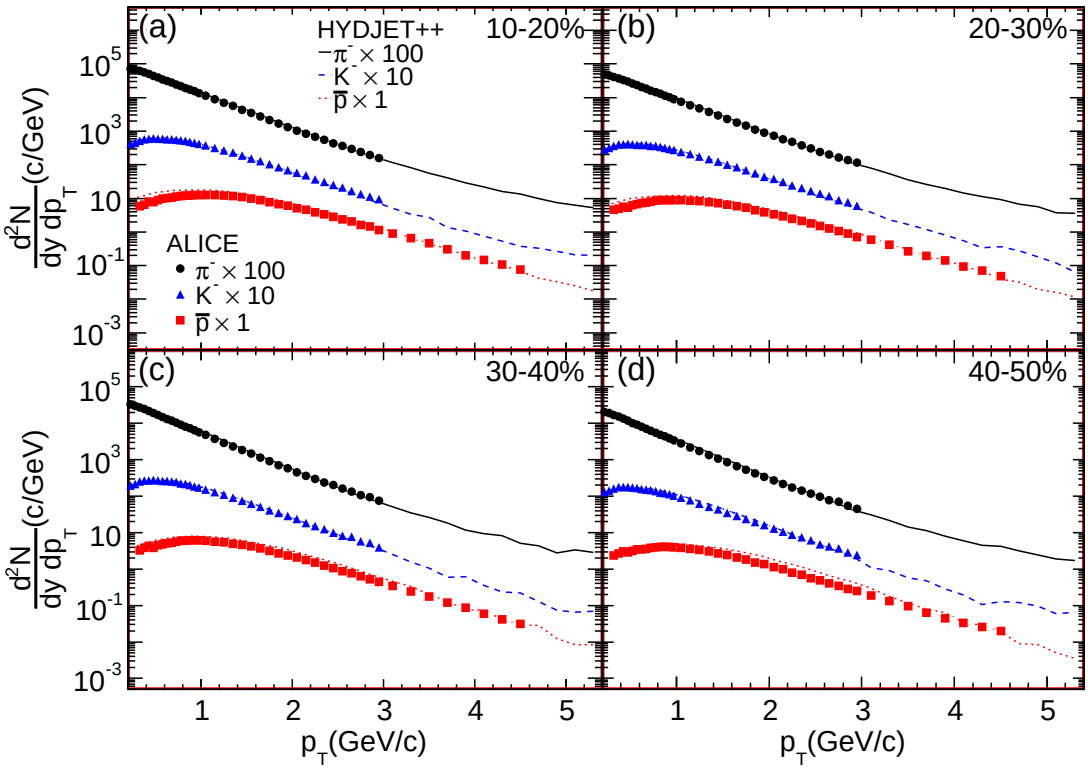

Fig. 12. Negatively charged pion, kaon and anti-proton transverse momentum spectra at pseudo-rapidity $|\eta| < 0.5$ for different centralities of PbPb collisions at $\sqrt{s_{\rm NN}} = 2.76$ TeV. The points are ALICE data [41], histograms are the simulated HYDJET++ events. The spectra are scaled by different factors for visual convenience.

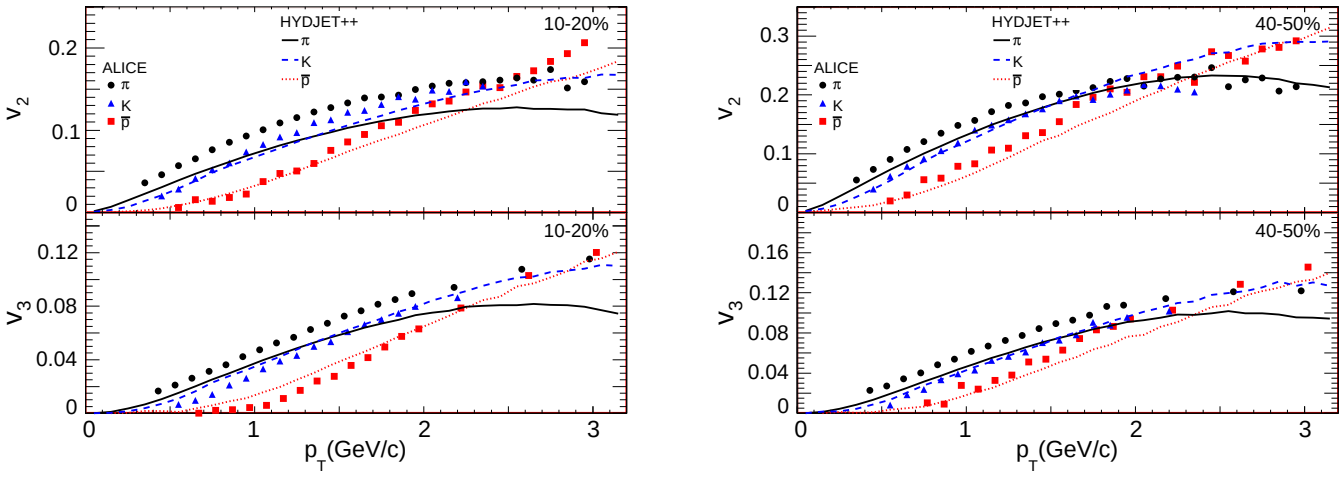

Fig. 13. Elliptic $v_2(p_{\rm T})$ and triangular $v_3(p_{\rm T})$ flows of charged pions, kaons and anti-protons at pseudo-rapidity $|\eta| < 0.8$ for 10–20% (left) and 40–50% (right) centrality of PbPb collisions at $\sqrt{s_{\rm NN}} = 2.76$ TeV. The points are ALICE data [42], histograms are the simulated HYDJET++ events.

.3 Hexagonal flow v_6 as a superposition of elliptic v_2 and triangular v_3 flows

Hexagonal flow v_6 as a superposition of elliptic v_2 and triangular v_3 flows

L. Bravina,[1] B.H. Brusheim Johansson,[1,*] G. Eyyubova,[2] V.L. Korotkikh,[2] I.P. Lokhtin,[2] L.V. Malinina,[2,†] S.V. Petrushanko,[2] A.M. Snigirev,[2] and E.E. Zabrodin[1,‡]

[1] *Department of Physics, University of Oslo, PB 1048 Blindern, N-0316 Oslo, Norway*

[2] *Skobeltsyn Institute of Nuclear Physics, Moscow State University, RU-119991 Moscow, Russia*

(Dated: February 26, 2015)

Partial contributions of elliptic v_2 and triangular v_3 flows to the hexagonal v_6 flow are studied within the HYDJET++ model for Pb+Pb collisions at $\sqrt{s} = 2.76A$ TeV. Scaling of the ratio $v_6^{1/6}\{\Psi_2\}/v_2^{1/2}\{\Psi_2\}$ in the elliptic flow plane, Ψ_2, is predicted in the range $1 \le p_t \le 4$ GeV/c for semicentral and semiperipheral collisions. Jets increase this ratio by about 10% and also cause its rise at $p_t \ge 3.5$ GeV/c. The part of v_6 coming from v_2 is instantly increasing as the reaction becomes more peripheral, whereas the contribution of v_3 to v_6 drops. This behavior explains the experimentally observed increase of correlations between second and sixth harmonics and the decrease of correlations between third and sixth harmonics with rising impact parameter b. Our study favors the idea that basic features of the hexagonal flow can be understood in terms of the interplay of elliptic and triangular flows.

PACS numbers: 25.75.-q, 25.75.Ld, 24.10.Nz, 25.75.Bh

I. INTRODUCTION

One of the main goals of heavy-ion experiments at ultrarelativistic energies is the study of properties of a new state of matter, quark-gluon plasma (QGP). Collider experiments with gold-gold collisions at $\sqrt{s} = 200\,\mathrm{GeV}$ at the Relativistic Heavy Ion Collider (RHIC) provided a lot of evidence that a hot and dense substance formed at the very beginning of the collision could be treated as a nearly perfect fluid [1]. Therefore, the whole paradigm has been changed. The plasma is no longer believed to be an ideal gas of noninteracting (or weakly interacting) partons, but rather a strongly interacting liquid [2]. It demonstrates a strong degree of collectivity, and the transverse flow of hadrons, particularly *elliptic* flow [3], is a very important signal that supports the hydrodynamic description of heavy-ion collisions. Hydrodynamic models, however, overestimate the flow at $p_t \ge 2\,\mathrm{GeV}/c$ [4], whereas conventional microscopic transport models usually undermine the strength of elliptic flow either at midrapidity [5] or at high transverse momenta [6, 7] at energies of RHIC or higher. The best description of the flow signal is obtained, therefore, in hybrid models, such as VISHNU [8] and MUSIC [9], which couple hydrodynamic treatment of the early stage of the expansion to hadron cascade model as an afterburner.

At present, the flow analysis is based on a Fourier decomposition of the azimuthal distribution of hadrons [10, 11],

$$E\frac{d^3N}{d^3p} = \frac{1}{\pi}\frac{d^2N}{dp_t^2 dy}\left[1 + 2\sum_{n=1}^{\infty} v_n \cos n(\phi - \Psi_n)\right], \quad (1)$$

where ϕ is the azimuthal angle between the transverse momentum of the particle and the participant event plane, each having its own azimuth Ψ_n, and p_t and y are the transverse momentum and the rapidity, respectively. The flow harmonic coefficients

$$v_n = \langle \cos n(\phi - \Psi_n) \rangle \quad (2)$$

are obtained by averaging over all events and all particles in each event. The first two harmonics, dubbed *directed*, v_1, and *elliptic*, v_2, flow have been studied rather intensively during the past 15 years [4], whereas the systematic study of higher harmonics, namely, *triangular*, v_3, *quadrangular* (or *hexadecapole*), v_4, *pentagonal*, v_5, and *hexagonal*, v_6, flow began quite recently in the Large Hadron Collider (LHC) era [12].

It is generally assumed that, in the case of noncentral collision of two similar nuclei, remnants of the interacting nuclei fly away quickly, thus giving space for expansion of the overlapped volume. In the transverse plane this area resembles an ellipse; therefore, odd harmonics of anisotropic flow, such as v_3, v_5, etc., can be neglected because of the symmetry considerations. The concept of participant triangularity due to initial-state fluctuations was first introduced in [13]. In model simulations, the triangular flow signal was found to be directly proportional to the participant triangularity. After that, correlations were studied between the higher-order harmonic eccentricity coefficients ε_n, linked to participant plane angles Φ_n, and the final anisotropic flow coefficients v_n and their final anisotropic flow angles Ψ_n; see, e.g., [14–18]. This analysis was done within both ideal and viscous relativistic hydrodynamics with Monte Carlo−Glauber

*Also at Oslo and Akershus University College of Applied Sciences (HIOA), Oslo, Norway

†Also at Joint Institute for Nuclear Researches, RU-141980 Dubna, Russia

‡Also at Skobeltsyn Institute of Nuclear Physics, Moscow State University, RU-119991 Moscow, Russia

or color glass condensate (CGC) initial conditions. One of the interesting observations is that just the first few flow harmonics survive after the hydrodynamic evolution despite the fact that the initial spacial anisotropies are of the same order [15]. The characteristic mode mixing between the different order flow coefficients has been revealed [16–18]. It is found that the final plane angles $\Psi_n,\ n > 3$ seem to be uncorrelated with the corresponding participant plane angles $\Phi_n,\ n > 3$, associated with initial anisotropies [19]. In contrast, the response of the elliptic flow to ellipticity, as well as that of the triangular flow to triangularity, is approximately linear [17]. Is it because of the crosstalk of several harmonics, and which harmonics play a major role in this process? To answer these questions it would be important to study the influence of v_2 and v_3, linked to elliptic and triangular anisotropies, respectively, on higher harmonics of the anisotropic flow. For our analysis the HYDJET++ model [20] is employed. The basic principles of the model are given in Sec. II.

II. MODEL

The Monte Carlo event generator HYDJET++ is a superposition of two event generators, FASTMC [21, 22] and PYQUEN [23], describing soft and hard parts of particle spectra in ultrarelativistic heavy-ion collisions at energies from RHIC ($\sqrt{s} = 200\,\mathrm{GeV}$) to LHC ($\sqrt{s} = 5.5\,\mathrm{TeV}$). Both FASTMC and PYQUEN generate particles independently. Their partial contributions to the total event multiplicity depend on collision energy and centrality. The soft part of a single event in HYDJET++ is a thermal hadronic state treated within the framework of parametrized hydrodynamics [21, 22]. The hard part of this event is represented by a multiple scattering of hard partons in a hot and dense medium, such as quark-gluon plasma. It accounts for the radiative and collisional energy losses [24] and shadowing effect [25]. Further details of the HYDJET++ model can be found elsewhere [20–23]. Below we concentrate on the simulation of anisotropic flow in the recent version of HYDJET++ [26].

In the case of noncentral collisions of identical nuclei the overlap area has a characteristic almond shape. This ellipsoid posseses the initial coordinate anisotropy, which is a function of impact parameter b and nuclear radius R_A, $\epsilon_0(b) = b/(2R_A)$. In the azimuthal plane the transverse radius of the fireball reads [22]

$$R_{\mathrm{ell}}(b,\phi) = R_{\mathrm{fo}}(b)\frac{\sqrt{1-\epsilon^2(b)}}{\sqrt{1+\epsilon(b)\cos 2\phi}}\ . \tag{3}$$

Here ϕ is the azimuthal angle and $R_{\mathrm{fo}}(0)$ is the model parameter that determines the scale of the fireball transverse size at freeze-out. The pressure gradients are stronger in the direction of the short axis in the transverse plane. Thus, the initial spatial anisotropy is transformed into the momentum anisotropy, which results in the anisotropy of the flow. The azimuthal angle of the fluid velocity vector ϕ_{fl} is linked to the azimuthal angle ϕ via [22]

$$\frac{\tan\phi_{\mathrm{fl}}}{\tan\phi} = \sqrt{\frac{1-\delta(b)}{1+\delta(b)}}\ , \tag{4}$$

with $\delta(b)$ being the flow anisotropy parameter. In the employed version of HYDJET++ both spatial and flow anisotropies, $\epsilon(b)$ and $\delta(b)$, are proportional to the initial spatial anisotropy $\epsilon_0 = b/(2R_A)$.

To introduce the triangular flow the transverse radius of the freeze-out surface is modified further [cf. Eq. (10) from [14]]:

$$R(b,\phi) = R_{ell}(b,\phi)\{1+\epsilon_3(b)\cos[3(\phi-\Psi_3)]\}\ , \tag{5}$$

where the new phase Ψ_3 is randomly distributed with respect to the position of the reaction plane Ψ_2. It means, in particular, that the integrated triangular flow measured in the Ψ_2 plane is zero, in accordance with the experimental observations. Similarly to $\epsilon(b)$, the new parameter $\epsilon_3(b)$, which is responsible for emergence of the triangular anisotropy, can be either linked to initial eccentricity $\epsilon_0(b)$ or treated as a free parameter.

It is worth mentioning here several important points. Like many other hydrodynamic models, HYDJET++ does not consider directed flow; i.e., v_1 of particles is essentially zero. The model describes the midrapidity area of heavy-ion collisions rather than the fragmentation ones. Recent measurements of the directed flow of charged particles done by the ALICE Collaboration at midrapidity in lead-lead collisions at $\sqrt{s} = 2.76\,\mathrm{TeV}$ [27] show that v_1 is order(s) of magnitude weaker than v_2 and v_3. Then, in contrast to event-by-event (EbE) hydrodynamics, HYDJET++ has no evolution stage and, therefore, cannot trace, e.g., propagation of energy and density fluctuations of the initial state, the so-called hot spots. It deals already with the final components of anisotropic flow. Lacking the EbE fluctuations, the model-generated ratios of different flow harmonics could be directly confronted only with the ratios obtained from EbE analysis of the data. This is not the case, however, because the data on flow harmonics are averaged over the whole statistics before performing the analysis of ratios, such as $v_n^{1/n}/v_2^{1/2}$. It leads to acquiring an extra multiplier to which the model results (or data) should be adjusted; see [28] for details.

The elliptic flow of particles contributes to all even harmonics, i.e., v_4, v_6, etc. For instance, quadrangular flow in HYDJET++ is determined by the elliptic flow of particles, governed by hydrodynamics, and particles coming from jets [29, 30]. The interplay between the elliptic and triangular flows will result in the appearance of odd higher harmonics in the model. Similarly to v_2, triangular flow should contribute separately to v_6, v_9, etc. The goal of our study of the hexagonal flow, v_6, is, therefore, twofold. First, the partial contributions of

v_2 and v_3, each having its own flow angle Ψ_2 and Ψ_3, to v_6 should be analyzed. Of particular interest are the features of the distributions $v_6\{\Psi_2\}(p_t)$ and $v_6\{\Psi_3\}(p_t)$. Second, the model allows one to investigate the influence of nonflow correlations, arising from jet fragmentation and resonance decays, on the flow harmonics. The previous study [29, 30] of the v_4/v_2^2 ratio revealed that the jet contribution to this ratio is quite substantial compared to the slight modification caused by the decays of resonances. But, before the analysis of generated spectra, we have to estimate individual contributions of elliptic and triangular flow to v_6 within the framework of relativistic ideal hydrodynamics.

III. v_6 AS A FUNCTION OF v_2 AND v_3

As was shown within the approach suggested in [31], the freeze-out distribution of fast particles obtained by a saddle-point integration is proportional to the exponential

$$\frac{d^3N}{dyd^2p_t} \propto \exp\left(\frac{p_t u_{\max} - m_t u^0_{\max}}{T}\right) , \qquad (6)$$

where $u = (u^0, u_\parallel, u_\perp)$ is the fluid 4-velocity, $u_\parallel \equiv u_{\max}$, $v_{\max} = u^0_{\max}/u_{\max}$, y is the rapidity, T is the temperature and $m_t = \sqrt{m^2 + p_t^2}$ is the transverse mass of a particle. The method utilizes the fact that fast particles come from regions of the freeze-out hypersurface where the $u_\parallel$, which is parallel to the particle's transverse momentum $\overrightarrow{p_t}$, is close to its maximum value $u_{\max}$ [31]. Assuming for the sake of simplicity a single event plane and expanding $u_{\max}(\phi)$ in Fourier series, one gets

$$u_{\max}(\phi) = u_{\max}\left[1 + 2\sum_{n=1}^{\infty} V_n \cos(n\phi)\right] . \qquad (7)$$

Denoting

$$a = \frac{p_t - m_t v_{\max}}{T}\, u_{\max} ,$$

we obtain from Eqs. (1), (6), and (7)

$$\exp\left\{a\left[1 + 2\sum_{n=1}^{\infty} V_n \cos(n\phi)\right]\right\} = 1 + 2\sum_{n=1}^{\infty} v_n \cos(n\phi) . \qquad (8)$$

Then, the expressions for the elliptic and triangular flows read

$$v_2 = aV_2 \equiv \frac{p_t - m_t v_{\max}}{T}\, u_{\max} V_2 , \qquad (9)$$

$$v_3 = aV_3 \equiv \frac{p_t - m_t v_{\max}}{T}\, u_{\max} V_3 , \qquad (10)$$

respectively. It is easy to see that the quadrangular flow depends on both V_2 and V_4:

$$v_4 = \frac{1}{2}a^2V_2^2 + aV_4 . \qquad (11)$$

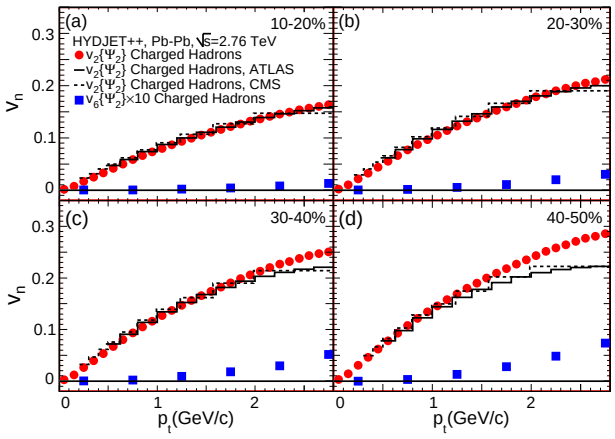

FIG. 1: (Color online) Transverse momentum dependencies of $v_2\{\Psi_2\}$ (circles) and $v_6\{\Psi_2\}$ (squares) of charged hadrons calculated within the HYDJET++ for Pb+Pb collisions at $\sqrt{s} = 2.76\,\text{TeV}$ at centralities (a) $\sigma/\sigma_{\text{geo}} = 10-20\%$, (b) $20-30\%$, (c) $30-40\%$, and (d) $40-50\%$. Solid and dashed histograms show experimental data on v_2 taken from ATLAS [32] and CMS [33], respectively.

Since the last term in Eq.(11) $aV_4 \ll a^2V_2^2 \equiv v_2^2$ at $p_t \to \infty$, we regain the familiar result $v_4 \cong \frac{1}{2}v_2^2$ [31]. For the hexagonal flow one gets, after the straightforward calculations,

$$v_6 = \frac{1}{6}(a^2V_2)^3 + \frac{1}{2}(aV_3)^2 + aV_6 + 3(aV_2)(aV_4) . \qquad (12)$$

Taking into account that at high transverse momenta $aV_4 \ll v_2^2$ and $aV_6 \ll a^2V_3^2 \equiv v_3^2$ we arrive at the simple expression

$$v_6 \cong \frac{1}{6}v_2^3 + \frac{1}{2}v_3^2 . \qquad (13)$$

Note again that this result was obtained under the assumption of a single event plane. We have learned in the past few years, however, that each of the flow harmonics v_n possesses its own event plane Ψ_n not necessarily coinciding with the others. The interplay between different event planes can be very important, and one should consider Eq. (13) as a first-order approximation. Model results for the hexagonal flow and its correlations with the elliptic and triangular flows are given below.

IV. RESULTS AND DISCUSSION

To study the formation of the hexagonal flow in the model ca. 2×10^6 lead-lead collisions were generated for each of four centralities $\sigma/\sigma_{\text{geo}} = 10-20\%$, $20-30\%$, $30-40\%$, and $40-50\%$. Transverse momentum distributions of v_6 in Ψ_2 and Ψ_3 planes are shown in Figs. 1 and 2, respectively, together with the corresponding distributions for the elliptic and triangular flows. Available experimental data for $v_2(p_t)$ and $v_3(p_t)$ are plotted onto the

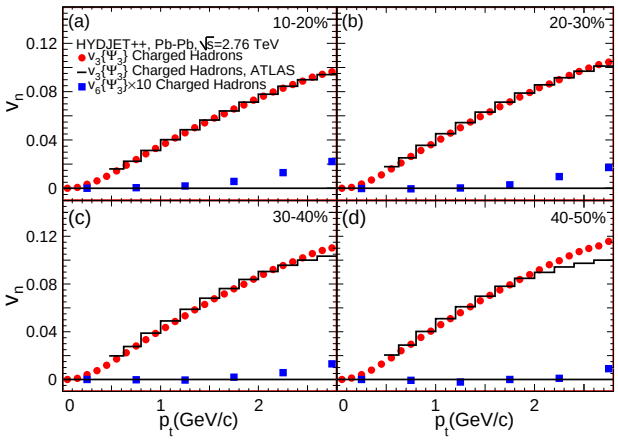

FIG. 2: (Color online) The same as Fig. 1 but for triangular and hexagonal flows in the Ψ_3 plane. Histograms show experimental data on v_3 taken from [32].

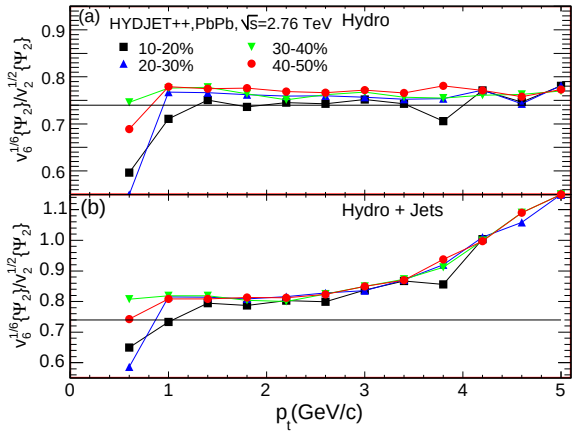

FIG. 3: (Color online) Ratio $v_6^{1/6}/v_2^{1/2}$ as a function of p_t in the Ψ_2 event plane for charged particles, originated from (a) soft processes only and (b) both soft and hard processes, in HYDJET++ simulations of Pb+Pb collisions at $\sqrt{s} = 2.76\,\mathrm{TeV}$. The reaction centralities are $10-20\%$ (squares), $20-30\%$ (triangles pointing up), $20-30\%$ (triangles pointing down), and $40-50\%$ (circles). Solid lines in both plots show the prediction of ideal hydrodynamics for this ratio at high p_t, namely, $v_6^{1/6}/v_2^{1/2} = (1/6)^{1/6} \approx 0.74$.

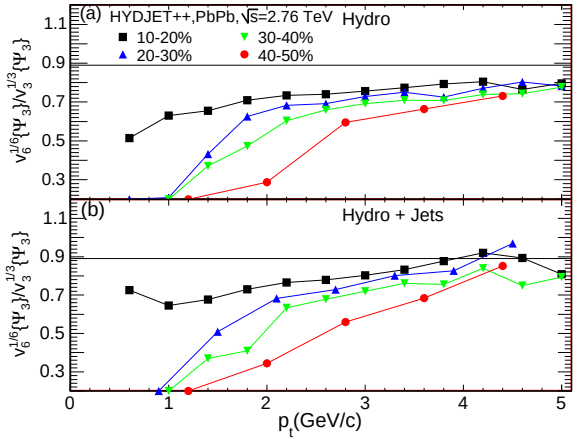

FIG. 4: (Color online) The same as Fig. 3 but for the ratio $v_6^{1/6}/v_3^{1/3}$ vs. p_t in the Ψ_3 event plane. Solid lines in both plots show the prediction of ideal hydrodynamics for this ratio at high p_t, namely, $v_6^{1/6}/v_3^{1/3} = (1/2)^{1/6} \approx 0.89$.

model calculations as well. The agreement with the data for both flow harmonics is fair. A detailed comparison of the model results with the data is given in [26]. Recall, that in contrast to many other hydrodynamic models the HYDJET++ model demonstrates a drop of elliptic flow at $p_t \geq 3\,\mathrm{GeV}/c$ [34, 35]. This drop is attributed in the model to the interplay of soft hydrodynamic processes and hard jets. In ideal hydrodynamics, particles with higher transverse momenta are carrying larger elliptic flow. However, the number of these particles decreases exponentially with rising p_t, and after certain p_t the particle spectrum is dominated by hadrons coming out from quenched jets. The elliptic flow of the jet hadrons is much lesser than the flow of hydro-induced hadrons; thus, the resulting flow of high-p_t particles drops (to almost zero modulo path-length dependence of in-medium partonic energy loss).

It appears that the hexagonal flow in HYDJET++ is weak but not zero in both Ψ_2 and Ψ_3 planes. In the Ψ_2 plane it starts to rise at $p_t \geq 1.5\,\mathrm{GeV}/c$ in semiperipheral collisions with $\sigma/\sigma_{\mathrm{geo}} \geq 30\%$. Here we observe a clear tendency that v_6 of charged hadrons with high transverse momenta increases with rising impact parameter. In the Ψ_3 plane the high-p_t tail of the distribution is presented as well. The generated $v_6\{\Psi_3\}(p_t)$ seems to become a bit weaker at $1 \leq p_t \leq 2.5\,\mathrm{GeV}/c$ with increasing b, despite the fact that triangular flow slightly increases. This peculiarity is clarified in our study below.

To check the scaling trends in the behavior of different flow harmonics the ratio $v_n^{1/n}/v_2^{1/2}$ is employed. The ratio $v_6^{1/6}(p_t)/v_2^{1/2}(p_t)$ in the Ψ_2 plane is displayed in Fig. 3 (a) for hadrons participated only in the hydrodynamic process and in Fig. 3(b) for all hadrons in the system. Note that the hexagonal flow here is determined with respect to Ψ_2 plane and not its own Ψ_6 plane. One can see the real scaling at $p_t \geq 1\,\mathrm{GeV}/c$, where all curves are on top of each other. For "hydrodynamic" particles the relation $v_6/v_2^3 \approx 1/6$ is fulfilled with good accuracy already at $p_t = 1\,\mathrm{GeV}/c$. The effect of jets is twofold. First of all, hadrons from jets increase the considered ratio by $\sim 10\%$ in the interval $1 \leq p_t \leq 3\,\mathrm{GeV}/c$, as demonstrated in Fig. 3(b). Second, at larger transverse momenta the ratio starts to rise further in contrast to the plateau in the hydrodynamic case.

The situation with the ratio $v_6^{1/6}(p_t)/v_3^{1/3}(p_t)$ in the Ψ_3 plane, which is depicted in Fig. 4, is not so clear. This ratio is below the ideal high-p_t limit $v_6/v_3^2 \approx 1/2$,

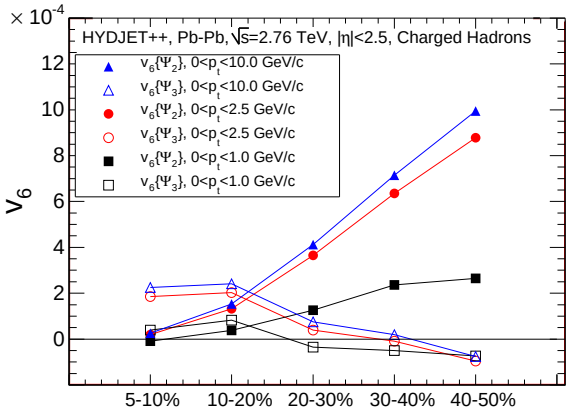

FIG. 5: (Color online) Hexagonal flow $v_6\{\Psi_2\}$ and $v_6\{\Psi_3\}$ of charged particles vs. centrality in Pb+Pb collisions at $\sqrt{s} = 2.76\,\text{TeV}$ simulated by HYDJET++. The pseudorapidity interval is $|\eta| < 2.5$. Solid and open symbols indicate $v_6\{\Psi_2\}$ and $v_6\{\Psi_3\}$ of hadrons with transverse momenta below $10\,\text{GeV}/c$ (triangles), $2.5\,\text{GeV}/c$ (circles), and $1\,\text{GeV}/c$ (squares), respectively.

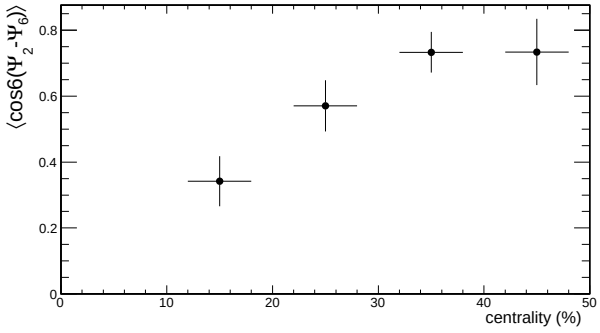

FIG. 6: Two-plane correlator $\cos\langle 6(\Psi_2 - \Psi_6)\rangle$ as a function of centrality for charged hadrons in HYDJET++ simulated Pb+Pb collisions at $\sqrt{s} = 2.76\,\text{TeV}$.

but steadily increases to it with rising transverse momentum. Jets also increase this ratio and make its rise a bit steeper. In contrast to the scaling in the Ψ_2 plane, the ratio $v_6^{1/6}/v_3^{1/3}$ in the Ψ_3 plane decreases for more peripheral collisions.

This means that the partial contributions of elliptic and triangular flows to the projections of the hexagonal flow onto Ψ_2 and Ψ_3 planes are changing with centrality. Figure 5 presents v_6, averaged in several p_t intervals, as a function of centrality in both Ψ_2 and Ψ_3 planes. Although the absolute magnitude of the signals depends on the selected p_t intervals, the tendencies in the v_6 development are clearly revealed. Namely, $v_6\{\Psi_2\}$ is weak in semicentral collisions but gradually increases for more peripheral reactions. This issue is supported by recent CMS data on hexagonal flow extracted by different methods [36]. And vice versa, $v_6\{\Psi_3\}$ is maximal in semicentral collisions and then drops. Summarizing information provided by Eq. (13) and Figs. 1, 2, and 5, we arrive at the following scenario. For central topologies triangular flow is stronger than the elliptic one; therefore, it makes the main contribution to the hexagonal flow. The event plane Ψ_6 is closer to the Ψ_3 rather than the Ψ_2 one. (Recall, that there are no genuine hexagonal deformations in the HYDJET++ model that can account for the formation of genuine v_6.) In peripheral topologies elliptic flow dominates over the triangular one. Thus, the resulting hexagonal flow event plane Ψ_6 should be oriented closer to Ψ_2. In other words, in semicentral collisions Ψ_6 is more strongly correlated with Ψ_3, whereas in more peripheral collisions Ψ_6 is correlated with Ψ_2.

To see this interplay more distinctly, we apply the method of event plane correlators [37–39]. For each flow harmonic of nth order one has to determine the event flow vector $\overrightarrow{Q_n}$ and the event plane angle Ψ_n following, e.g., prescription of [4, 11]

$$\begin{aligned}\overrightarrow{Q_n} &= (Q_{n,x}, Q_{n,y}) = \left(\sum_i w_i \cos(n\phi_i), \sum_i w_i \sin(n\phi_i)\right) \\ &= (Q_n \cos(n\Psi_n), Q_n \sin(n\Psi_n)) \ , \end{aligned} \tag{14}$$

$$\tan(n\Psi_n) = \frac{Q_{n,y}}{Q_{n,x}} \ , \tag{15}$$

where w_i and ϕ_i are the weight and the azimuthal angle of the ith particle in the laboratory system, respectively. The correlators between arbitrary l event planes of order k_l have the form $\langle\cos(\sum_{k=k_{l_{\min}}}^{k_{l_{\max}}} kc_k\Psi_k)\rangle$ with the constraint $\sum_{k=k_{l_{\min}}}^{k_{l_{\max}}} kc_k = 0$. In our case of just two planes, (Ψ_2, Ψ_6) and (Ψ_3, Ψ_6), the correlators are simply $\langle\cos 6(\Psi_2 - \Psi_6)\rangle$ and $\langle\cos 6(\Psi_3 - \Psi_6)\rangle$, respectively. Both correlators were extracted from the HYDJET++ events by the method applied for analysis of experimental data [38]. This approach implies separation of a single event into two forward-backward symmetric subevents with a pseudorapidity gap in between, and takes into account resolution corrections for each of the event planes; see [38] for details and also [39] for generalization of the method. Moreover, to avoid ambiguity in the interpretation of the results, we artificially increased the triangularity of the freeze-out hypersurface. The obtained correlators are displayed in Figs. 6 and 7. In contrast to Fig. 5, here the correlations are investigated between the different event planes and not between the flow harmonics projected onto Ψ_2 or Ψ_3 planes. We see that the correlator $\langle\cos 6(\Psi_2 - \Psi_6)\rangle$ increases for more peripheral collisions, whereas the correlator $\langle\cos 6(\Psi_3 - \Psi_6)\rangle$ drops. Similar centrality dependencies were observed by the ATLAS Collaboration as well [38]. Such a behavior has a simple explanation. The event plane Ψ_6 becomes closer to the Ψ_2 one as the hexagonal flow is strongly determined by the v_2 for the periph-

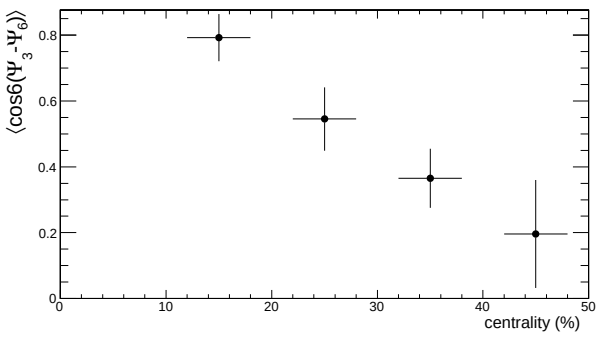

FIG. 7: The same as Fig. 6 but for two-plane correlator $\cos\langle 6(\Psi_3 - \Psi_6)\rangle$.

eral collisions. Because v_3 is randomly oriented with respect to v_2, the correlations between the Ψ_6 and the Ψ_3 become weaker. Recently, various two- and many-plane correlators were studied in [39] within the microscopic a multiphase transport AMPT model. Very good agreement with the experiment is demonstrated. However, the authors attribute the drop of the correlations between the third and the sixth harmonics to the decrease of the triangular flow itself. This is not the case, because the magnitude of the v_3 is approximately the same, as one can see, e.g., in Fig. 2. In our opinion, the falloff is driven by two reasons: (i) domination of v_2 over v_3 in semiperipheral and peripheral collisions, and (ii) absence of correlations between the Ψ_2 and Ψ_3.

Finally, the contribution of the genuine hexagonal fluctuations to the final hexagonal flow should be weak. The experimentally observed event plane correlations and other features of v_6 are reproduced in terms of interplay between the second and the third flow harmonics.

V. CONCLUSIONS

The hexagonal flow v_6 is studied within the HYDJET++ model in Pb+Pb collisions at $\sqrt{s} = 2.76\,\mathrm{TeV}$ and centralities $10\% \le \sigma/\sigma_{\mathrm{geo}} \le 50\%$. In contrast to the majority of hydrodynamic models, the HYDJET++ model combines parametrized hydrodynamics with jets. Only second and third flow harmonics are generated at the freeze-out hypersurface in the present version of the model; therefore, the hexagonal flow originates solely as a result of nonlinear hydrodynamic response, $v_6 \sim v_2^3 + v_3^2$. The following conclusions can be drawn.

(1) Scaling of the ratio $v_6^{1/6}\{\Psi_2\}/v_2^{1/2}\{\Psi_2\}$ is observed in the Ψ_2 event plane within the indicated centrality interval. No scaling is found for the ratio $v_6^{1/6}\{\Psi_3\}/v_3^{1/3}\{\Psi_3\}$.

(2) Jets increase both ratios by $10\% - 15\%$ and lead to rising high-p_t tails at $p_t \ge 3$ GeV/c.

(3) The behavior of the plane correlators $\langle\cos 6(\Psi_2 - \Psi_6)\rangle$ and $\langle\cos 6(\Psi_3 - \Psi_6)\rangle$ is in line with the experimental observations and with the centrality dependencies of v_6 on v_2 and v_3 in the Ψ_2 and Ψ_3 event planes, respectively. These findings strongly favor the idea that basic features of the hexagonal flow can be understood as a result of contributions of elliptic and triangular flows and their interplay. Original hexagonal initial fluctuations seem to play a minor role in the formation of v_6.

Acknowledgments. Fruitful discussions with L. Csernai and J.-Y. Ollitrault are gratefully acknowledged. This work was supported in parts by the Department of Physics, UiO, Russian Foundation for Basic Research under Grant No. 12-02-91505 and a Grant of the President of Russian Federation for Scientific School Supporting No. 3920.2012.2.

[1] I. Arsene *et al.* (BRAHMS Collaboration), Nucl. Phys. A **757**, 1 (2005); B.B. Back *et al.* (PHOBOS Collaboration), *ibid.* **757**, 28 (2005); J. Adams *et al.* (STAR Collaboration), *ibid.* **757**, 102 (2005); K. Adcox *et al.* (PHENIX Collaboration), *ibid.* **757**, 184 (2005).
[2] E. Shuryak, Prog. Part. Nucl. Phys. **53**, 273 (2004).
[3] J.-Y. Ollitrault, Phys. Rev. D **46**, 229 (1992); **48**, 1132 (1993).
[4] S. A. Voloshin, A. M. Poskanzer, and R. Snellings, in *Relativistic Heavy Ion Physics*, Landolt-Börnstein Database Vol. 23, edited by R. Stock (Springer, Berlin, 2010), p.5−54.
[5] M. Bleicher and H. Stöcker, Phys. Lett. B **526**, 309 (2002).
[6] E. E. Zabrodin, C. Fuchs, L. V. Bravina, and Amand Faessler, Phys. Lett. B **508**, 184 (2001).
[7] G. Burau, J. Bleibel, C. Fuchs, Amand Faessler, L. V. Bravina, and E. E. Zabrodin, Phys. Rev. C **71**, 054905 (2005).
[8] H. Song, S. A. Bass, and U. Heinz, Phys. Rev. C **83**, 024912 (2011).
[9] B. Schenke, S. Jeon, and C. Gale, Phys. Rev. C **82**, 014903 (2010).
[10] S. Voloshin and Y. Zhang, Z. Phys. C **70**, 665 (1996).
[11] A. M. Poskanzer and S. A. Voloshin, Phys. Rev. C **58**, 1671 (1998).
[12] J. Velkovska *et al.* (CMS Collaboration), J. Phys. G **38**, 124011 (2011); J. Jia *et al.* (ATLAS Collaboration), *ibid.*

38, 124012 (2011); R. Snellings *et al.* (ALICE Collaboration), *ibid.* **38**, 124013 (2011).
[13] B. Alver and G. Roland, Phys. Rev. C **81**, 054905 (2010).
[14] B. H. Alver, C. Gombeaud, M. Luzum, and J.-Y. Ollitrault, Phys. Rev. C **82**, 034913 (2010).
[15] G.-Y. Qin, H. Petersen, S. A. Bass, and B. Müller, Phys. Rev. C **82**, 064903 (2010).
[16] F. G. Gardim, F. Grassi, M. Luzum, and J.-Y. Ollitrault, Phys. Rev. C **85**, 024908 (2012).
[17] Z. Qiu and U. Heinz, Phys. Rev. C **84**, 024911 (2011).
[18] D. Teaney and L. Yan, Phys. Rev. C **86**, 044908 (2012).
[19] U. Heinz and R. Snellings, Annu. Rev. Nucl. Part. Sci. **64**, 123 (2013). (
[20] I. P. Lokhtin, L. V. Malinina, S. V. Petrushanko, A. M. Snigirev, I. Arsene, and K. Tywoniuk, Comput. Phys. Commun. **180**, 779 (2009).
[21] N. S. Amelin, R. Lednicky, T. A. Pocheptsov, I. P. Lokhtin, L. V. Malinina, A. M. Snigirev, Iu. A. Karpenko, and Yu. M. Sinyukov, Phys. Rev. C **74**, 064901 (2006).
[22] N. S. Amelin, R. Lednicky, I. P. Lokhtin, L. V. Malinina, A. M. Snigirev, Iu. A. Karpenko, Yu. M. Sinyukov, I. Arsene, and L. Bravina, Phys. Rev. C **77**, 014903 (2008).
[23] I. P. Lokhtin and A. M. Snigirev, Eur. Phys. J. **C46**, 211 (2006).
[24] http://cern.ch/lokhtin/pyquen.
[25] K. Tywoniuk, I. C. Arsene, L. Bravina, A. B. Kaidalov, and E. Zabrodin, Phys. Lett. B **657**, 170 (2007).
[26] L. V. Bravina, B. H. Brusheim Johansson, G. Kh. Eyyubova, V. L. Korotkikh, I. P. Lokhtin, L. V. Malinina, S. V. Petrushanko, A. M. Snigirev, and E. E. Zabrodin, arXiv:1311.7054.
[27] B. Abelev *et al.* (ALICE Collaboration), Phys. Rev. Lett. **111**, 232302 (2013).
[28] C. Gombeaud and J.-Y. Ollitrault, Phys. Rev. C **81**, 014901 (2010).
[29] L. Bravina, B. H. Brusheim Johansson, G. Eyyubova, and E. Zabrodin, Phys. Rev. C **87**, 034901 (2013).
[30] E. Zabrodin, G. Eyyubova, L. Malinina, and L. Bravina, Acta Phys. Pol. B Proc. Suppl. **5**, 349 (2012).
[31] N. Borghini and J.-Y. Ollitrault, Phys. Lett. B **642**, 227 (2006).
[32] G. Aad *et al.* (ATLAS Collaboration), Phys. Rev. C **86**, 014907 (2012).
[33] S. Chatrchyan *et al.* (CMS Collaboration), Phys. Rev. C **87**, 014902 (2013).
[34] G. Eyyubova, L. V. Bravina, E. E. Zabrodin, V. L. Korotkikh, I. P. Lokhtin, L. V. Malinina, S. V. Petrushanko, and A. M. Snigirev, Phys. Rev. C **80**, 064907 (2009).
[35] E. Zabrodin, G. Eyyubova, L. Bravina, I. P. Lokhtin, L. V. Malinina, S. V. Petrushanko, and A. M. Snigirev, J. Phys. G. **37**, 094060 (2010).
[36] S. Chatrchyan *et al.* (CMS Collaboration), arXiv:1310.8651.
[37] R. S. Bhalerao, M. Luzum, and J.-Y. Ollitrault, Phys. Rev. C **84**, 034910 (2011).
[38] J. Jia *et al.* (ATLAS Collaboration), Nucl. Phys. A **910-911**, 276 (2013).
[39] R. S. Bhalerao, J.-Y. Ollitrault, and S. Pal, Phys. Rev. C **88**, 024909 (2013).